Study of beauty quark production and next-to-leading order effects at HERA

Dissertation
zur Erlangung des Doktorgrades
des Department Physik
der Universität Hamburg

vorgelegt von
Adriana Elizabeth Nuncio Quiroz
aus Toluca, Mexiko.

Hamburg
2008

Abstract

In this thesis a study on the production and evolution of beauty quarks in ep collisions at HERA is presented. The emphasis is put on the corresponding Quantum Chromodynamics predictions including next-to-leading order corrections.

In the context of this work the FMNR⊗PYTHIA interface was developed, which calculates next-to-leading order Quantum Chromodynamics predictions at visible level for heavy-flavour processes in the photoproduction regime. This is achieved using the REDSTAT routines which transform the FMNR program into a Monte Carlo-like event generator. The parton-level events obtained are interfaced to PYTHIA using the Le Houches accord routines. All branching ratios and decay channels of the heavy quarks implemented in the PYTHIA framework are used, and therefore complex cuts on the final state can be applied. The FMNR⊗PYTHIA interface is applied in this thesis to obtain next-to-leading order predictions for the recently finished heavy flavour ZEUS analyses: the $ep \rightarrow b\bar{b}X \rightarrow D^*\mu X'$ and $ep \rightarrow b\bar{b}X \rightarrow \mu^+\mu^- X'$ channels. A comparison with the H1 $D^*\mu$ measurement is also performed.

Since the use of such double tagging techniques to identify events where heavy flavours are present proved to be very convenient when the final state is a pair of leptons, another part of this thesis work deals with the implementation of an electron finder, the ^{G}Elec finder. This finder is tested on the reconstruction of the $J/\psi \rightarrow e^+e^-$ signal. Finally, a heavy-flavour analysis has been started, namely the $ep \rightarrow b\bar{b}X \rightarrow e\mu X'$ dilepton channel, using an integrated luminosity of 114 pb^{-1} gated by the ZEUS detector in the years 1996-2000. Compared to previous analyses the study of beauty quark production in this channel extends the phase space of the measurement closer to the kinematic threshold, since electrons provide access to lower p_T values than muons do.

The technical part of this thesis consisted in the calibration, maintenance and data quality monitoring of the ZEUS calorimeter. From where the list of channels to be excluded from all physics analyses was generated based on the weekly electronics calibration and the daily checks.

Kurzfassung

In dieser Dissertation wird die Produktion und Entwicklung von Beauty Quarks in ep-Kollisionen bei HERA untersucht. Dabei liegt der Schwerpunkt bei den zugehörigen Vorhersagen der Quantenchromodynamik in nächstführender Ordnung.

Im Rahmen dieser Arbeit wurde die FMNR⊗PYTHIA -Schnittstelle entwickelt, welche Vorhersagen in nächstführender Ordnung der Quantenchromodynamik auf sichtbarem Niveau für Prozesse mit schweren Quarks in Photoproduktion berechnet. Hierzu werden die REDSTAT-Routinen verwendet, welche das Programm FMNR in einen Monte-Carlo-artigen Ereignisgenerator transformieren. Die Ereignisse auf Partonlevel werden mithilfe der Le Houches accord-Routinen mit PYTHIA verbunden. Alle Verzweigungsverhältnisse und Zerfallskanäle der schweren Quarks werden wie in PYTHIA implementiert verwendet, sodass komplexe Schnitte auf den Endzustand angewandt werden können. Die FMNR⊗PYTHIA -Schnittstelle wird in dieser Arbeit zur Bestimmung von Vorhersagen in nächstführender Ordnung für in letzter Zeit erstellte ZEUS-Analysen mit schweren Quarks verwendet: für die Kanäle $ep \rightarrow b\bar{b}X \rightarrow D^*\mu X'$ und $ep \rightarrow b\bar{b}X \rightarrow \mu^+\mu^- X'$. Ein Vergleich mit den H1-Messungen im $D^*\mu$-Kanal wurde ebenfalls durchgeführt.

Da sich die Verwendung von Doppelnachweismethoden zur Identifikation von schweren Quarks als besonders erfolgreich erwiesen hat, falls im Endzustand ein Paar von Leptonen vorliegt, beschäftigt sich ein weiterer Teil dieser Arbeit mit der Identifikation von Elektronen, dem ^{G}Elec Algorithmus. Dieser Algorithmus wird mit einem $J/\psi \rightarrow e^+e^-$ Datensample getestet. Schliesslich wird eine Analyse mit schweren Quarks im $ep \rightarrow b\bar{b}X \rightarrow e\mu X'$ Kanal unter Verwendung einer integrierten Luminosität von $114\,pb^{-1}$ aus ZEUS-Daten der Jahre 1996-2000 begonnen. Im Vergleich zu vorhergehenden Analysen wird der Phasenraum der Beautyproduktion in diesem Kanal in Richtung des kinematischen Limits erweitert, da Elektronen die Verwendung niedrigerer p_T als Myonen ermöglichen.

Der technische Teil dieser Promotion umfasst die Kalibration, Instandhaltung und Überwachung der Datenqualität des ZEUS Kalorimeters. Hierbei wurde basierend auf der wöchentlichen Kalibration der Ausleseelektronik und täglicher Kontrollen die Liste aller für Physikanalysen zu verwendenden Kalorimeterkanäle erzeugt.

Contents

Chapter 1

Introduction

One of the dreams of the human being has always been the understanding of the universe. This has produced numberless efforts to try to build up a description of the matter and the phenomena around us. Our current understanding of the structure of matter is modeled in the Standard Model of particle physics. This theory –although incomplete– gives a simple and satisfactory description of the known phenomena, where forces between 12 fundamental fermions (quarks and leptons) and their antiparticles are mediated by the exchange of gauge bosons and the still undiscovered Higgs boson. The electromagnetic and weak interactions are successfully described by the unified electroweak model, and the strong interaction is well described by quantum chromodynamics (QCD). Leptons (e.g. the electron) exist as free particles, while quarks have never been detected to be in isolation. Due to the strong force the quarks combine to form color neutral composite particles called hadrons, e.g. the proton. At high energies the coupling strength of the strong interaction becomes smaller and perturbative methods can be applied in the calculation of the matrix elements of the interactions between particles, provided that a "hard" scale has been chosen. Such a hard scale can be provided for example by the masses of the heavy quarks (charm, beauty and top). The process of heavy quark production is therefore fundamental for the study of the theory of quantum chromodynamics.

The HERA (Hadron Electron Ring Anlage) accelerator, where electrons and protons were collided head-on at a centre-of-mass energy of 318 GeV, was a unique machine and the perfect testing ground for the study of the proton substructure. Fifteen years of data taking came to an end on June 30$^{\text{th}}$ 2007, when the electrons and protons in the HERA accelerator made their final lap in the accelerator ring. The experiments using HERA have produced important results which confirm the nature of the strong force and provided evidence that the electromagnetic and the weak force can be unified into a single force –a first step towards the hope of the grand unification of all fundamental forces into a single entity–. The Collaborations

from the different experiments at HERA have been an example and a model for good international cooperation. HERA also laid the foundations for the next generation of particle physics experiments at CERN's Large Hadron Collider, as well as for the planned International Linear Collider.

At HERA the process of heavy quark production is best suited for the study of the strong interactions. Such a test of QCD is not only of principal interest by itself, it is also crucial for the search for physics beyond the Standard Model at future colliders. The interpretation of the data of the corresponding experiments will depend on the precise knowledge of the rate of QCD processes, which will be one of the main background contributions in almost all processes and particularly in the search for new physics.

At HERA several heavy flavour analyses have been performed and compared with theoretical predictions at next-to-leading order. Nevertheless, these calculations were not available for all kinds of analyses, especially those tagging several particles in the final state with complicated cuts on those particles. This thesis work was developed in order to study the production of heavy flavours at HERA and the corresponding theoretical predictions including next-to-leading order corrections. With that aim, a new tool was developed, the FMNR⊗PYTHIA interface, which calculates next-to-leading order QCD predictions at visible level for heavy flavour processes in the photoproduction regime. In order to produce such an interface, first the FMNR program needed to be transformed into a Monte Carlo-like event generator. This was achieved using the REDSTAT routines which are implemented as an extension to the FMNR program. The REDSTAT method is based on a simple idea (although the implementation in the code is far from trivial), the combination of correlated events with similar kinematics. The parton-level events obtained after this process were interfaced to PYTHIA using the Le Houches accord routines. Using the PYTHIA framework it is possible to use all branching ratios and decay channels of the heavy quarks implemented there, with the advantage that complex cuts on final state particles can be applied. Finally, next-to-leading order cross section predictions at visible level can be obtained.

This new tool is used in this thesis to obtain predictions for two recently finished heavy flavour ZEUS analyses: the $ep \to b\bar{b}X \to D^*\mu X'$ and $ep \to b\bar{b}X \to \mu^+\mu^- X'$ channels. A comparison with the H1 $D^*\mu$ measurement is also performed.

The use of such double tagging techniques to identify events where heavy flavours are present has proven to be very convenient. When the final state is a pair of leptons, a good lepton identification is imperative. Therefore, another part of this thesis work was devoted to the implementation of a new electron finder, the $^{\text{G}}$Elec finder, which is also a first step towards the development of a general electron identification algorithm for ZEUS.

The ^{G}Elec finder is tested in this work on the reconstruction of the $J/\psi \to e^+e^-$ signal. A heavy-flavour analysis using a double tagging technique has been started using ^{G}Elec, namely the $ep \to b\bar{b}X \to e\mu X'$ dilepton channel, which is presented at the end of this thesis.

The contents of the following Chapters of this thesis are as follows: In **Chapter 2** the description of the HERA accelerator and ZEUS, one of its universal detectors, will be given. **Chapter 3** deals with the technical task of this thesis, the calibration and data quality monitoring of one of the most important components of the ZEUS detector, the Uranium calorimeter. **Chapter 4** summarizes the theoretical framework of the HERA physics relevant for this work. **Chapter 5** shows a brief review of the different techniques and previous measurements of heavy flavour production at HERA. The **Chapter 6** presents the FMNR⊗PYTHIA interface, designed to provide heavy flavour NLO predictions at visible level. **Chapter 7** deals with the new ^{G}Elec finder and the dilepton identification of beauty quarks. **Chapter 8** summarizes the work done in this thesis and states the conclusions on the obtained results.

Chapter 2

Experimental framework

This chapter contains a brief description of the HERA collider and one of its universal detectors: ZEUS. The detector components will be mainly described in the configuration that they had when the data used for the analyses treated in this work was taken (HERA I). Nevertheless, the upgrade of the accelerator and the ZEUS experiment will also be shortly explained, as the analysis method developed in this thesis can as well be implemented for more recent data (HERA II).

2.1 The HERA electron-proton collider

The HERA accelerator [1] was the first and the only lepton-proton collider in the world while operating. Located at the DESY (Deutsches Elektronen SYnchrotron) Research Centre in Hamburg, it operated since autumn 1991 and was closed down on June 30th 2007, after 15 years of data taking. At the time of writing this words the four experiments of HERA are being dismantled and in many cases shipped back to the institutes in charge, while the accelerator remains in the tunnel. HERA is making way for one of DESY's next big projects. Its main pre-accelerator PETRA is being converted into a high-brilliance synchrotron radiation source for X-rays. An aerial view of DESY and its accelerators is shown in Figure 2.1.

The HERA tunnel is 6.3 km long and is located $15 - 30$ m under ground level. It consists of four circular sectors and four straight sectors where the experimental halls were located, as shown in Figure 2.2.

The HERA machine collided electrons or positrons, accelerated to an energy of $E_e = 27.5$ GeV, with protons. The energy of the proton beam was changed at the beginning of 1998 from $E_p = 820$ to 920 GeV. The resulting ep center-of-mass energy was 300 or 318 GeV, respectively. Leptons and protons were stored and accelerated in two independent storage rings on top of each other inside the HERA

Figure 2.1: Aerial view of the DESY Research Centre in Hamburg. The location of the HERA and PETRA accelerators is indicated by dashed lines.

tunnel. The magnetic system of the lepton ring consisted of conventional magnets with a maximum field of 0.165 T, while for the proton ring superconducting magnets with a maximum field of 4.65 T were used.

The beams of particles consisted of up to 220 bunches of electrons or protons with approximately 10^{10} particles, crossing each other every 96 ns. Some bunches were left empty and were used for calibration and for the measurement of cosmic-ray background. When either the lepton or the proton bunch was empty it was possible to study the beam-related background, which originated from the interaction of the lepton or the proton beam with the residual gas in the beam pipe.

The electrons and protons were brought into collision in two interaction points, one in the North Hall where the H1 experiment was located, the other in the South Hall where the ZEUS experiment was placed. In the East Hall the HERMES experiment studied the spin structure of the nucleon using collisions of polarised leptons on an internally polarised target. The West Hall was used until 2003 by the HERA B
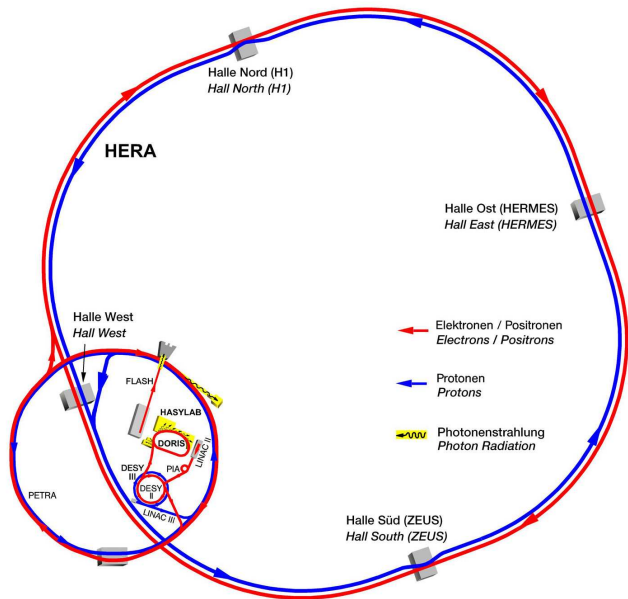
Figure 2.2: Schematic view of the HERA storage ring and its pre-accelerators system.

experiment, which studied collisions of the proton-beam halo with a wire target to measure CP-violation in decays of B mesons into the so-called "golden decay mode": $B \to J/\psi K^0$.

One of the main parameters of particle colliders is the *luminosity* $\mathcal{L}$. It is defined as the number of collisions per unit area and per unit time $[\,\mathrm{cm}^{-2}\,\mathrm{sec}^{-1}\,]$. The *specific luminosity* is the luminosity divided by the beam currents $[\,\mathrm{cm}^{-2}\,\mathrm{sec}^{-1}\,\mathrm{A}^{-2}\,]$. The specific luminosity quantifies the intrinsic quality of the colliding beams. The *integrated luminosity*, $\mathcal{L}_{\mathrm{int}}$, is the luminosity summed over a given period of time $[\,\mathrm{cm}^{-2}\,]$.

In particle physics the probability for a given process to occur is called *cross section*. The standard unit for measuring a cross section (denoted as σ) is the *barn*, which is equal to $10^{-24}\,\mathrm{cm}^2$, and thus $\mathcal{L}_{\mathrm{int}}$ can be expressed e.g. in pb^{-1}. The integrated luminosity is calculated using the number of occurrences (N events) of a process with cross section σ:

$$\mathcal{L}_{\mathrm{int}} = \frac{N}{\sigma}. \qquad (2.1)$$

High luminosity is obtained by optimising the transverse size of the beams, the number of particles per bunch, the lifetime of the beams and the number of bunches in the machine:

$$\mathcal{L}_{\mathrm{int}} = f\,\frac{n_1 n_2}{4\pi\sigma_x\sigma_y}, \qquad (2.2)$$

where n_1 particles collide on n_2 particles with frequency f and where σ_x and σ_y are the Gaussian transverse beam profiles in the x and y direction [2].

The performance of HERA in terms of the delivered luminosity from 1992 to 2007 is shown in Figure 2.3. The running period HERA I, began in 1992 with an electron beam, but in 1994 it was realized that the electron beam current was limited by positively ionised dust particles getting into the beam pipe through the pumps, reducing the lifetime of the beam. For this reason HERA switched to positrons in July 1994, achieving a more stable lepton beam and a significant increase in the integrated luminosity of the collected data. During the 1997-1998 shutdown, new pumps were installed in the

Figure 2.3: HERA delivered luminosities.

lepton beam pipe to improve the electron life time, and therefore during 1998 and parts of 1999 (and later also in 2005) HERA was running again with electrons.

Although a lot of interesting measurements were performed at the HERA I running period, the Collaborations expressed their desire for an upgrade of the HERA collider in order to obtain an increase in the luminosity that would favour especially the study of heavy flavour physics, high Q^2 events and exotic phenomena. The luminosity upgrade of the accelerator was therefore done during the 2000-2001 shutdown period. The HERA II running period initiated with the expectation of achieving a factor 5 higher specific luminosity. The detectors were also upgraded and the combination of new detector components together with the increasing luminosity brought a significant increase in the data sample which is leading to higher precision measurements. The HERA II running period ended in Summer 2007.

The upgrade project for HERA was centred mainly on two aspects. First, a stronger focusing of the beams at the interaction region, reducing the transverse region of the interacting beams, with the additional challenge of reducing at the

same time the synchrotron radiation background; and second, the installation of spin rotators to polarise the lepton beam longitudinally.

In the old focusing scheme the first proton quadrupole was placed at a distance of 26 m from the interaction point (IP). To achieve a stronger focusing, the magnets had to be moved closer to the experiments and therefore an earlier magnetic separation of the beams was required. New half-quadrupoles (GM) were installed at ±11 m from the IP. A thinner mirror plate which allows protons to be focused without large disturbance of the electron beam was placed only 7 cm away. Two superconducting magnets (GG and GO) were installed inside the experiments. These magnets perform the final focusing of the beams.

The reduction of the bending radius of the electron beam near the interaction point from 1200 m to 400 m, resulted in a significant increase of the synchrotron radiation, which could cause damage to the beam pipe and the closest components to it. An elliptical vacuum pipe was designed to stop the biggest part of the synchrotron radiation. These modifications are displayed in the Figure 2.4.
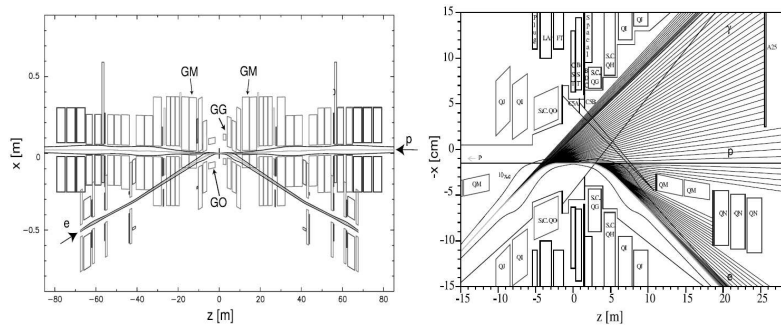
Figure 2.4: Layout of the modified interaction region at H1 and ZEUS (left). Emission of synchrotron radiation inside of the H1 detector (right), the case of the ZEUS detector is similar.

The lepton beam in HERA became naturally transversely polarised through the emission of synchrotron radiation [3]. Spin rotators on either side of the experiments changed the transverse polarisation of the beam into longitudinal polarisation. The positron beam polarisation was measured using two independent polarimeters, the transverse polarimeter (TPOL) and the longitudinal polarimeter (LPOL). Both devices exploited the spin-dependent cross section for Compton scattering of circularly polarised photons emitted from positrons to measure the beam polarisation.
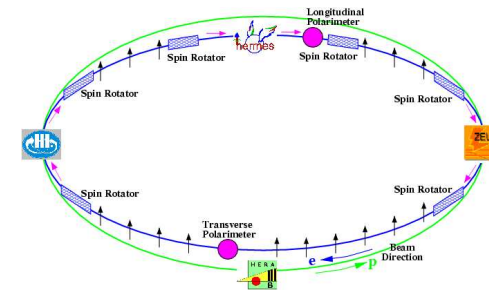
Figure 2.5: HERA polarimeters and spin rotators.

The transverse polarimeter was upgraded in 2001 to provide a fast measurement for every positron bunch, and position-sensitive silicon strip and scintillating-fibre detectors were added to investigate systematic effects. The spin rotators were already installed in HERMES at HERA I, and for the HERA II running period they were installed in the H1 and ZEUS experiments.

The HERA upgrade is described in detail in the reports [4, 5]. The main machine parameters before and after the upgrade are summarised in Table 2.1.

Type	HERA I design		typical in 2000		HERA II design	
Luminosity	$1.5 \times 10^{31}\,\mathrm{cm^{-2}\,s^{-1}}$		$1.7 \times 10^{31}\,\mathrm{cm^{-2}\,s^{-1}}$		$7.0 \times 10^{31}\,\mathrm{cm^{-2}\,s^{-1}}$	
$E_{\text{center-of-mass}}$	300 GeV		318 GeV		318 GeV	
	Lepton	Proton	Lepton	Proton	Lepton	Proton
Energy	30 GeV	820 GeV	27.5 GeV	920 GeV	27.5 GeV	920 GeV
Nr. bunches	210	210	180	180	180	180
Beam current	58 mA	160 mA	45 mA	100 mA	58 mA	140 mA
Particles p/bunch	3.6×10^{10}	10^{11}	3.5×10^{10}	7.3×10^{10}	4×10^{10}	10^{11}
Beam width	247 µm	247 mm	190 µm	190 µm	118 µm	118 µm
Beam height	78 µm	78 mm	50 µm	50 µm	32 µm	32 µm

Table 2.1: Main design parameters of HERA. Typical values in the year 2000 also shown.

2.2　　The ZEUS detector and its role at HERA

The experiments at HERA where particle beams collided –H1 and ZEUS– were general purpose magnetic detectors designed to study lepton-proton scattering. Both had nearly hermetic coverage. They differed principally by the choices made for calorimetry. The H1 Collaboration has stressed electron identification and spacial resolution by choosing a large diameter magnet encompassing the main liquid argon calorimeter; while the ZEUS Collaboration did put emphasis on energy resolution optimising the calorimetry for hadronic measurements, and chosen an uranium scintillator sampling calorimeter with equal response to electrons and hadrons. The experiments differed in construction and design, but they shared the aim to answer the same physical questions. With two independent experiments, measurements which can not be done in any other part of the globe, complement and verify each other. Detailed information on the detectors can be found in the technical proposals and status reports of the corresponding experiment [6, 7].

The ZEUS detector was situated in the HERA South Hall at about 30 m underground. The main part of the detector had a size of $12 \times 10 \times 19$ m and weighted about 3600 Tons (Figure 2.6). For most subdetectors the front-end electronics was mounted on the detector while the post-end electronics was located in the Rucksack (a three story building which could move with the detector), or in balconies or special areas around the detector.
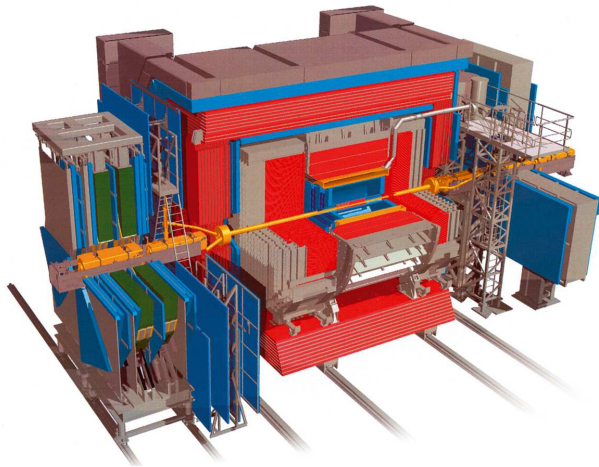
Figure 2.6: Three dimensional view of the ZEUS detector. One quadrant was removed to show the internal components.

The ZEUS coordinate system is a right-handed, orthogonal system with the origin at the nominal interaction point, the x axis points towards the center of HERA, the y axis points upward and the z axis points in the direction of the outgoing proton beam (also referred as to forward direction), as it is shown in Figure 2.7.
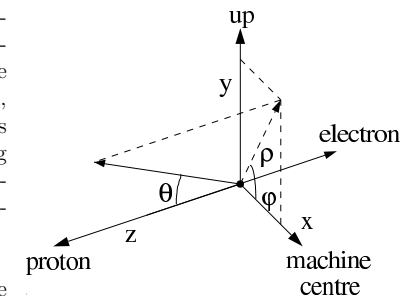
Figure 2.7: ZEUS coordinate system.

The ZEUS detector design reflects the different emphasis mentioned above as well as the large momentum imbalance between the lepton and the proton beams. This imbalance caused that most of the final state particles were boosted to the forward direction. Therefore the detector was designed asymmetrically, placing more components in the forward direction. The detector layout is shown in Figures 2.8 and 2.9.
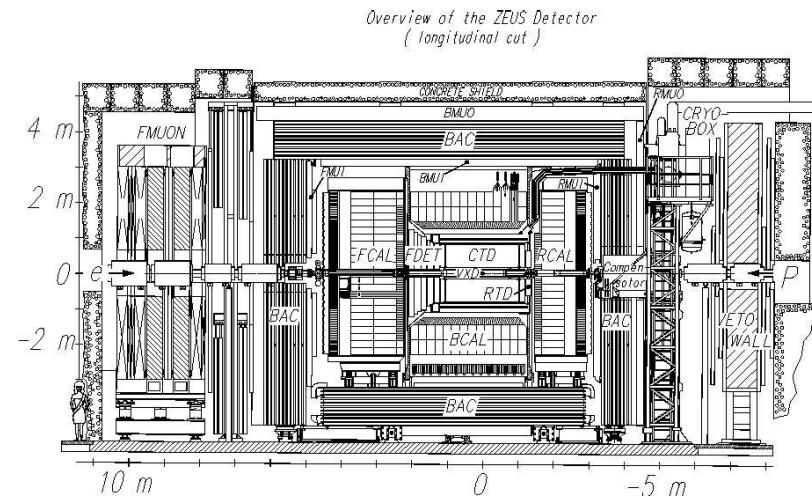
Figure 2.8: Cross section of the ZEUS detector along the beam axis in the HERA I configuration.

The interaction region was immediately surrounded by the tracking region. The innermost part of ZEUS used to be a vertex detector (VXD). This was removed during the shutdown in 1995-96, and replaced in the upgrade project of 2001 with a

silicon micro-vertex detector (MVD). The central tracking detector (CTD), a cylindrical drift chamber, was placed next. The CTD was complemented by forward (FTD) and backward (RTD) drift chambers and in the forward direction by a transition radiation detector (TRD) to identify high energy electrons. In the upgrade phase the straw tube tracking (STT) detector was installed to replace the TRD detector. The forward tracking (FDET) then consisted of three sets of planar drift chambers with transition radiation detectors between them, and in the rear region by one planar drift chamber consisting of three layers. Enclosing the tracking system, a super conducting solenoid provided a magnetic field of 1.43 T.

The compensating uranium calorimeter (CAL) surrounded the tracking system. In addition, pre-sampler detectors were mounted on the front of the calorimeter modules to correct the energy of the particles. The hadron-electron separator (HES) was installed, after three radiation lengths, inside the forward and rear parts of the calorimeter. To the calorimeter followed an iron Yoke which provided a return path for the magnetic field flux.

In order to measure particles that where not absorbed by the CAL, muon identification chambers were placed inside (FMUI, BMUI, RMUI) and outside (FMUON, BMUON, RMUON) the Yoke.

A small angle rear tracking detector (SRTD) was attached to the front face of the RCAL. The C5 counter, located also at the rear part or the calorimeter ($z = 314\,\text{cm}$), consisted of two planes of scintillators, one above and one below the beam pipe. The timing information given by these two sub-detectors was used to reject proton-beam gas events. Other detectors were located several meters away from the main detector along the beam pipe. The Leading Proton Spectrometer (LPS), consisting of six silicon strip detector stations was located at distances of $24 - 90\,\text{m}$ from the interaction point. It measured protons scattered at very small angles. To the rear side at $z = -7.5\,\text{m}$ the VETO wall, an iron-scintillator detector which consisted of an iron wall supporting scintillator hodoscopes, was used to reject background from proton-beam gas interactions too. The luminosity measurement was done by the LUMI detector, which consisted of two small lead scintillator calorimeters at $z = -106\,\text{m}$ for photons, and at $z = -35\,\text{m}$ for the electrons produced from bremsstrahlung events.

With this set up, particle identification was achieved for a variety of different physics processes at HERA: in Neutral Current (NC) events the scattered lepton (electron or positron) has to be identified and measured with high precision; the identification of electrons, positrons and muons is very important to study the semileptonic decay of heavy quarks and exotic process involving leptons. In Charged Current (CC) processes a hermetic detector is needed in order to reconstruct the missing transverse momentum carried by the outgoing neutrino.
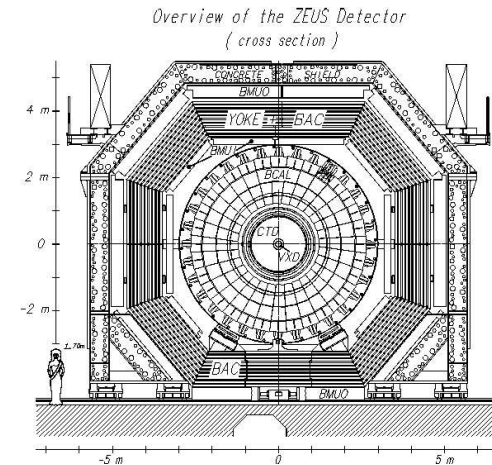
Figure 2.9: Cross section of the ZEUS detector orthogonal to the beam axis in the HERA I configuration.

A detailed description of the ZEUS detector can be found elsewhere [7]. A brief outline of the components that are most relevant for this analysis is given below.

2.3 The Central Tracking Detector

Charged particles were tracked in the Central Tracking Detector (CTD) [8]. This is a cylindrical drift chamber used to measure the direction and momentum of the charged particles. In addition, it was used to estimate the energy loss by ionisation dE/dx, which is used to discriminate between different types of particles.

The inner radius of the of the CTD chamber is 18.2 cm, the outer is 79.4 cm, and its active region covered the longitudinal interval from $z = -100\,\text{cm}$ to $z = 104\,\text{cm}$, resulting in a polar angle coverage of $15° < \theta < 164°$. One octant of the CTD is shown in the Figure 2.10.

The CTD is composed of 72 radial layers of sense wires, organised in 9 superlayers (SL). A group of eight radial sense wires in a superlayer, with the associated field wires, makes up a *cell*. Five of the superlayers (odd numbered), called *axial layers*, have wires parallel to the beam axis, whereas four (even numbered), called *stereo layers*, have wires with small stereo angles of about $\pm 5°$ to achieve better resolution in z. The electric field within the cells and the magnetic field from the solenoid
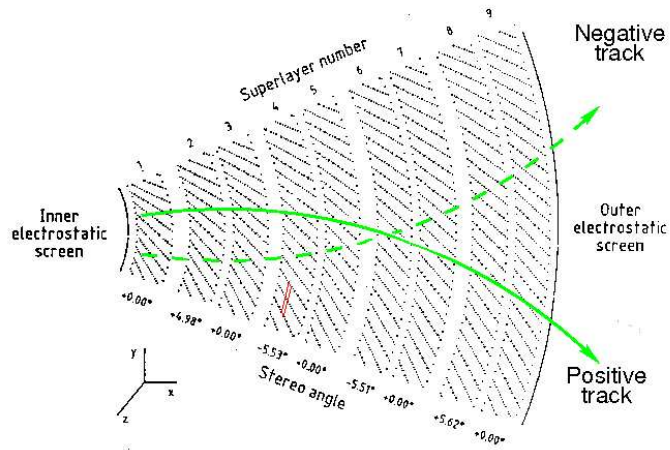
Figure 2.10: One octant of the CTD in the radial direction. The sense wires are indicated by dots. Examples of trajectories for positive and negative charged tracks are also displayed.

produce a Lorentz angle of 45°. The field wires were also tilted by 45° with respect to the radial direction of the CTD, for an approximate azimuthal drift of the electrons towards the sense wires.

The superlayers are numbered from inside to outside the detector, number 1 is the innermost and the outermost is superlayer 9. For trigger purposes, SL1, SL3, and SL5 are instrumented with a system that determines the z position using information on the arrival time of the particle (z-by-timing system). The achieved resolution is $\sim 200\,\mu$m in the $r - \phi$ plane and ~ 2 mm in the z coordinate. The momentum resolution is parametrised by [9]:

$$\frac{\sigma(p_T)}{p_T} = 0.0067 \cdot p_T \oplus 0.0071 \oplus \frac{0.0011}{p_T} \qquad (2.3)$$

for tracks fitted to the interaction vertex and passing at least 3 superlayers, with $p_T > 150$ MeV. The symbol $\oplus$ indicates the quadratic sum. The first term is the hit position resolution, while the second and third depend on the multiple scattering inside and before the volume of the chamber, respectively.

The CTD was filled with a mixture of Argon (Ar), Carbon Dioxide (CO_2) and Ethane (C_2H_6) in a proportion 86:3:11 up to the year 2000. In that year, a trace
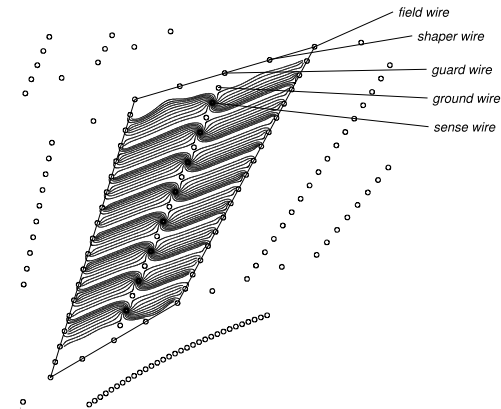
Figure 2.11: Layout of CTD drift cell.

of water ($\sim 0.15\%$) was added to the gas mixture to reduce deposits on the wires. These thin insulating deposits on the cathode wires lead to the accumulation of a positively charged ion layer which causes strong reduction of gain factors (Malter effect). As a result, electrons from the wire surface are emitted and cause avalanches at the anodes. This in turn leads to large standing currents in the chamber, and the CTD can not be reliably operated anymore. Later in 2000 the high voltage was decreased by 10% and the gas mixture was modified to return the pulse hight spectrum to that of the previous period.

A charged particle crossing the CTD produced ionisation of the gas mixture contained in the chamber. The electrons resulting from the ionisation drifted towards the sense wires (positive), whereas the positively-charged ions drifted towards the negative field wires. The drift velocity of the electrons is $\sim 50\,\mu$m/ ns. Near the sense wires, where the field was very strong, an avalanche effect occurred, giving an amplification factor on the electrons of $\sim 10^4$, so that a readable pulse was induced in the sense wires. The pulse measured was proportional to the energy loss of the initial particle, and with this information the average energy loss per unit of length (dE/dx) was measured.

The dE/dx measurement is a fundamental ingredient of particle identification, and recently large efforts were done in order to improve the precision of the measurements. Several corrections were applied to the dE/dx measurement of the ZEUS CTD, yielding a much better particle discrimination, e.g. corrections on the wire gain, drift-time effect, run-by-run differences, etc. A very extensive review of all the corrections can be found in [10].

2.4 The uranium-scintillator Calorimeter

The ZEUS calorimeter (CAL) [11] was one of the most important components for the experiment, providing energy measurements, electron/hadron discrimination, timing, and participating in the trigger at all levels. It was a high resolution compensating calorimeter with photomultiplier readout. It enclosed the tracking system and the solenoid, and had almost hermetic coverage with 99.7% of the 4π solid angle. It consisted of 3.3 mm depleted Uranium plates (98.1% U^{238}, 1.7% Nb, 0.2% U^{235}) wrapped into stainless steel foils (200 or 400 µm thick) as absorber material, alternated with 2.6 mm thick organic scintillators (SCSN-38 polystyrene) as active material. The high Z of the Uranium implied a compact size of the calorimeter and its natural radioactivity provided the means for calibration (as will be explained in Chapter 3).

The light generated by charged particles which traversed the scintillator was collected by plastic wavelength shifters and transported to photomultipliers where the light was transformed into electrical signals (Figure 2.12).
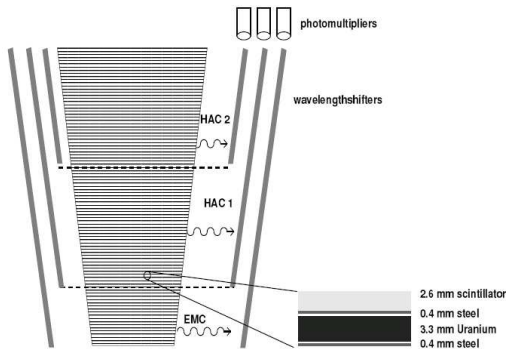
Figure 2.12: Sketch of the composition of a CAL module, showing electromagnetic (EMC) and hadronic sections (HAC). From [12].

The thickness of the absorber and of the active material were selected in order to have linear and equal response for an electron or a hadron of the same energy ($e/h = 1.00 \pm 0.02$) passing through the detector. This mechanism is called *compensation*, and allows to achieve good resolution in the determination of both the electromagnetic and the hadronic energy. The electromagnetic resolution of the ZEUS calorimeter was:

$$\frac{\sigma(E)}{E} = \frac{18\%}{\sqrt{E}} \oplus 2\%, \tag{2.4}$$

where E is the particle energy measured in GeV, while the hadronic resolution was:

$$\frac{\sigma(E)}{E} = \frac{35\%}{\sqrt{E}} \oplus 1\%. \tag{2.5}$$
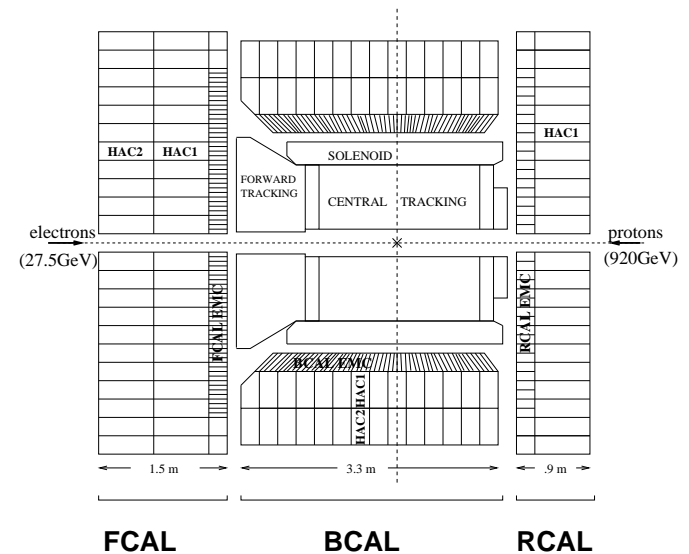
Figure 2.13: Diagram of a longitudinal cut of the calorimeter showing 3 regions: forward (FCAL), barrel (BCAL) and rear (RCAL).

The CAL was divided into three parts, the forward (FCAL), barrel (BCAL) and rear (RCAL) calorimeters, as displayed in Figure 2.13. Since most of the final state particles were boosted into the forward region, the three parts had different thicknesses. FCAL was $\sim 7\lambda$ thick, BCAL $\sim 5\lambda$ and RCAL $\sim 4\lambda$, where λ was the interaction length. Each part of the calorimeter had a modular structure. Up to 185 layers of absorber plus scintillator form the calorimeter *modules*, with each module segmented into *towers*, which were further segmented into one electromagnetic (EMC) and two hadronic (HAC) sections (RCAL had only one hadronic section). These sections were made up of *cells*, whose sizes depended on the type and its position in the CAL as shown Table 2.4.

CAL section	Angular coverage	EMC $x \times y$	HAC $x \times y$
FCAL	2.5° - 39.9°	$20 \times 5\,\mathrm{cm}^2$	$20 \times 20\,\mathrm{cm}^2$
BCAL	36.7° - 129.2°	$20 \times 5\,\mathrm{cm}^2$	$20 \times 20\,\mathrm{cm}^2$
RCAL	128.1° - 178.4°	$20 \times 10\,\mathrm{cm}^2$	$20 \times 20\,\mathrm{cm}^2$

Table 2.2: Angular coverage of the CAL sections and dimensions of the cells at their front side.
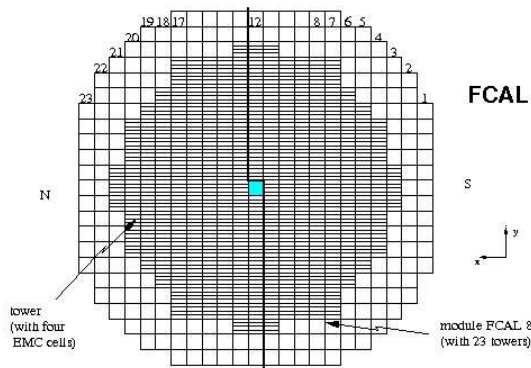
Figure 2.14: View of FCAL from the interaction point.
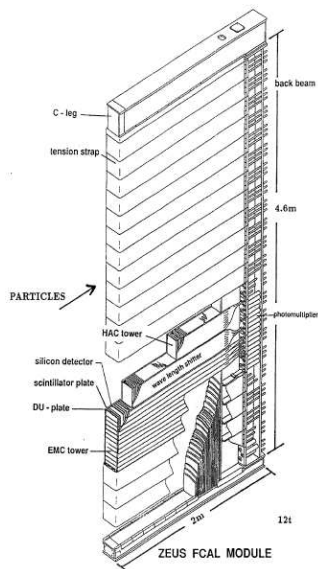
Figure 2.15: Structure of one FCAL Module.

The FCAL structure is shown in Figure 2.14. A module is indicated and its layout is shown in Figure 2.15. The RCAL structure was similar. The total number of modules in each was 23 (32 in BCAL). The centre module, number 12, was divided into two parts, top and bottom, to allow the beam pipe access into the detector. Another feature of FCAL and RCAL is that they were divided into halves (denoted as solid lines in the Figure) and could be pulled back from the interaction region during beam injection in order to mitigate the effects of radiation on the scintillator and electronics.

At each calorimeter cell, the light produced in the scintillator material was read out via wavelength shifters on both sides of the cell. A photomultiplier tube (PMT) was connected to each wavelength shifter, therefore every single cell was measured by two photomultiplier tubes. Not only the signal of each cell was measured, also the arrival time of the pulse was recorded with a precision of few ns. The PMT high voltages were set individually at ∼1200 V. There were nearly 6000 cells in the calorimeter and therefore about 12000 channels to read out.

2.5   Muon detectors

The muon detectors were designed to measure the tracks of particles coming from the interaction region, which were able to cross the whole calorimeter and the iron yoke. The muon detection system, like the other ZEUS components, took into account the boost of the particles into the forward direction. Therefore the muon system was split into two detectors: the Forward Muon detector (FMUON) and the Barrel and Rear Muon detector (BMUON and RMUON).

2.5.1   The Forward Muon Detector

The forward muon detector [7] was divided into two regions (Figure 2.16). The inner region, called FMUI, located between the FCAL and the BAC, the other was the FMUO, placed outside the BAC. The FMUON detector consisted of:

- four planes of limited streamer tube trigger planes (LST1-LST4) with digital readout in ρ and ϕ,

- two planes of limited streamer tubes with digital (ρ, ϕ) and analog ρ readout in the large polar angle region (LW1, LW2),

- four planes of drift chambers (DC1-DC4),

- two large toroidal iron magnets providing a magnetic field of 1.7 T for the momentum discrimination and measurement in the angular region $5° < \theta < 16°$.

The first streamer plane (LST1) and the first drift chamber (DC1) maked up the FMUI detector, the rest of the system was placed outside the iron yoke. The individual components of the FMUON detector are described below.

The limited streamer tubes (LST) planes

The aim of the LST planes was to trigger on muon candidates and to reconstruct their position in terms of the azimuthal and radial coordinates of the track. A trigger plane was made of four LST chambers, grouped by two in two half-planes. A quadrant consisted of two layers of LST, positioned horizontally inside a plastic sheet. The tubes of the two planes were slightly displaced (0.5 cm) in order to achieve a complete geometrical acceptance. Each quadrant was contained in an aluminium air tight box. The signals generated by the LST were induced on copper strips, glued to the outer side of the plastic sheet. There were 132 radial strips, 1.9 cm wide, and they were divided along the bisector of the quadrant so that the simplest unit of the trigger plane to be read was the octant. The number of ϕ strips was 32 per octant. Each strip covered an interval of 1.4° in the azimuthal angle.
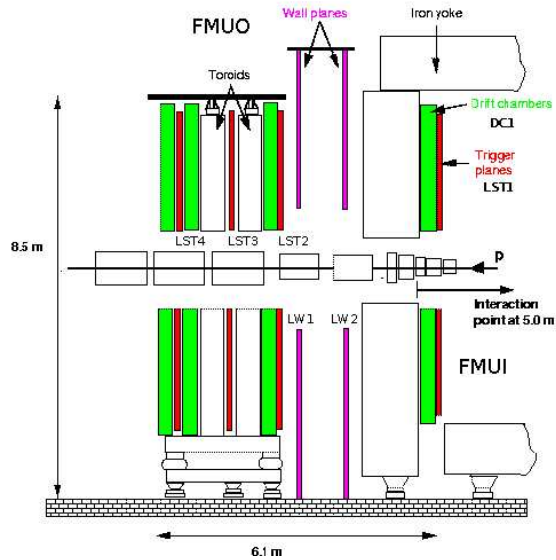
Figure 2.16: Schematic view of the forward muon detector along the beam axis.

The drift chambers

The drift chambers were needed in order to obtain good momentum resolution. Each plane consisted of four chambers grouped into pairs in two half planes fixed on a support panel. The basic element of the chamber was the *cell*, made of four sense wires together with the layers needed to generate the appropriate magnetic field. The sense wires measured the radial coordinate, and the information was sent to a TDC which converted them into a time interval related to the drift distance.

The large angle coverage planes

The two large angle coverage planes (LW) were needed in order to achieve the desired geometrical acceptance also in the region left uncovered by the toroids ($16° < \theta < 32°$). Each plane consisted of eight air tight aluminium wrappings that contained a LST layer. The LST signal was induced on copper strips with radial geometry spaced $0.7°$ in the ϕ coordinate and 1.8 cm in the ρ coordinate. The number of ϕ strips was 64 per octant while the ρ strips were 192 per octant. The achieved resolution in ρ, using a center of gravity algorithm, was $\sim 1\%$.

2.5.2   Barrel and Rear Muon Chambers

The barrel and rear muon detector [13] had to cover a very large area, so a modular structure was chosen. The basic element was the *chamber*. The chambers which covered the inner barrel part between BCAL and the iron yoke are called BMUI, whereas the chambers situated in the outer barrel part, outside the yoke, are denoted as BMUO. In a similar way, in the rear region the detector was divided into RMUI and RMUO chambers.

The layout of B/RMUON is displayed in Figure 2.17. The chambers had different shapes and dimensions depending on their location, but its internal structure was the same for all: the element bearing the weight of the chamber was an aluminium honeycomb structure, 20 cm thick in the rear chambers, 40 cm in the barrel ones. On both sides of the honeycomb a couple of LST planes was placed. Each tube contained eight cells, each with one sense wire; the distance between two sense wires was 1 cm. During data taking these were set to ~ 4500 V so that they could behave as anodes, while the inner cells walls covered with graphite, act as cathodes. The cells were filled with a mixture of carbon dioxide (CO_2), Argon and Isobutane. On one of the outer walls of the LST plane constructive strips orthogonal to the wires were placed. The distance between two adjacent strips was 1.5 cm. The signal read by the wires was also induced on the strips, so that a single plane of wires and strips was sufficient to determine the particle position. For redundancy each chamber had two LST planes on each side. The cells in one plane were displaced with respect to those in the other plane by half cell, to have also good acceptance for particles passing near the boundary of two cells in a plane.
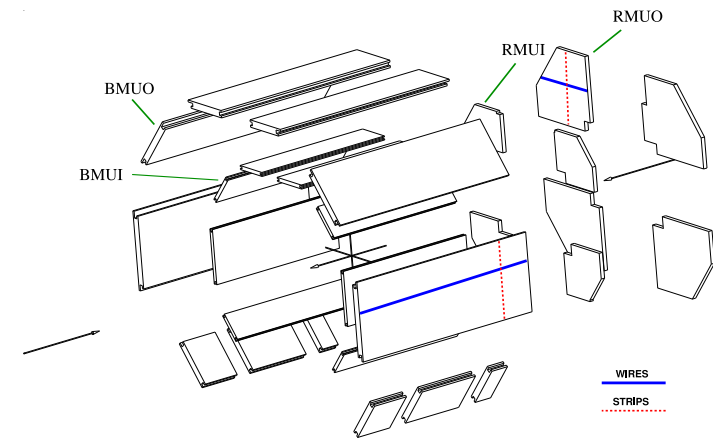
Figure 2.17: Blowup of the layout of the barrel and rear muon chambers.

2.6   Backing Calorimeter

The Backing Calorimeter (BAC) [14] was built to fulfil two tasks: to preserve hermetic hadron jets energy measurement and to aid tracking of muons passing through the iron yoke of the detector.

To measure the energy of hadron shower leakages out of the central uranium calorimeter and to correct jet energy measurements, the BAC detector was equipped with an analog readout, giving precise information on the deposited energy but only approximate position information. To enable muon tracking in the iron yoke the complementary digital readout (the so called HIT readout) was designed, giving basically no information about the deposited energy, but exact position in two dimensions. This information can also be used for better positioning of shower leakages and for discrimination between leaking hadron cascades and muons.

The BAC modules consisted of 7-8 tubes, called *channels*, with a cross section of $11 \times 15\,\mathrm{mm}^2$ and 1.8-7.3 m long. At the centre of the tubes, gold plated tungsten wires with a diameter of 50 μm are placed, supported every $\sim 50\,\mathrm{cm}$ in the z-direction. On the top of the modules aluminium cathode pads, 50 cm long, were located. The wires were read out on one side and provide both analog and digital signals, whereas the pads had analog read out only. The wires were grouped into *towers* of a width of $25 - 30\,\mathrm{cm}$ (2-4 modules) over the full depth of the BAC.

The energy measurement was done by summing up the analog signals from the wires. The pads of 2-4 neighbouring modules were added to pad towers with an area of $50 \times 50\,\mathrm{cm}^2$ (4 modules) similar to the wire towers. They provided a measurement of the location of the energy deposit along the wires (i.e. in the z-coordinate). The signals from the wires were also used to measure patterns of hit positions in the BAC which were used to reconstruct muon trajectories. The energy resolution determined by test beam measurement is:

$$\frac{\sigma_E}{E} = \frac{1.1}{\sqrt{E}},$$
(2.6)

where E is the particle energy in GeV.

2.7   Luminosity measurement

The luminosity [15] delivered at ZEUS was determined by measuring the Bethe-Heitler QED Bremsstrahlung process $ep \rightarrow ep\gamma$ [16], where the lepton and the proton were scattered at very small angles. The cross section of this process can be calculated differentially as function of the photon energy with an accuracy of 0.5%. Thus a precise measurement of the rate and energy of the Bremsstrahlung photons allowed an accurate determination of the ep luminosity.
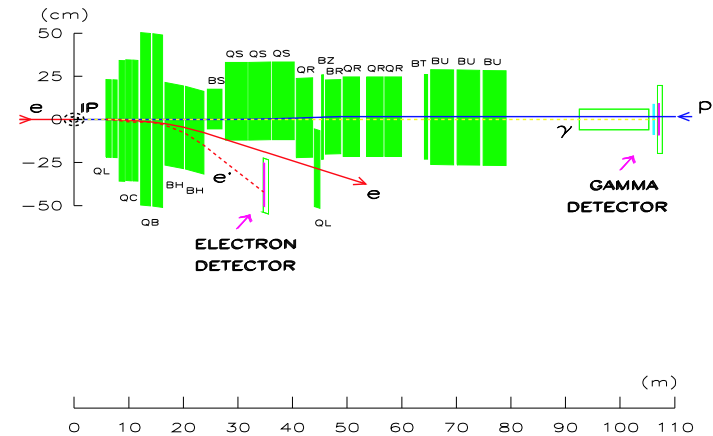
Figure 2.18: Luminosity system.

The luminosity monitor consisted of a pair of calorimeters: a photon and a lepton calorimeter, located along the beam line at $z = -106\,\mathrm{m}$ and $z = -35\,\mathrm{m}$ respectively (Figure 2.18). To protect the photon calorimeter against synchrotron radiation it was shielded by a carbon-lead filter. The resulting calorimeter resolution was $\sigma(E)/E = 23\%/\sqrt{E}$, where E is measured in GeV. The Bremsstrahlung event rate was determined by counting the number of photons above a fixed energy threshold. The luminosity was then calculated by dividing the measured rate by the Bremsstrahlung cross section corrected for detector acceptance. The main contribution to the background was given by the Bremsstrahlung of leptons of residual gas in the beam pipe. This was estimated using *pilot bunches*, i.e. lepton bunches with no paired proton bunches, evaluating for these the rate of Bremsstrahlung events. The achieved precision on the luminosity measurement was of the order of $1.5 - 2\%$.

For this work data from the years 1996 to 2000 was used. The integrated luminosity delivered by HERA and the usable for ZEUS physics analysis is displayed in Figure 2.19.

2.8   Trigger system and data acquisition

The bunch structure of the beams at HERA produced a beam crossing every 96 ns, corresponding to a rate of potentially interesting events of 10.4 MHz. The rate of ep events was in the range from about 0.1 Hz for NC DIS events with $Q^2 > 100\,\mathrm{GeV}^2$ up to 240 Hz for soft photoproduction vector meson production (for an instantaneous luminosity of $2 \times 10^{31}\,\mathrm{cm}^{-2}\,\mathrm{sec}^{-1}$). The rate of background events, on the other hand,
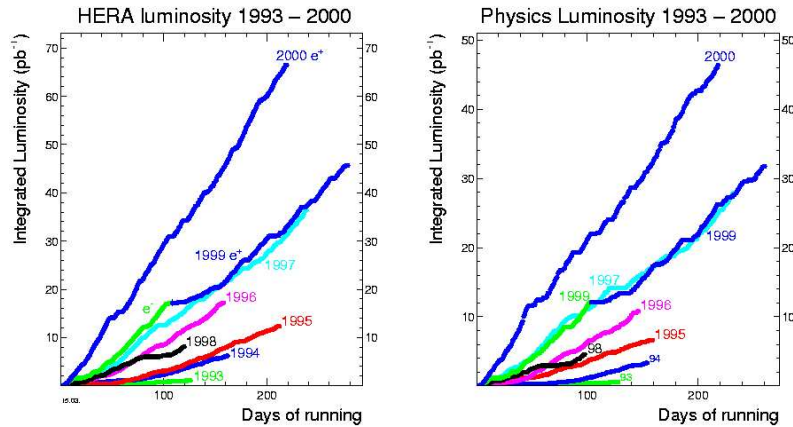
Figure 2.19: Integrated luminosity delivered by HERA (left) and usable for ZEUS physics analysis (right) in the 1993-2000 running period.

exceeded the rate of physics events by several orders of magnitude: interactions of the leptons or protons with the residual gas nuclei or elements from the beam line (beam gas events) typically occurred at a rate of 10 kHz and an additional background was given by cosmic ray muons passing the CTD. The total data size per event was of the order of $\mathcal{O}(10^5)$ byte, while the writing speed was limited to $\mathcal{O}(10^6)$ byte per second. Hence a significant reduction of the data rate and size was required.

The ZEUS trigger was a sophisticated three-level system [7, 17], designed to select events online, as illustrated in Figure 2.20. The complexity of the trigger decisions increaced from level to level, while the data throughput was reduced.

2.8.1   First level trigger

Each component of the ZEUS detector was equipped with its own first level trigger (FLT), implemented in hard-wired logic circuits. Each FLT provided a fast trigger decision based on properties as energy sums, thresholds or timing information, and passed it onto the global first level trigger (GFLT) while the event data was stored in pipelines. By combining different trigger slots a decision was made by the GFLT after $\sim 4.4\,\mu s$ and the accepted event was passed to the next trigger stage. The trigger processing for all components was pipelined and deadtimeless, accepting data from a bunch crossing every 96 ns. The typical GFLT output rate was below 1 kHz.
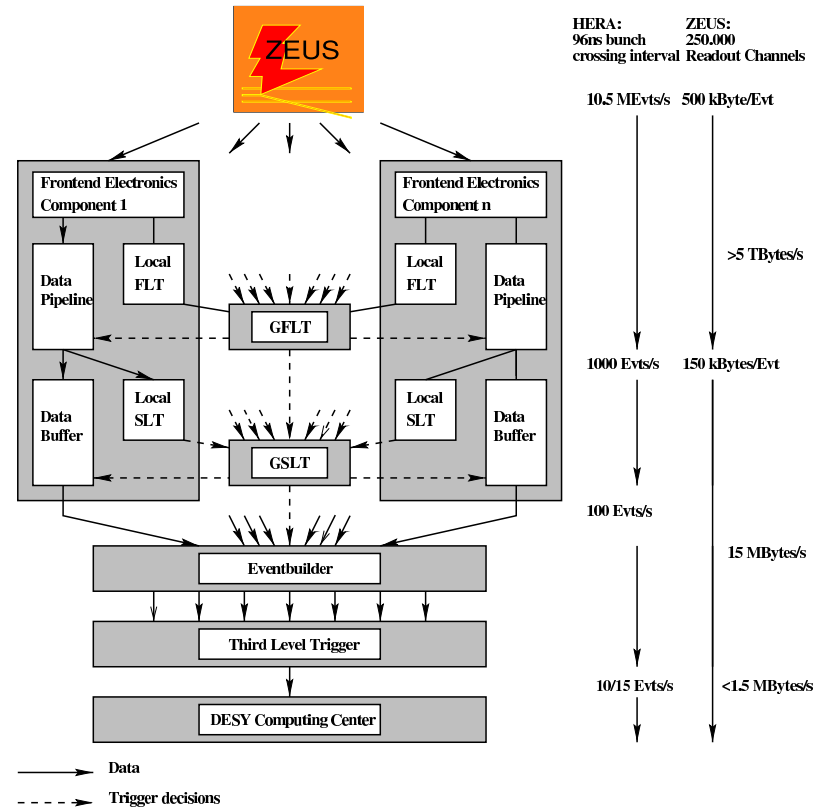
Figure 2.20: The ZEUS trigger and data acquisition system.

2.8.2 Second level trigger

The second level trigger (SLT) was implemented in a transputer network. The decision of the GFLT was analysed further and the event quantities were recalculated to a higher degree of precision. Beam gas background was rejected on the basis of CAL timing information, which was available at this stage. The decisions of several branches of the SLT were collected by the global second level trigger GSLT, which provided a decision after 7 ms, reducing the event rate to 50-100 Hz. For GSLT accepted events, the data of all components was combined into a single record of ADAMO [18] data base tables by the event builder and passed to the third level trigger. The GSLT was supplemented by an additional tracking trigger in 2001, called global tracking trigger (GTT).

2.8.3 Third level trigger

The third level trigger (TLT) used a computer farm for the analysis and classification of each event. Based on physical quantities of the fully reconstructed events, such as kinematic variables, output of electron and muon algorithms, topologies of hadronic final states, etc., a decision was made and the accepted events were classified. After having accepted the event, the TLT sent the data via an optical link to the DESY computing centre. There, accepted events (with a size of approximately 100 kB) were written to tape at a rate of 5-10 Hz and fully reconstructed offline by the ZEUS software.

Chapter 3

Calibration and data quality monitoring of the calorimeter

In this chapter an explanation of the calibration procedures of the calorimeter will be given. A technical review can be found in [19]. The calibration and maintenance of the ZEUS calorimeter was the responsibility of the Data Quality Monitoring (DQM) experts of the component. Part of this thesis work was devoted to this task.

The aim of the calibration of the ZEUS calorimeter was to get rid of systematic biases and improve the accuracy of the component. The monitoring of the quality of CAL data allowed to recognise problems and had a fast reaction in case a hardware piece needed to be exchanged. Due to the effort of the DQM crew, the calorimeter had a very good performance over its long operation time and the calorimeter was one of the most reliable components of the experiment.

The role of the DQM expert was to be the on-call person for one-week shifts, day and night. The CAL shifter performed sets of calibrations, updates of constants, online and offline checks, helped to identify CAL related problems, and contributed to its maintenance. During some parts of the calibration one important requirement was not to have beams in HERA. A good coordination with the HERA and ZEUS crews was therefore necessary to determine the time available for calibration. The DQM expert provided some judgement as to how much time needed to be allocated for the calibration. At the end of the shift, a report was presented to the CAL group and the shifter also attended the ZEUS components meeting to report of the CAL activities during that week.

To understand the different steps in the calibration it is necessary to also understand the data acquisition system (CalDaq) [19] of the calorimeter. During the HERA I running period the CalDaq provided data acquisition to not only the ZEUS

uranium scintillator calorimeter, but also to other components like the small rear tracking device (SRTD), the forward neutron calorimeter (FNC), the proton remnant taggers (PRT), the LED system (LED) and the laser table diodes (LASER).
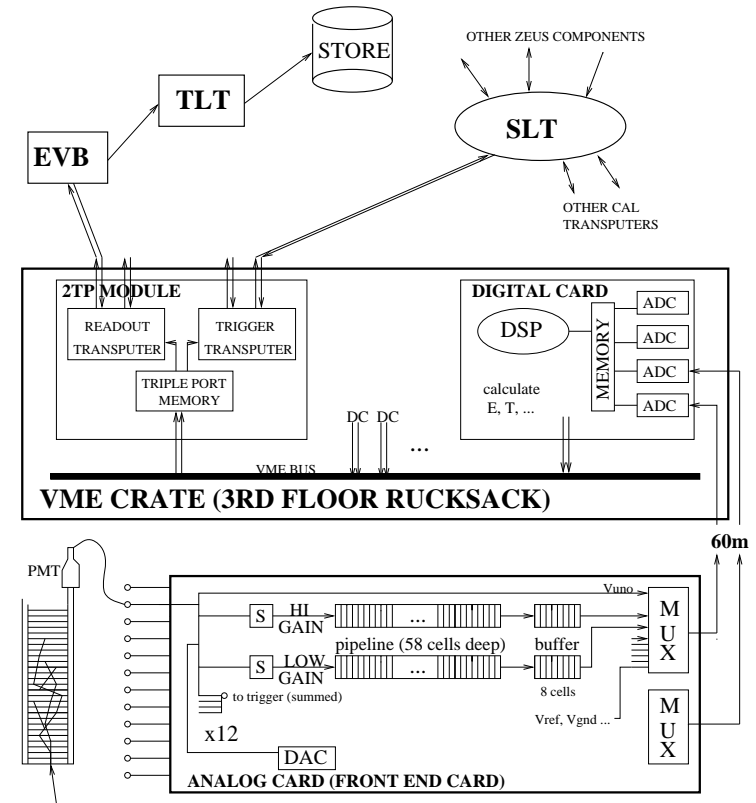
Figure 3.1: Sketch of the CAL readout chain from energy deposit in a cell to mass storage and trigger system.

The readout chain [20] for the calorimeter is displayed in Figure 3.1, and can be explained as follows: The signals from the PMTs were sent into the front-end analog electronics where they were sampled and pipelined every 96 ns. When an event was accepted by the trigger, the samples were stored in the buffer and then read out (multiplexed or MUXed) and sent to the ADCs in the digital cards (which were

located in some 40 VME transputer crates on the rucksack). There, the samples were digitalised and stored in the DSP (Digital Signal Processor) memory. They were then corrected with the calibration constants downloaded at the start of the run, and analysed by the online DSP code to produce an energy and time for each channel. The resulting data was finally read out from the digital cards via the transputer network. Note that the calibration constants used by the DSP codes are a crucial part of the CalDaq. Hence the procedure to obtain these constants will also be described here.

During ZEUS data taking there were calibration tasks which should be done daily, and some others on a weekly basis, as will be explained next.

3.1   Daily calibration
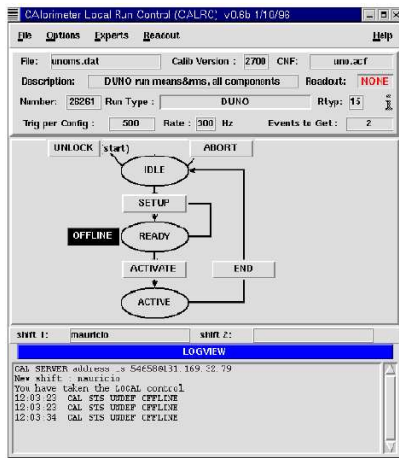
Figure 3.2: CAL Run Control panel.

For most of the calibration tasks no beams had to be in HERA. A valid calibration had to be done with the solenoid and the yoke magnetic fields on and the CAL closed. This was to recreate the standard situation of the ZEUS experiment during HERA running. If the magnetic field was just raised, the calorimeter should have gone through the hysteresis training procedure, i.e. three cycles of opening and closing.

The CAL expert had to agree with the ZEUS crew to take the CAL *offline*, i.e. to excluded it from ZEUS data taking, and to use the CAL readout. The CAL run control was a graphical interface for passing commands and parameters to the CAL readout system and monitoring the progress of a run. The CAL run control panel is displayed in Figure 3.2.

During data taking the daily calibration consisted of a set of checkout runs, update of bad channels list, ADC-to-Volt, UNO scale factors, LED and laser and finally CAL subcomponents checkout. The most relevant ones for the calibration procedure will be described next.

- **Checkout runs: UNO, QINJ, PED runs with dummy constants.**
  Since each calorimeter cell was readout by two photomultipliers, the readout from a single PMT was named a *channel*. The check out runs helped the experts to find hardware problems, they used a version (set of calibration constants) without any bad channels and the real state of the CAL could be derived from this. If no problems were found after the analysis of these runs, an *internal* CAL calibration version was created. The different checkout runs can be described as follows:

  – **Charge injection on the Analog Cards (QINJ).**
    Control signals were sent directly to the Front End card to test the behaviour and response of the electronics without the presence of signals in the photomultipliers coming from physics events. As it is shown in Figure 3.1, each front end card received the signal of 12 PMTs. Therefore, if in a QINJ run a group of 12 channels failed this was an indication of a brocken card, as seen in Figure 3.3.
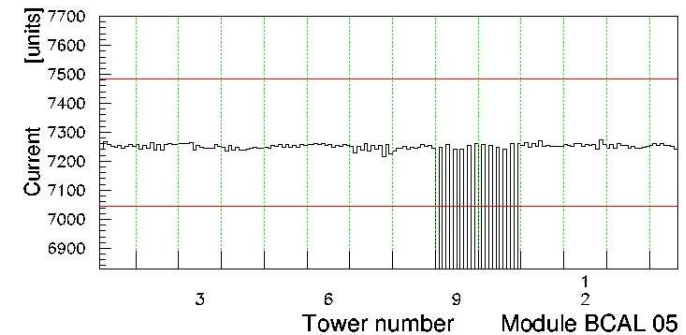
Figure 3.3: QINJ mean energy vs channel for BCAL module 05. The 12 channels with no signal were an indication of a brocken analog card.

  – **Uranium noise currents signals for each photomultiplier (UNO).**
    The signal from the natural radioactivity of the Uranium that was measured in the photomultipliers was low enough not to interfere significantly with the energy measurement of particles coming from physics processes, yet high enough such that the measurement of this activity allowed an accurate determination of the PMT gains (Figure 3.4). Therefore the UNO checkout runs complemented the QINJ runs, which tested only the front end and digital cards, whereas UNO runs tested in addition the functionality of the photomultipliers.
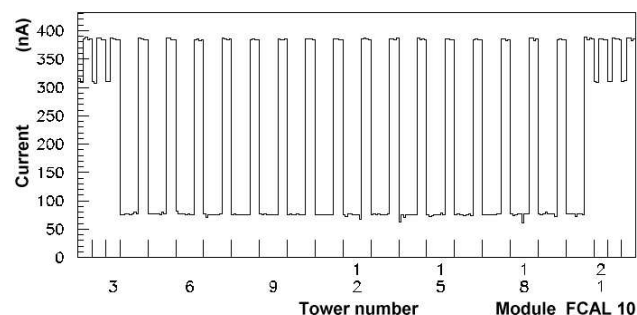
Figure 3.4: Uranium signal from module FCAL 10 without beams in HERA. In each tower the size of the cells is clearly visible. The EMC cells are smaller, therefore the signal coming from them is smaller; the HAC cells give a stronger signal.

– **Pedestals (PED).**
Analog electronics always has an output signal even when no signal is present at input. In the CAL there was a signal at input, namely the one produced by the PMTs if their high voltage was switched off (or reduced to 400 V). Its value was more or less constant but it shifted a little with time. Therefore, corrections for this effect were needed.

• **Update of bad channels list.**
After the above described checkout runs with dummy constants were taken, and checked that the general state of the CAL was good, a new set of the checkout runs was taken. This time using the internal CAL calibration version or using a so-called CAL_QUICK_CALIB run taken by the ZEUS crew. The bad channels found were put into the calibration constants formatted for the DSP (see Figure 3.1). The new version containing the new constants (*main version*) was uploaded to be used for ZEUS data taking.

• **Update of ADC-to-Volt calibration constants.**
The scale factors to calculate energy from ADC counts are called ADC-to-Volt constants. There was a well-known problem in the CAL readout where, over a long period of time ($\sim$ few days), the gain for a random set of six channels associated with one ADC drifted. This effect was observed when the average energy of a charge injection run (QINJ) for those channels was a few percent lower or higher than for its neighbours. Such a drift in the ADC-to-Volt values leaded to a drift in the energy measurement of physical processes. Sometimes this drift was significant enough such that without corrections those channels were considered as bad according to the data quality cuts. The ADC-to-Volt procedure allowed to correct this problem daily without doing a full calibration.

• **Update of UNO scale factors.**
After a main version was generated and uploaded, the update of UNO scale factors was done. Then a new UNO run was taken and it was compared to a previous run to look for one or several modules which had not set their HV properly. If no problems were found, the last UNO run was used for the update of the scale factors.

3.2   Once a week

• **Complete calibration of the front-end electronics.**
Since the Full Electronics calibration procedure required to have the CAL run control over more than one hour, this procedure was done during planned ZEUS data taking breaks. The calibration was done with magnets on and the CAL closed but with no beams in the machine, because this could affect the pipeline and UNO samples read out during the calibration runs. Also, the front-end was allowed to warm up if the power was just turned on ($\sim$ 45 min). The first task was the update of the bad channel list as explained before. At this step many channels were flagged bad because these dummy constants contained no information about bad channels; the focus was instead on the mean energy distributions, and try to look for major problems like HV off, dead front-end cards, etc. If problems were found the CAL-DQM expert could try to debug and –if possible– fix bad channels, as will be explained in the following section. Next, a new set of calibration runs was taken and the new constants formatted.
After an access to the detector the time offsets for the analog front end cards had to be updated, and a trimming was also done, if necessary (see below).
An additional set of UNO, QINJ and Pedestal checkout runs was taken, using a new CAL internal calibration version, and after the bad channels list was updated, the main calibration version was installed.
The last step of the calibration was the update of the UNO scale factors. Finally, the CAL readout was sent back online.
A short report was written in the ZEUS e-logbook containing the following info: created new version number, number of bad channels, number of holes (cells for which both readout channels failed), as shown in the next example:

```
Total number of CAL bad channels for version 3258 is 220
They break down as follows:
          FCAL    BCAL    RCAL    Total
  FEC     37      1       8       46
  UNO     44      77      20      141
  Qinj    9       3       1       13
  PED     14      6       0       20
Total     104     87      29      220
```

```
The total number of holes in the CAL are:
Ca Crt Crd Chn Poser Mod Tow Typ Sid   Code Message
 f  11  14  17   EEE   8  15   7   0    4001 UNO mean is high
 f  11  14  23   EEF   8  15   7   1    4005 UNO mean is too low
1 holes
```

- **Trimming the high voltage setting for the photomultipliers**
  Trimming the high voltage settings for the ZEUS calorimeter was required to ensure that the right energy scale was present for the calorimeter triggers. The calorimeter first level trigger, for example, did not get the UNO scale factors, which were sent offline for the calorimeter reconstruction. It therefore relied on the assumption that the PMT voltages were set correctly.

  Trimming the PMT voltages was an iterative procedure involving measuring the uranium noise through each PMT, comparing the measured values with nominal values, calculating a new set of HV settings, loading the settings, remeasuring the uranium noise, and so on. The best time to retrim was in the middle of a full calibration, after the calibration runs were taken, but before the UNO check-out run. This was to guarantee that all bad UNO channels got retrimmed back to good values.

3.3   Data quality monitoring

In addition to the online checks by the ZEUS shift crew, the quality of the CAL data was monitored daily, online and offline by the CAL DQM crew. Online checks allowed immediate monitoring of problems like high voltage trips and readout errors. The results from the offline checks were used to improve the list of bad channels to be excluded from the offline analysis.

When a problem was found, either offline or during calibration, the CAL disposed of histogram viewers (CAW, DQMCOC, ZMON) which were specially developed to debug CAL related problems. CAW, for example, is a PAW (Physics Analysis Workstation [21]) version with several calorimeter specific extensions. Among these extensions are cable maps, shared memory tools, and HV utilities.

Here some common problems are described with their probable source and solution:

- Noisy cells:
  There were several sources for noisy cells (Figure 3.5). These appeared mainly due to brocken hardware but also when the HV of the photomultiplier was not set to its nominal value or when the calibration version was some days old.
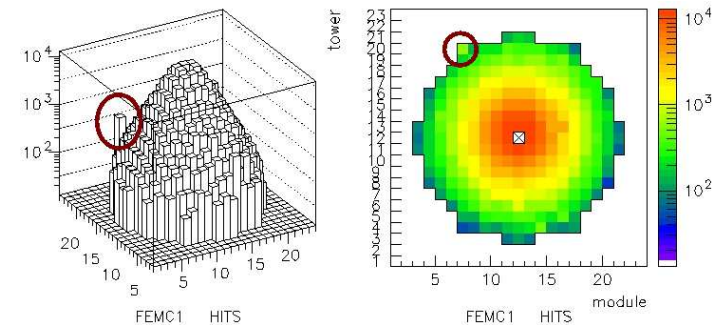
Figure 3.5: A noisy cell found using the CAW histogram viewer. The left figure shows a 3D plot of the hits in the module FEMC1, and the right plot a view from the interaction point. In both cases the noisy cell is marked with an ellipse.

Solution: A full electronics calibration recovered a big fraction of the noisy cells, and those which were not recovered were flagged as noisy. Typically $\sim 2\%$ of the 11836 readout channels were flagged after the calibrations and the data quality monitoring.

- Holes
  The number of cells for which both readout channels failed were, in general, less than two in the whole calorimeter.
  Solution: In some cases if one of both channels persisted as noisy after the full electronics calibration and trimming, then the faulty PMT was exchanged.

- Bad Module
  If a module seemed to be totally or partially off, as shown in Figure 3.6, it could have been a timing error.

  Solution: The connectors on the detector for that module could not be properly plugged. This happened e.g. during the hysteresis process.

- Group of 6 bad channels:
  There were two possibilities: a failed ADC on the Digital Cards (in the Rucksack), or a failed buffer chip (on the front end).
  Solution: They were distinguished by checking the Digital Card and running the CAL readout in debug mode while looking at the signal coming from the detector with the oscilloscope. A Digital card or ADC was exchanged easily. In the case that no signals were present in the oscilloscope the problem was probably a failed buffer chip on the detector. To fix this, an access to the detector was needed.
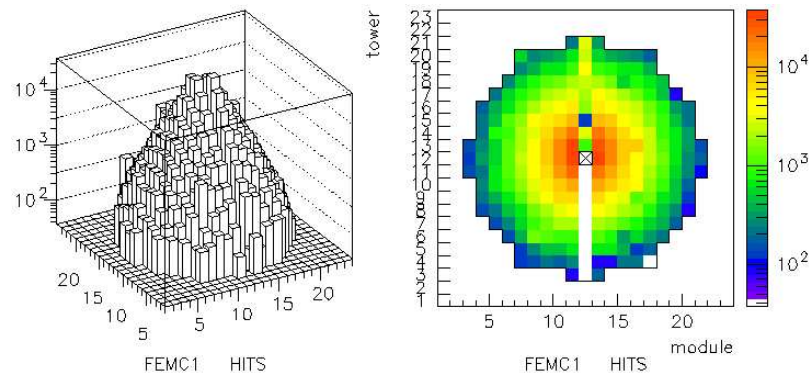
Figure 3.6: Here module 12 of FEMC1 had a problem with the clock, such that the upper part of the module had signals while the lower part was off.

- Group of 12 bad channels:
  Failed analog card (on the front end), as explained in Figure 3.3.
  Solution: The card had to be replaced during an access.

- Group of 24 bad channels (generating 12 holes):
  Failed digital card (in the Rucksack).
  Solution: If the card seemed fine from the check_dc point of view, another test was possible: Exchanging the signal cable to the probably faulty digital card with the cable going to one of the digital cards beside the suspicious one. Then another run was taken and if the 24 bad channels did not move to another place, the digital card was replaced.

3.4   Conclusion

Strict rejection criteria based on the weekly electronics calibration and the daily measurements were used to generate the list of channels to be excluded from –all– ZEUS physics analyses. The data obtained with the ZEUS calorimeter is therefore of very high quality and the calorimeter remains as one of the most reliable components of the experiment for physics analysis. Therefore, later in this work calorimeter variables will be used as discriminators in the implementation of a new electron finder (See Chapter 7).

Chapter 4

Theoretical framework

This chapter summarises the theoretical framework of the HERA physics relevant for this work. An overview of the Standard Model of particle physics opens this chapter, followed by the description of the kinematics in electron-proton scattering. A discussion of heavy flavour production and evolution is also presented.

4.1 The Standard Model

Our current understanding of the structure of matter is based on the Standard Model (SM) [22] of particle physics. This theory gives a simple and very satisfactory description of the known phenomena.

The SM is a quantum field theory. In this formalism, particles are described by functions of space-time coordinates, called *fields*, which can be considered as generalised coordinates of a Lagrange formalism [23]. Interactions between particles are represented by gauge transformations under which the corresponding Lagrangian density function is invariant. The symmetry resulting from this invariance is based on the gauge symmetry of the unitary groups $SU(3) \otimes SU(2) \otimes U(1)$, which is used in the SM to model the interaction among particles.

The elements forming the SM are 12 spin-$^1/_2$ fermions (leptons and quarks), as summarised in Table 4.1, with their corresponding antiparticles; and the integer-spin bosons mediating the fundamental forces, listed in Table 4.2.

At the beginning of the universe the amount of particles of each family was very similar. Nowadays, normal matter is made from particles of the first generation: the up (u) and down (d) quarks, which build up partons in the atomic nuclei, and electrons (e) which belong to the first lepton family. The rest of the particles, even if they are not stable and decay very fast, can still be produced in accelerators like

	Generations			Interactions		
	1	2	3	electron.	weak	strong
Leptons	e	μ	τ	-1	yes	no
	ν_e	ν_μ	ν_τ	no	yes	no
Quarks	u	c	t	2/3	yes	yes
	d	s	b	-1/3	yes	yes

Table 4.1: The SM fundamental particle spectrum, grouped in three generations, and their interactions.

HERA. The study of the production and decay of the quark **beauty** (b) and the comparison with theoretical predictions is the main topic of this thesis.

In the SM the **strong interaction** is modelled by Quantum Chromodynamics (QCD) [24], a gauge theory where the symmetry group is SU(3). The resulting gauge bosons (*gluons*) are massless and electrically neutral forming a colour octet. They come in 3 different charges (colours), red, blue and green (and the corresponding anticolours for the antiparticles). The **electroweak theory** by Glashow, Salam and Weinberg (GSW) [25], describes the electromagnetic and weak interactions using the symmetry group $SU(2) \otimes U(1)$. The electromagnetic interaction is carried by the photon: γ; and three massive gauge bosons are responsible for the weak force: the electrically charged $W^\pm$ and the neutral Z particle. The charges of the unbroken symmetry theory are the Isospin I for the $SU(2)$ sector and the hypercharge Y for the U(1) case.

Interaction	Theory	Symmetry	Gauge boson	Charge	coupling α_i
Strong	QCD	SU(3)	gluons $g_1 \cdots g_8$	colour	$0.1 - 1$
Electromagnetic	QED	U(1)	Photon γ	electric charge	1/137
Weak	GSW	SU(2)	$W^\pm, Z$ (H?)	weak isospin	1/30 (at M_W)

Table 4.2: The fundamental forces included in the Standard Model. The fourth fundamental force –Gravity– is not included.

The Higgs boson has never been observed in experiments, and finding it is a major goal in experimental particle physics today. The coupling of the Higgs field with the W and Z bosons would generate the masses of the weak bosons through spontaneous symmetry breaking ($M_W = 80.41$ GeV, $M_Z = 91.187$ GeV) whereas the photon remains massless.

Tipically predictions for particle interactions in the SM are expressed as power series expansions in coupling constants α_i. At low energies the SM has no internal inconsistencies using this perturbative approach and agrees with experiments. Even the neutrino masses –which were recently discovered to be different from zero [2]– can be included in an extension of the SM without many difficulties. Nevertheless, the SM is not the definitive theory. There are some windows in the phase space that have not been, or can not be explored, such as extremely weak couplings or extremely rare decays. Probably the most important limitation is the energy scale up to which the SM can be tested.

The SM –assuming that the Higgs boson is found, as expected, at the new pp collider LHC at CERN– still does not describe those phenomena involving gravity. Gravity is not yet incorporated as a quantum theory, and so far Standard Model and General Relativity could not be combined to give a coherent description of nature at any given energy scale. However, for the accelerator experiments the problems associated with quantum gravity are irrelevant until the Planck scale $\Lambda_{\text{Planck}} \sim 10^{19}$ GeV is reached. Before that energy, the effect of gravity is negligible. Only at energies of the order of the Planck scale gravity could be as strong as the other interactions.

4.2   Quantum Chromodynamics

In QCD the Lagrangian describing the interactions of quarks and gluons is (up to gauge-fixing terms)

$$\mathcal{L}_{\text{QCD}} = -\frac{1}{4}F^{(a)}_{\mu\nu}F^{(a)\mu\nu} + \mathrm{i}\sum_q \bar{\psi}^i_q \gamma^\mu (D_\mu)_{ij}\psi^j_q - \sum_q m_q \bar{\psi}^i_q \psi_{qi}, \qquad (4.1)$$

where the field strength tensor $F^{(a)}_{\mu\nu}$ is given by:

$$F^{(a)}_{\mu\nu} = \partial_\mu A^a_\nu - \partial_\nu A^a_\mu - \alpha_s f_{abc} A^b_\mu A^c_\nu, \qquad (4.2)$$

and the covariant derivative has the form:

$$(D_\mu)_{ij} = \delta_{ij}\partial_\mu + \mathrm{i}\alpha_s \sum_a \frac{\lambda^a_{ij}}{2} A^a_\mu. \qquad (4.3)$$

Here α_s is the QCD coupling constant, and the f_{abc} are the structure constants of the SU(3) algebra. The $\psi^i_q(x)$ are the 4-component Dirac spinors associated with each quark field of colour i and flavour q, and the A^a_μ are the eight Yang-Mills (gluon) fields. Being not colour neutral themselves, the gluons can also interact with each other.

The self coupling of the gluons leads to the property of *asymptotic freedom*, which states that the interaction strength of two coloured objects increases with the distance between. This property has been proven rigorously and determines that the QCD coupling is small only at high energies, and it is only in this domain that high-precision tests, similar to those in QED, can be performed using perturbation theory (pQCD). For lower energy scales one has to rely on non-perturbative QCD models.

Another property of QCD is *confinement*, which keeps quarks bound into colourless objects and prevents the observation of free quarks. Quarks or gluons within bound states are generally called *Partons*, and *Hadrons* are colour-singlet combinations of quarks, antiquarks, and gluons (e.g. mesons: $q\bar{q}$ or baryons: qqq or $\bar{q}\bar{q}\bar{q}$).

In high energy interactions, therefore no free quarks exit the scattering process, but the partons fragment (split and recombine with other partons) into several colour neutral hadrons, which are measurable in the detectors as bundles of particles clustered together into so-called *jets*.

4.2.1   Renormalisation
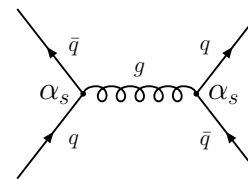
Figure 4.1: Leading order diagram to quark scattering in QCD.

In pQCD the calculation of the amplitude for the transition from initial to final state is expressed as power series expansions in the coupling constant α_s. If the expansion series converges, the series can be truncated at an appropriate order and the following orders can be neglected. The resulting calculation of an interaction is characterised by the order after which the expansion was stopped.

Figure 4.1 shows a Leading Order (LO, i.e. lowest order in α_s) diagram for quark-antiquark scattering. If contributions beyond the LO are considered, two types of singularities can appear when integrating over the phase space. The so-called *ultraviolet divergencies* (UV) are produced by loops, as the one shown in Figure 4.2a. Loops with infinite loop momenta lead to virtual fluctuations on very short time scales/distances. Additionally, *infrared* (IR) or *collinear* divergencies are related to long-time/distance physics. The infrared divergencies occur in loop contributions as well as through the emission of soft (low momentum) gluons, and the collinear ones when very collinear gluons are emitted in the initial or final state parton direction (Figure 4.2b).

Both singularities can be systematically removed, through a *dimensional regu-*
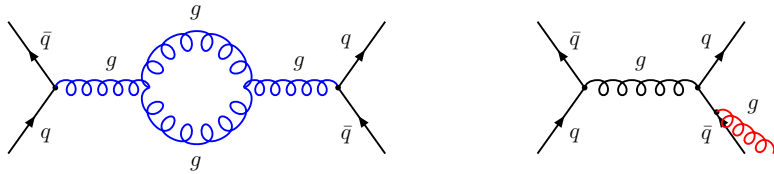
Figure 4.2: Examples of divergencies present at NLO: Quark loop producing an UV divergence (left). Emission of a collinear gluon (right).

larisation method, by first changing the space-time integration dimension from 4 to $4 - \epsilon$ ($\int d^4 \to \lim_{\epsilon \to 0} \int d^{4-\epsilon}$), and in a second step using a *renormalisation scheme* to reparametrise the amplitudes in terms of physical observables.

In the renormalisation process, the divergencies can be consistently absorbed by the parameters in the QCD Lagrangian: the coupling constants, masses and field strengths. A particular renormalisation scheme must be chosen, and here a *renormalisation scale* μ is introduced. A consistent choice of the renormalisation scale is typically the energy scale of the physics process. For heavy quark production (Section 4.4), a common choice is $\mu^2 = m_Q^2 + p_T^2$, where m_Q is the mass and p_T^2 is the transverse momentum of the heavy quark. It should be noted that although μ has dimension of mass, it is only introduced as an intermediate parameter to make the perturbative calculation possible. It is neither a cut off, nor a physical parameter.

The strong coupling constant depends on the renormalisation scale. The requirement that a measurable cross section $d\sigma$ has to be independent of the chosen renormalisation (or factorisation, see below) scale leads to an effective coupling constant α_s which can be obtained from the renormalisation group equation:

$$\mu^2 \frac{\partial \alpha_s(\mu)}{\partial \mu^2} = \beta(\alpha_s(\mu)), \tag{4.4}$$

where the β function can be written as a perturbative expansion in α_s, in terms of the renormalisation scale. The LO solution ($\mathcal{O}(\alpha_s)$) of Equation 4.4 is:

$$\alpha_s(\mu) = \frac{12\pi}{(33 - 2n_f)\ln(\mu^2/\Lambda_{\mathrm{QCD}}^2)}, \tag{4.5}$$

where Λ_{QCD}^2 is a fundamental parameter of QCD, which is determined experimentally, and n_f is the number of active quark flavours below that scale. Knowing the value of α_s at a certain scale, the values of α_s can be calculated perturbatively at all scales.

Figure 4.3 shows the dependence of the coupling constant on the energy scale. It can be clearly seen that for low energies perturbative calculations are not possible

as the strong coupling becomes large. In contrast, in the high energy domain the strong coupling becomes small and pQCD calculations can be accurately made.
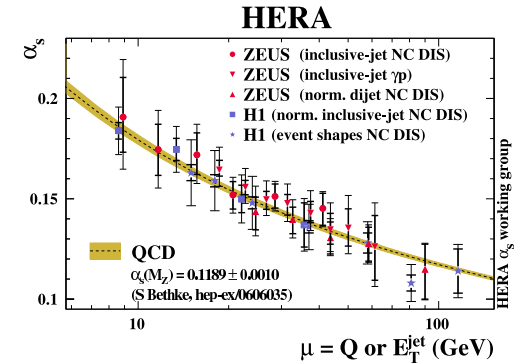
Figure 4.3: Summary of measurements of α_s at HERA as a function of the energy scale μ. The band is the QCD prediction for the value of $\alpha_s(M_Z)$.

4.3 Lepton-Proton scattering at HERA

Figure 4.4: Diagram of the ep scattering process at HERA.
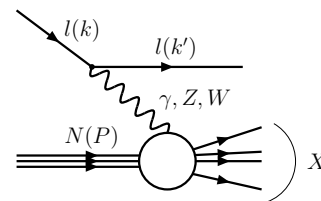
The interaction between a proton and a lepton –electron or positron– proceeds via the exchange of a virtual boson as depicted in Figure 4.4. The lepton number has to be conserved, therefore the presence of a scattered lepton in the final state is required, while the nucleon N fragments into a hadronic final state X.

$$lN \to l'X \tag{4.6}$$

For Neutral Current (NC) processes, in which the final state lepton is an electron or positron, the vector boson can be a γ or a Z, and for charged current (CC) interactions, the final state lepton is a neutrino and the exchanged vector boson is a W.

Assuming that k, k', P, P' are the four-vectors of the initial and final leptons, of the incoming nucleon and of the outgoing hadronic system, respectively, the set of

Lorentz invariant variables that describe the unpolarised lepton-proton scattering are: The transfered momentum squared or boson virtuality, which is given by

$$Q^2 = -q^2 = -(k - k')^2, \tag{4.7}$$

the centre of mass energy squared

$$s = (k + P)^2, \tag{4.8}$$

the centre of mass energy of the photon-proton system

$$W^2 = (q + P)^2, \tag{4.9}$$

the so called inelasticity,

$$y = \frac{P_p \cdot q}{P_p \cdot k} \qquad 0 < y < 1, \tag{4.10}$$

and a dimensionless variable introduced by Bjorken

$$x = \frac{Q^2}{2 P_p \cdot q} \qquad 0 < x < 1. \tag{4.11}$$

The kinematic variables given above are not independent. Once the centre-of-mass energy $\sqrt{s}$ is given, the kinematics of the event is completely determined by the knowledge of two of the other variables. Usually from the energy and direction of the outgoing lepton the (x, y) or (x, Q^2) pairs of variables can be determined.

The variable Q^2 defines two kinematic regimes, the Deep Inelastic scattering (DIS) and the Photoproduction (PHP) regime. Events with high photon virtuality ($Q^2 \geq 1\,\text{GeV}^2$) and large hadronic centre of mass energy ($W^2 = (q + P)^2 > m_p^2$) are referred to as DIS events. For these events the incoming lepton is deflected by some measurable angle and can be identified in the detector. Whereas for those events where the exchanged photon is almost real ($Q^2 < 1\,\text{GeV}^2$), the incoming lepton is deflected at a very small angle and can not be observed in the detector (PHP regime).

In the DIS regime and for $E_p \gg m_p$ (infinite momentum frame), the ep scattering can be described as the incoherent sum of elastic scattering processes of the lepton on a set of (non-interacting) partons which are interpreted as quarks and gluons. This picture is called the quark parton model (QPM) [26, 27]. In this picture, the variable x can be interpreted as the fraction of the parton momentum carried by the struck (massless) quark. The quarks that have not been struck are not influenced by the photon-quark scatter and are called $s$pectator quarks. The inelasticity y can be interpreted as the fraction of the lepton energy transfered to the hadronic system in the proton rest frame.

4.3.1 Factorisation

A high energy ep collision process can be roughly described as a sequence of distinct steps. The exact separation between the different parts is not unambiguous. However a separation between perturbative and non-perturbative parts of the calculation can be made. The *factorisation* theorem [28] allows to distinguish short-distance effects, which can be calculated perturbatively, and long-distance effects which need to be modeled by other means. As for renormalisation, a specific factorisation scheme must be chosen to consistently separate both effects, the only constraint is the presence of a hard scale, which can be for example the Q^2 of the event, the transverse momentum of the outgoing partons or, in the case of heavy flavour production, the mass of the heavy quarks.

In separating the perturbative and non-perturbative parts, the factorisation scale μ_F is introduced. Roughly speaking, any propagator that is off-shell by μ_F^2 or more will contribute to the hard scatter part of the calculation ($\hat{\sigma}_i$). Below this scale, it will be included in the non-perturbative proton distribution functions $f_i^p(x, \mu_0^2)$, where μ_0 is the starting scale and the subscript i denotes the parton type. The parton distribution functions at a starting scale have to be determined experimentally. They can be evolved to any other scale $\mu_F > \mu_0$ using parton evolution schemes, as will be described below. The factorisation of the ep scattering process, as described above, is illustrated in Figure 4.5.
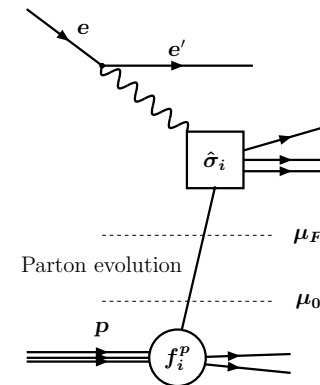
Figure 4.5: Schematic representation of the QCD factorisation theorem for ep scattering process. Here $\hat{\sigma}_i$ is the perturbative hard scattering process, f_i^p are the non-perturbative parton distribution functions of the proton, which can be evolved from the initial scale μ_0 to the factorisation scale μ_F.

Applying the factorisation theorem the ep cross section can be decomposed as follows:

$$d\sigma(ep \rightarrow eX) = \sum_i \int_0^1 f_i^p(x, \mu_f^2) \cdot d\hat{\sigma}_i(\hat{s}, \alpha_s(\mu_R^2), \mu_R, \mu_F) \, dx \qquad (4.12)$$

The parton distribution functions $f_i^p(x, \mu_f^2)$ of the proton are universal. The cross section for the hard process $\hat{\sigma}_i$ depends on the centre-of-mass energy $\hat{s}$, the factorisation scale μ_F, the strong coupling constant α_s and the renormalisation scale $\mu_R \gg \Lambda_{QCD} \approx 200 \, \text{MeV}$.

4.3.2 QCD Evolution Equations

In a hard ep-collision, the factorisation theorem states that all non-perturbative effects can be factorised into universal (process-independent) parton densities. This leads to a perturbatively calculable dependence on Q^2 (the hard scattering scale of the interaction), called *parton evolution*. The essential idea is that the parton being probed may not come directly from the proton, and instead the original quark or gluon may radiate another parton before interacting with the photon.

The formalism of *collinear factorisation* is the one in which the DGLAP evolution equations [29] are used to describe the radiation of partons from the initial parton distribution in the proton and in the photon. In the collinear factorisation ansatz the parton distributions in the proton (or photon) are assumed to depend only on the scale variable x and an energy scale μ, usually the photon virtuality Q^2. In particular, the initial partons in the proton are assumed to carry no transverse momentum. In the evolution the partons are treated as massless on-shell particles. Factorisation and renormalisation scales are used to absorb the divergent parts of the perturbation series into the parton distributions and α_s.

In other approaches, such as the BFKL evolution equations [30–32] and later the CCFM evolution equations [33–35], the so-called k_T *factorisation* formalism is used. In this approach there is no restriction on the momentum k_T of the partons but in contrast it has a strong ordering in x, as will be described in Section 4.5.1.

4.4 Heavy flavour production at HERA

A quark is defined to be heavy when its mass m_Q is much larger than Λ_{QCD}. Hence *charm, beauty* and *top* are referred to as *heavy quarks*. Due to its high mass the top quark is outside the scope of HERA.

Heavy flavour physics has traditionally been a challenging testing ground for the predictions of perturbative QCD. Commonly it is said that the mass of the heavy quark sets the hard scale of the production process, although it is more accurate to say that the condition $m_Q \gg \Lambda_{QCD}$ indicates that perturbative predictions are only marginally affected by power corrections and by contributions from non-perturbative origin.

At HERA heavy quarks are produced predominantly in the boson-gluon fusion process (BGF) which is pictured in Figure 4.6.
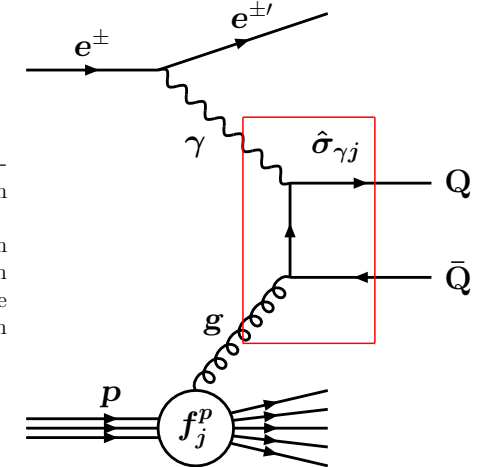
Figure 4.6: Heavy quarks produced in a boson-gluon fusion process in ep-scattering. The matrix elements $\hat{\sigma}_{\gamma j}$ can be computed perturbatively, in contrast to the non-perturbative part: the parton distribution functions of the proton f_j^p.

At present, the theoretical calculations for such processes use the factorisation theorem to make a convolution of pQCD matrix elements and non-perturbative components, obtaining cross section predictions which can be compared with experimental data. For the heavy flavour production case the factorisation and renormalisation scales are usually chosen to be equal, $\mu_F = \mu_R$.

In this approach, the cross section for the production of an inclusive open heavy

quark Q in photon-hadron collisions can be written as [36]:

$$d\sigma_Q = \sum_j f_j^p \otimes d\hat{\sigma}_{\gamma j} + \sum_{ij} f_i^\gamma \otimes f_j^p \otimes d\hat{\sigma}_{ij}, \qquad (4.13)$$

where f_i^γ and f_j^p are the parton densities in the photon and in the proton respectively; $\hat{\sigma}_{\gamma j}$ and $\hat{\sigma}_{ij}$ are the perturbative hard scattering processes.

The hard process $\hat{\sigma}_{\gamma j}$, for example, is expressed as power series in $\alpha_{em}\alpha_s^i$:

$$\hat{\sigma}_{\gamma j} = \sum_{i=1}^\infty \alpha_{em}\alpha_s^i A_i = \alpha_{em}\alpha_s A_1 + \alpha_{em}\alpha_s^2 A_2 + \alpha_{em}\alpha_s^3 A_3 + \ldots \qquad (4.14)$$

The coefficients A_1, A_2, and A_3 indicated in Equation 4.14 correspond to the LO, NLO, and NNLO contributions respectively. These predictions for the production of heavy quarks are also called: *parton level* predictions.

If cross-section predictions beyond the parton level are wanted (for example, predictions on quantities that can be directly measured in the detectors) the order at which the matrix elements $\hat{\sigma}$ are calculated strongly influence the further evolution of the heavy quarks in the theoretical models. This is because some of the higher order contributions to Equation 4.14 could be double counted, as will be explained in Chapter 5. On the following the order at which the different contributions are calculated will be explicitly stated.

The discussion now will focus on the different methods to calculate the two contributions to the parton level cross section $d\sigma_Q$, Equation 4.13, considering the special conditions that apply to HERA.

4.4.1   Parton distribution functions

In heavy flavour processes, the parton distribution functions (PDF) provide important information on the initial phase of the interaction. They are specific to the incoming proton, and could be described as the momentum distributions of partons inside the proton (corresponding to f_j^p in Equation 4.13).

The calculation of parton distributions within the incoming hadron is not possible using perturbative methods, since the interactions inside the proton are dominated by low momentum transfer processes, leading to the absence of a hard scale which can be used in the perturbation expansion. Instead, they are determined e.g. by global fits to deep inelastic scattering data. Figure 4.7 shows parton density functions for u, d and s quarks and gluons as extracted from an NLO QCD analysis on DIS data by the ZEUS and H1 collaborations [37] at $Q^2 = 10\,\text{GeV}^2$.
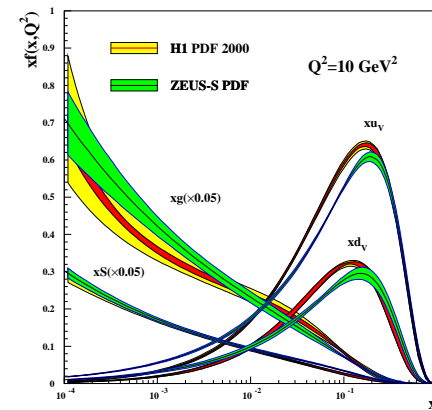
Figure 4.7: Set of quark and gluon distribution functions extracted from fits to deep inelastic data, when probed at a momentum scale $\mu^2 = 10\,\text{GeV}^2$.

The evolution of the parton densities as a function of Q^2 can be calculated using the parton evolution schemes described in 4.3.2.

The factorisation theorem ensures that the PDFs are universal and therefore the distributions obtained in other experiments or in fits to other data can be applied to any process. The CTEQ [38] group, among others, also provides PDFs updated to recent data and theoretical developments.

The PDFs available are obtained using a specific renormalisation and factorisation scheme. Therefore, in heavy flavour production, to correctly match the matrix elements with the PDFs, it is important to select the same scheme for both contributions.

4.4.2   Photon structure

The next ingredient in the calculation of the heavy flavour production cross section is the photon structure, f_i^γ in Equation 4.13. In deep inelastic scattering the finite photon virtuality ensures that the interaction process takes place on a short time scale, and the photon acts like a point-like exchange boson (Figure 4.8a). In contrast, towards smaller photon virtualities, the photon becomes quasi-real. In photoproduction it can show hadronic behaviour, fluctuating into a system of light quarks and gluons with one of these participating in the interaction, as shown in Figure 4.8b.
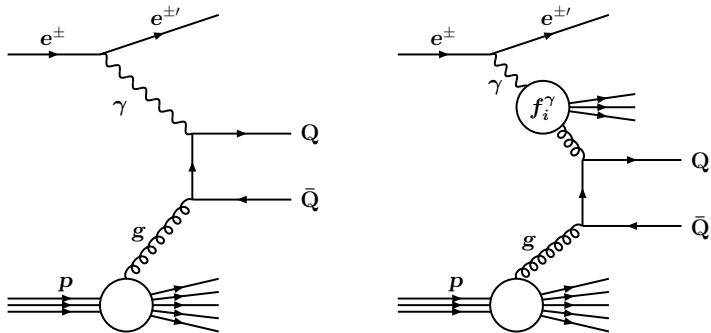
Figure 4.8: Photon as a point-like exchange boson (left) and a quasi real photon showing hadronic structure (right). Here f_i^γ is the photon structure function.

Like for protons, the photon structure can be described by a parton distribution function. Such distributions for the photon have been extracted from measurements e.g. in $\gamma\gamma^*$ collisions at LEP [39].

The photon structure functions depend both on the approach in which the parton evolution is described (DGLAP, CCFM or BFKL) and on the order of the perturbative expansion. Using the "massive scheme" (see next section) at NLO in the DGLAP approach most of the photon structure is included in the hard matrix elements and the contributions from processes with hadron-like photons becomes small ($\lesssim 10\%$).

4.4.3 Perturbative calculation of matrix elements

For the calculation of the matrix elements of the hard processes $\hat{\sigma}_{\gamma j}$ and $\hat{\sigma}_{ij}$ of Equation 4.13 different schemes have been developed, which differ mainly in the order at which the perturbative series is truncated (LO, NLO etc), or in the choice of the scale parameters ($\mu^2 = m_Q^2, Q^2, p_T^2$):

- **Massless Resummed Scheme**
  In this approach, also known as the Zero Mass Variable Flavour Number Scheme (ZM-VFNS) [40, 41], quarks are treated as active partons in the proton. For that, a density distribution for the quarks in the proton is used to describe the non-perturbative part of the calculation. The perturbative series is expanded using the scale parameter μ, given by the hard scales of this scheme: Q^2 or the jet momentum p_T. The perturbative calculations are expected to converge for $\Lambda_{QCD} < \mu$ if the divergent logarithm terms, like $[\alpha_s \ln(\mu^2/m_q^2)]^n$, are properly controlled by resummation techniques (See for example [24]).

This approach is valid for heavy quarks in the limit when $\mu^2 \gg m_Q^2$, in which the heavy quarks can be treated as massless.

In the massless scheme at LO the dominant contribution is the heavy quark excitation (Figure 4.9a). At NLO virtual corrections, like the one shown in Figure 4.9b are included, and the QCD Compton (Figure 4.9c) and photon-gluon fusion ($\gamma g \to q\bar{q}$, Figure 4.6) processes also contribute.
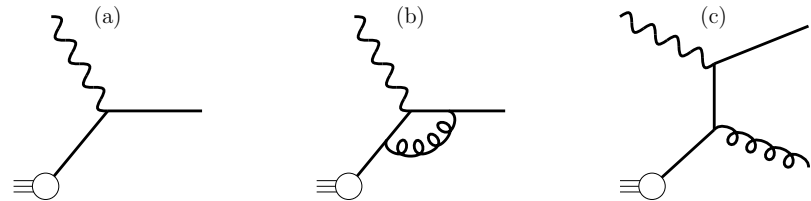
Figure 4.9: LO (a) and some NLO (b,c) diagrams for heavy flavour production in the massless scheme.

- **Massive Fixed Order Scheme**
  At values of $\mu^2 \sim m_Q^2$, the massive scheme is more appropriate. This approach is often refered to as the Fixed Flavour Number Scheme (FFNS) [42–44]. In this scheme, the heavy quarks are dynamically produced in the hard interaction and the scale to make the perturbative expansion is the mass of the heavy quark m_Q. In this approach the logarithmic terms, which needed to be resummed in the massless approach, are neglected.
  In the massive scheme the LO process is the boson-gluon fusion process and NLO contributions, like the ones shown in Figure 4.10, are of order α_s^2.
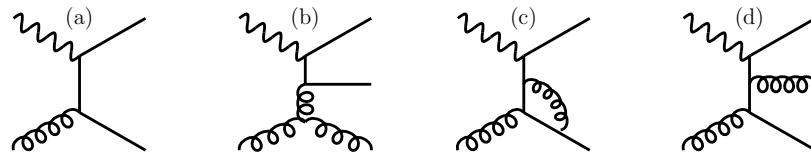
Figure 4.10: LO (a) and NLO (b-d) contributions to the heavy flavour process in the massive scheme.

The fixed order massive scheme is used in this thesis to create a Monte Carlo event generator which implements the NLO calculations, fragmentation and decay of the heavy quarks to give predictions for complex final states, as will be described in Chapter 6.

- **General Mass Variable Flavour Number Scheme**
  To provide reliable pQCD predictions over the whole range of μ^2, composite schemes have been created, which provide a smooth transition from the massive description $\mu^2 \sim m_Q^2$ to the massless behaviour $\mu^2 \gg m_Q^2$. These are commonly referred to as General Mass Variable Flavour Number Schemes (GM-VFNS) [45–51], in which the heavy quark becomes active inside the proton depending on the energy scale.

4.5 Heavy flavour evolution at HERA

The concern of the last section was the production of heavy quarks. This section will be engaged with its evolution, i.e. after the creation of the heavy quark, the different steps that it goes through until indication of its presence is observed in the detector.

As for the production case, the evolution of heavy quarks can be described as a series of different steps. For example, in a first perturbative step, additional partons can be emitted from an initial state parton or from the heavy quark (*parton shower*), followed by a second non-perturbative step using phenomenological models to form hadrons from these partons (*hadronisation*), and finally the last step is the decay of those hadrons into particles which may (or not, e.g. neutrinos) be registered in the detector.

This description depends strongly on three facts of the production phase: First, the scheme (massless, massive, general) used to calculate the matrix elements of the hard interaction, second the order of the perturbative expansion in the calculation of those matrix elements and third the evolution scheme of the initial state radiation. This dependence is better understood looking at Figure 4.11. There, when the matrix elements of the hard interaction are calculated at LO, the first step of the heavy flavour evolution is the *parton shower* (PS), in which additional partons are emitted from the initial state parton, as will be explained in detail below. On the contrary, when NLO contributions to the hard scattering process are used, parts of the parton shower are already included in the calculation. Therefore it is important to keep in mind that the description of the evolution of heavy flavours used in the context of LO + PS may not be applicable in the context of NLO calculations. Each step in the heavy flavour evolution will be discussed next.

4.5.1 Parton showers

The model of parton showers, or *parton cascades*, approximates multiple parton emissions by a series of successive parton splittings, as illustrated in Figure 4.12. The probability that a parton is emitted from a parent parton with a given virtuality
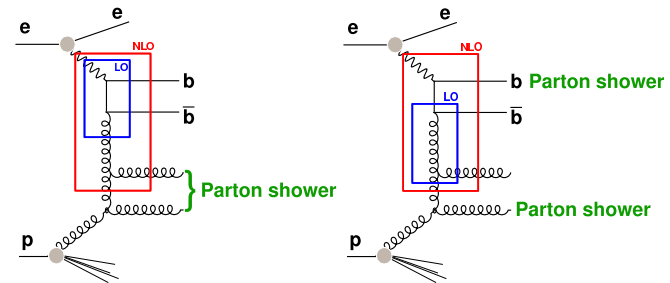
Figure 4.11: LO, NLO and PS in $b\bar{b}$ production. A part of the parton shower applied to the initial and final state partons in LO is part of the hard scatter at NLO. From [52]

is taken from the corresponding *splitting functions* [29], which are also part of the evolution equations.

Initial- and final-state parton showers are treated differently. The initial state parton shower starts from a parton coming from the proton which continues to emit partons with increasing virtuality until it enters the hard scatter. In contrast, outgoing partons from the heavy quarks have positive virtuality and the emissions are stopped when they reach a minimal virtuality, typically $\sim 1\,\text{GeV}$. The initial-state parton showers are closely connected with the evolution of parton density functions (PDFs). But while the evolution of PDFs typically starts with some parametrised input distribution at some low scale and applies a given evolution scheme to obtain the distribution at higher scales, the initial-state parton shower is typically constructed the other way around. After a sub-process has been generated at some high scale, the incoming partons are evolved backwards down to lower scales, explicitly constructing the necessary splittings. Several evolution schemes have been developed, the most commonly used at HERA will be described next:

- **The DGLAP equations**
  The Dokshitzer-Gribov-Lipatov-Altarelli-Parisi (DGLAP) evolution equations, describe the way in which the quark and gluon momentum distributions inside a hadron evolve in Q^2. The DGLAP equations are given by:

$$\frac{\mathrm{d}q_i(x,Q^2)}{\mathrm{d}\log Q^2} = \frac{\alpha_s(Q^2)}{2\pi} \int_x^1 \frac{\mathrm{d}y}{y} \left[\sum_i q_i(y,Q^2)P_{qq}\left(\frac{x}{y}\right) + g(y,Q^2)P_{qg}\left(\frac{x}{y}\right) \right] \quad (4.15)$$

$$\frac{\mathrm{d}g(x,Q^2)}{\mathrm{d}\log Q^2} = \frac{\alpha_s(Q^2)}{2\pi} \int_x^1 \frac{\mathrm{d}y}{y} \left[\sum_i q_i(y,Q^2)P_{gq}\left(\frac{x}{y}\right) + g(y,Q^2)P_{gg}\left(\frac{x}{y}\right) \right] \quad (4.16)$$

where $q_i(x,Q^2)$ is the quark density function for each quark flavour i, and

$g(x, Q^2)$ is the gluon density function. The Altarelli-Parisi splitting functions $P_{jk}\left(\frac{x}{y}\right)$ represent the probability of a parton k with momentum fraction y emitting a parton j of momentum fraction x in the interval $Q^2 \to Q^2 + \mathrm{d}\log Q^2$. In the DGLAP formalism a collinear evolution of PDFs is applied, in which all collinear singularities from the initial state radiation are absorbed into the PDFs, while in parton showering the evolution is non-collinear.

The DGLAP approach assumes that the dominant contribution to the evolution comes from successive parton emissions which are strongly ordered in transverse momentum k_T, the largest of which corresponds to the parton interacting with the probe ($k_{T,1}^2 \ll k_{T,2}^2 \ll \ldots \ll k_{T,n}^2 \ll Q^2$), as illustrated in Figure 4.12.
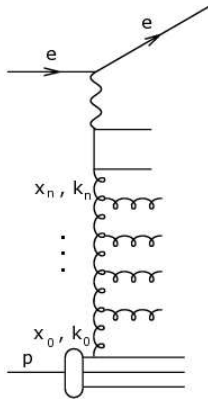
Figure 4.12: Diagram of the k_T evolution ladder. A quark from the proton interacts with a virtual photon from the electron after radiating n gluons. Each gluon is characterised by a longitudinal momentum fraction x_i and a transverse momentum $k_{T,i}$.

- **The BFKL equations**
  The Balitsky-Fadin-Kiraev-Lipatov (BFKL) approach, also called k_T factorisation, corresponds roughly to emissions strongly ordered in x, with no restriction on the momentum k_T, since partons in the initial state cascade can have any kinematically allowed transverse momentum, in contrast to DGLAP.

- **The CCFM equations**
  The Ciafaloni-Catani-Fiorani-Marchesini approach attempt to cover both the DGLAP and BFKL regions by considering colour coherence effects. In the CCFM evolution equation angular ordering of emissions is introduced to correctly treat gluon coherence effects.

4.5.2 Hadronisation

The heavy quarks produced in the hard interaction can not be observed directly in the experiment due to colour confinement. They form colour neutral bound states (hadrons) which are formed from the original quark pair. The process in which the hadron formation takes place is called *hadronisation* or *quark fragmentation*. The hadronisation of the heavy quark into a heavy-flavoured hadron is described by the factorisation theorem through the following equation [36]:

$$\frac{d^3\sigma_H(k)}{d^3k} = \int D(z) \frac{d^3\sigma_Q(\hat{k})}{d^3\hat{k}} \, \delta^3(\vec{k} - z\vec{\hat{k}}) \, d^3\hat{k} \, dz, \qquad (4.17)$$

where H is the heavy-flavoured hadron with momentum k, and $\hat{k}$ is the momentum of the heavy quark. $D(z)$ is the non-perturbative fragmentation function, which is not calculable but universal, and z is the momentum fraction of the parton carried by the hadron.

- **Fragmentation functions**
  These describe the fraction of the quark's energy transferred to the final state hadron. Among the most popular parametrisations are:

  ▷ *Lund String Model* [53]
    In this model $q\bar{q}$ pairs are connected by colour field lines, called *strings*. The potential is assumed to rise with the distance r between the quarks. When the energy stored is sufficient, the string breaks producing a new $q\bar{q}$ pair. The string breaks up repeatedly into colour singlet systems as long as the invariant mass of the string pieces exceeds the on-shell mass of a hadron. The $q\bar{q}$ pairs are created according to the probability of a tunnelling process $\exp\left(-\pi m_{q,\perp}^2/\kappa\right)$ which depends on the transverse mass squared $m_{q,\perp}^2 \equiv m_q^2 + p_{q,\perp}^2$ and the string tension $\kappa \approx 1\,\mathrm{GeV/fm}$. Due to the dependence on the parton mass m_q and/or hadron mass m_h, the production of heavy-quark hadrons is suppressed. The string fragmentation function for light quarks has the form:

$$D(z) \sim \frac{1}{z}\,(1-z)^a \, \exp\left(-\frac{bm_h^2}{z}\right), \qquad (4.18)$$

  where a and b are free parameters which need to be adjusted to bring the fragmentation into accordance with measured data.

It was recognised very early [54] that a heavy flavoured meson should retain a large fraction of the momentum of the primordial heavy quark, and therefore its fragmentation function should be much harder than that of a light hadron. In the limit of a very heavy quark, one expects the fragmentation function to go into any heavy hadron to peak near 1.

When the heavy quark is produced at a momentum much larger than its mass, one expects important perturbative effects, enhanced by powers of the logarithm of the transverse momentum over the heavy quark mass, to intervene and modify the shape of the fragmentation function. Some of the parametrisations used for heavy flavours are the following:

▷ *Peterson fragmentation function* [55] which has the form:

$$D(z) \propto \frac{1}{z} \left(1 - \frac{1}{z} - \frac{\epsilon}{1-z}\right)^{-2}, \tag{4.19}$$

where ϵ is a free parameter which depends on the order of the perturbative expansion and is expected to scale with the quark mass: $\epsilon \propto 1/m_{\rm Q}^2$.

▷ *Kartvelishvili parametrisation* [56]:

$$D(z) \propto z^{\alpha} (1-z), \tag{4.20}$$

here α is the variable parameter.

At this stage hadrons were formed from the original heavy quarks. A list of the most frequently produced B- and C-hadrons is given in Table 4.3.

Hadron	quark content	mass [MeV]	life time [ps]
$B^{\pm}$	bu	5279.0 ± 0.5	1.643 ± 0.010
B^0	bd	5279.4 ± 0.5	1.527 ± 0.008
B_s^0	bs	5369.6 ± 2.4	1.454 ± 0.040
Λ_b	udb	5624.0 ± 9	1.288 ± 0.065
$D^{\pm}$	cd	1869.4 ± 0.5	1.051 ± 0.013
D^0	cu	1864.6 ± 0.5	0.411 ± 0.003
$D_s^{\pm}$	cs	1968.3 ± 0.5	0.490 ± 0.009
Λ_c^+	cud	2284.9 ± 0.6	0.200 ± 0.006

Table 4.3: Examples of B- and C- hadrons.

As seen in Table 4.3, B hadrons have both a higher mass and a longer life time than C hadrons. The higher mass is due to the higher b-quark mass. The longer life time results from the smaller transition probability $b \rightarrow c$ as compared to $c \rightarrow s$ in the Cabibbo-Kobayashi-Maskawa (CKM) matrix elements $|V_{cb}| \sim 0.04$ and $|V_{cb}| \sim 0.97$ respectively (See e.g. [2]). More properties of such heavy-flavoured hadrons can be found elsewhere [2, 12].

4.5.3 Decay of heavy-flavoured hadrons

The presence of hadrons containing heavy quarks is deduced by observation of their decays. There are several modes for a hadron to decay, but since leptons are particles which are relatively easy to identify in the detectors, the decay of hadrons into leptons will be investigated in the last part of this thesis in order to tag events where beauty quarks are present. The discussion will now begin with the semileptonic decay of a heavy hadron.

- **Semileptonic decay**
  The simplest approach is to treat the semileptonic decay of hadrons containing c or b quarks in analogy with the decay of a free muon. This is also called *spectator model*, since the light quarks $\bar{q}$ accompanying the heavy quark Q in the hadron are assumed to play no role in the decay. Diagrams for spectator model decay of B and C mesons is shown in Figure 4.13.
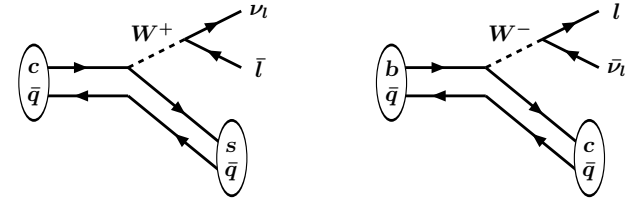
Figure 4.13: Spectator diagrams for C and B meson decays.

The leptons (e and μ) resulting from the semileptonic decay provide a very clear experimental signature among the possible final states of hadron decays.

- **Cascade decay**
  Additionally to the direct lepton production, the so called *cascade decays* provides another source of leptons from beauty decays, as shown in Figure 4.14. As will be explained later in this work, the requirement of two leptons (e and/or μ) in the final state provides a clear experimental signature of the presence of beauty quarks (Chapter 7).
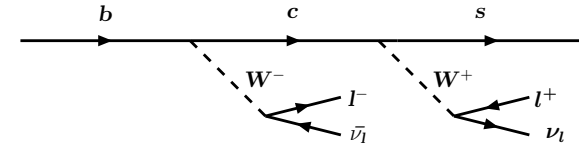
Figure 4.14: Weak cascade decay of a beauty quark.

Some examples of branching ratios of direct and cascade decays of beauty are given below.

decay	branching fraction [%]
$b \to e^+ \nu_e$	10.9
$b \to \mu^+ \nu_\mu$	11.0
$b \to \tau^+ \nu_\tau$	2.5
$b \to \text{cascade} \to e$	9.6
$b \to \text{cascade} \to \mu$	10.03
$b \to \bar{D}^0 X$	60.9
$b \to D^- X$	23.5
$b \to D^{*+} X$	17.3

Table 4.4: Beauty quark branching ratios in percentage.

4.6 Heavy flavour Monte Carlo models and NLO predictions

In this section a short review of the different Monte Carlo models and NLO predictions to describe the production and evolution of heavy quarks at HERA will be made. The methods described in this section are used to compare QCD predictions with HERA data (See Chapter 5). This part is also intended as a motivation to introduce in Chapter 6 a new method, the FMNR⊗PYTHIA interface, which is designed to provide heavy flavour NLO predictions at visible level.

At HERA, as in any other high energy collider, event generator programs are used to modelate the physics processes [57]. They provide samples of single events with their full set of initial state, intermediate and final state particles which follow distributions as predicted by the underlying QCD calculation. The production and evolution of beauty quarks, as explained in Sections 4.4 and 4.5, can be modeled by series of perturbative and non-perturbative methods. This is illustrated in Figure 4.15.

The different models and predictions for heavy flavour processes differentiate each other in two main characteristics: the order of the perturbation expansion: LO, NLO, NNLO, etc; and in the 'level' of the prediction: parton- hadron- or visible level. Predictions at *parton level* are those calculations up to the creation of the heavy quark; predictions at *hadron level* give information over the hadrons produced after the fragmentation of the heavy quark and predictions at *visible level* are the calculations up to quantities which can be registered in the detector.
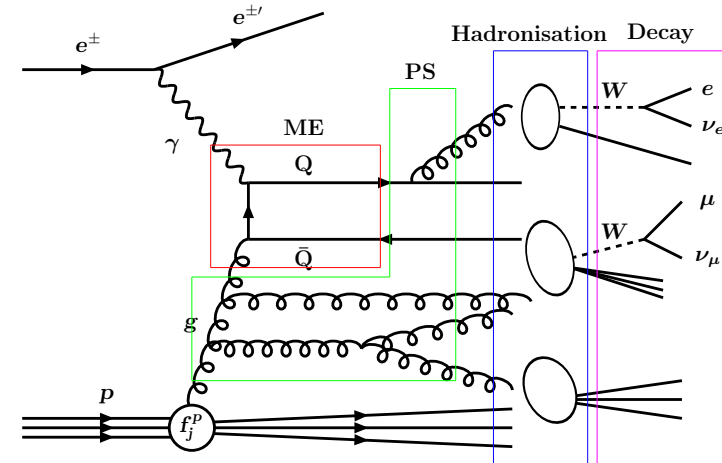
Figure 4.15: Heavy flavour production and evolution as modeled in *ep* event generators in a boson-gluon fusion process. Series of perturbative and non-perturbative steps are used to obtain cross section predictions.

The event generators may not make use of all the steps shown in Figure 4.15, as will be explained below in the description of some of the most used models at HERA.

4.6.1 Leading order + parton shower calculations

Leading order plus parton shower event generators make use of Monte Carlo techniques. In them the matrix elements (ME in Figure 4.15) are evaluated at leading order and effects from higher orders are introduced using parton showers (PS) which are radiated from the initial and final state partons using a soft collinear approximation. Monte Carlo generators of this kind are generally known as LO+PS, to indicate the combination of leading order matrix elements with parton showers.

The Monte Carlo programs used for the modeling of heavy quark physics at HERA are: PYTHIA [58], RAPGAP [59], AROMA [60] and HERWIG [61]. These programs are based on the DGLAP evolution equations (Section 4.4.1). More recently, the Monte Carlo program CASCADE [62] was introduced which contains an implementation of the k_t factorisation approach using the CCFM evolution equation. For this thesis the more relevant LO+PS programs are: PYTHIA which is used in Chapter 6 for the implementation of a new method to calculate NLO predictions; RAPGAP which

together with PYTHIA is used as Monte Carlo for acceptance corrections in heavy flavour analyses; and finally HERWIG which may be used in the future to obtain NLO predictions using a different method to the one proposed in Chapter 6 of this work.

In these Monte Carlo programs the formation of hadrons (See Figure 4.15) is simulated using the Lund string model (as implemented in JETSET [63]) complemented by the Peterson fragmentation function for heavy quarks. In HERWIG a cluster algorithm is used to form hadrons. After the hadronisation, the decay of the unstable hadrons is applied according to decay probabilities and spectra determined from measurements from other experiments. The final state particles are subsequently filtered through a detailed detector simulation (ZEUS uses e.g. Mozart, based on GEANT[64]) to describe the detector response. After these steps, the generated events can be compared to experimental data.

A short description of the Monte Carlo programs follows:

- The PYTHIA Monte Carlo generator is used in the massive scheme, in which the heavy quarks are generated dynamically, using the boson-gluon fusion process. PYTHIA can also be used in an inclusive mode in which direct and resolved events are generated using massless matrix elements for all quark flavours.

- The RAPGAP Monte Carlo generator produces events using the massive approach. It also provides a correct treatment of the diffractive contribution of inclusive scattering which was not included in older generators.

- HERWIG includes the simulation of hard lepton-lepton, lepton-hadron and hadron-hadron scattering and soft hadron-hadron collisions. HERWIG implements the cluster hadronisation approach to describe the fragmentation of quarks into hadrons via non-perturbative gluon splitting. The coloured objects in the final state are combined to colour-singlet clusters which are subsequently fragmented into hadrons.

4.6.2 Next-to-leading order calculations

Other event generators for heavy-flavour processes at HERA evaluate the matrix elements (ME of Figure 4.15) including next-to-leading order corrections. These predictions are considered to provide more reliable estimates of the cross sections, as they account for the presence of hard parton emissions and virtual corrections, as the ones shown in Figure 4.10.

In the NLO calculations, the different matrix element diagrams contributing to the cross section are implemented as sets of processes with positive or negative weights. Processes with positive weights are for example $\gamma g \to Q\bar{Q}g$. Processes

with negative weights are for example some cases where virtual corrections producing divergencies are present (more about this in Chapter 6). The big spread of weights make it difficult to implement NLO calculations in full hadron level Monte Carlo event generators. Thus, most of the next-to-leading order predictions are available only at parton level. The need of next-to-leading order predictions at visible level to compare with HERA data is one of the main motivations of this thesis work and this topic is extensively treated in Chapter 6. For that so called Fixed Order parton level calculations are used. The ones commonly used at HERA are described next.

Fixed order parton level calculations

NLO predictions at parton level are implemented for ep and γp processes in the programs FMNR and HVQDIS. Both programs are based on calculations in the massive scheme (Section 4.4.3) and provide weighted parton level events with two or three outgoing partons, i.e. a quark, an antiquark and an additional light parton.

- The FMNR [65–67] program implements cross section calculations for the photoproduction regime, in both leading and next-to-leading order. An extensive description of the FMNR program will be given in Chapter 6.

- HVQDIS [68–70] covers the DIS region of Q^2. The NLO matrix elements are calculated in the 3-flavour approach, this limits the choice of input parton densities to strictly 3 flavour models (in the $\overline{MS}$ factorisation scheme).

Calculation of visible level cross sections can be obtained from these programs using extensions, which include the fragmentation (and optionally, decay) of the heavy quarks. Usually, the heavy quarks are hadronised by rescaling the three momentum of the quark according to the Peterson fragmentation function.

For comparison with experimental measurements, which typically are given at visible level, the parton-level calculations have to be corrected. These corrections should be in principle at NLO, as the parton-level calculations. However, at HERA for lack of more appropriate simulations the LO+PS generators described above are commonly used. In $p\bar{p}$ collisions (LHC and Tevatron) a different approach has been implemented, the MC@NLO method [71, 72]. In this approach, the NLO QCD predictions are obtained using the DGLAP evolution equations with NLO matrix elements, which are then consistently matched to parton showers, and subsequently hadronised. This is achieved combining the HERWIG Monte Carlo event generator described above, with NLO calculations of rates for QCD processes. An alternative to the MC@NLO approach developed in this thesis is presented in Chapter 6.

Chapter 5

Heavy quark measurements

In this chapter, a brief review of the different tagging techniques and previous measurements of beauty and charm quark production is presented. The emphasis will be made on the latest measurements from the HERA experiments H1 and ZEUS. The experimental methods will be described and the theoretical predictions used to compare with those data will be quoted.

5.1 Experimental techniques

The methods to identify heavy quarks are basically similar among the different high energy physics experiments dealing with the signatures from the decay of heavy hadrons. The identification methods most commonly used at HERA will be described next. The different algorithms are often combined to enhance the separation of the heavy quark signal from the light background.

- **Resonance Reconstruction**
  In this technique, the particles from the decay of the heavy hadron, which was produced in the fragmentation of the heavy quark, are analysed. From these decay particles the invariant mass of the hadron is reconstructed, such that the number of signal events can be determined from the resonance spectrum, above a non-resonant combinatorial background.
  The invariant mass reconstruction is best suited in decays where all the final state particles can be well measured in the tracking detectors. The advantage of the full resonance reconstruction method is that all details about the heavy quark resonance and decay kinematics are known and therefore the number of events can be determined precisely. The disadvantage comes from small branching ratios and limited detector acceptances and/or poor resolution.

- **Lepton tag**
  Particle identification is one of the most important tools to enhance signals from heavy hadrons and to reduce combinatorial background. In the central drift chambers of the experiments, the energy loss by ionisation dE/dx for a given particle is determined. With this information a discrimination between π, K, p, e or their antiparticles can be achieved.
  The identification of leptons from semi-leptonic decays of heavy hadrons is very important for the selection of heavy quark event candidates. Electron identification is typically done using the tracking chambers and the energy deposited in the calorimeter. Muon identification is done using the central tracks which are consistent with the amount of energy deposited by a minimally ionising particle. These tracks can be extrapolated to signatures in the muon chambers. The lepton identification at ZEUS is one of the main topics of this thesis and it will be treated in detail in Chapter 7.

- **The p_t^{rel} method**
  An observable which reflects the characteristics of the quark masses in a semi-leptonic decay is the transverse momentum of the lepton relative to the direction of the jet axis, p_t^{rel}, as shown in Figure 5.1. Beauty quarks are significantly heavier than charm and lighter flavour quarks and this is reflected in their decay kinematics. Due to the heavy beauty quark mass, the p_t^{rel} spectrum of muons originating from beauty quarks is harder than the p_t^{rel} spectrum from charm and light quarks. This technique uses this difference to extract statistically the relative contributions from beauty, charm and light flavour quarks in a given event sample.
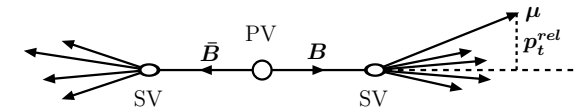
Figure 5.1: The p_t^{rel} variable is the transverse momentum of the muon relative to its associated jet.

- **Life time**
  The reconstruction of vertices displaced from the primary interaction point give information about the life time of heavy hadrons. With this method the combinatorial background is reduced with respect to other methods because the tracks of the decay particles of the meson are required to come from a common secondary vertex.

- **Impact parameter method**
  The impact parameter of a track is defined as the distance of closest approach

of a track to the primary vertex. The impact parameter of a track is defined to be positive if the angle between the jet direction and the line connecting the vertex and the point of closest approach of the track is less than 90°, and as negative otherwise (See Figure 5.2). Negative signed impact parameters are caused by resolution effects of tracks of particles coming from the primary vertex, and the positive signed impact parameter reflect the convolution of the resolution and the life time of heavy hadrons. This method increases the statistics in case the reconstruction of secondary vertices is not optimal, because it only depends on the measurement of the impact parameter of few tracks.
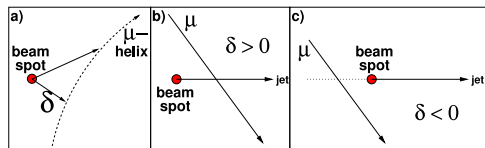
Figure 5.2: The impact parameter variable and definition of its sign. From [73].

- **Significance method**
  From the signed impact parameter of a track a quantity called signed significance can be derived by dividing the measured signed impact parameter by the estimate of its resolution: $S = \delta/\sigma(\delta)$. Properly reconstructed tracks with large impact parameters tend to have large significance values while badly reconstructed tracks with large resolution remain in the core of the distribution as shown in Figure 5.3. The quantities S_1 and S_2 are defined as the significance of the track in the event with the highest and second highest absolute significance respectively.
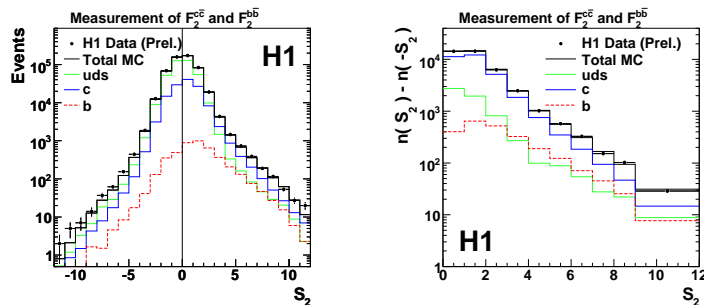
Figure 5.3: Significance distribution S_2 before (left) and after subtraction (right). From [74].

Mirroring the negative bins of the significance distribution at $S = 0$ and subtracting them from the positive bins, leads to significance distributions where the symmetric effects around zero are removed. The fractions of charm, beauty and light quarks of the data are extracted using a fit to the subtracted S_1 and S_2 distributions.

- **Double tag**
  Events in which both heavy quarks can be identified are of particular interest for this work. When a pair of heavy quark-antiquark is produced in the hard interaction the study of the final state configurations provides valuable information about the parent quarks. Double tagging techniques are typically based in the identification of leptons and/or the reconstruction of heavy mesons e.g. $ep \to b\bar{b}X \to \mu\mu X'$ or $ep \to b\bar{b}X \to D^*\mu X'$. The samples of these channels profit from low background. Another advantage of this techniques is that they can cover almost the full phase space for heavy quark production, allowing a direct measurement of total $Q\bar{Q}$ cross sections. These methods are constrained mainly due to statistics. A description of the double tagging technique using the $D^* + \mu$ channel will be presented in Chapter 6.

5.2   Charm measurements

The charm quark predicted in 1970 by Sheldon Glashow, John Iliopoulos, and Luciano Maiani, was first observed in November 1974, with the simultaneous discovery of the J/ψ charm particle at SLAC by a group led by B. Richter [75] and at BNL by a group led by Samuel C. Ting [76]. The experimental signature was a resonance at 3.1 GeV, which was interpreted as a $c\bar{c}$ bound state.

First observations of charm production at HERA date back to the year 1995 [77, 78]. Since then with the increase of the statistics and the continuous upgrade of the detectors charm has been measured in a number of analyses. A compilation of all charm results at HERA can be found e.g. in [79].

Charm quarks from open charm production are tagged using the full reconstruction of charm hadron decays into charged particles. The 'golden' decay channel corresponds to the D^* meson via: $D^{*+} \to D^0\pi_s^+ \to (K^-\pi^+)\pi_s^+$. The mass difference between the D^* and the D^0 mesons is only a few MeV above the pion mass, which causes the suppression of the combinatorial background leading to an enhanced signal to background ratio. The number of D^* mesons is obtained through the observable $\Delta m = m(K^-\pi^+\pi_s^+) - m(K^-\pi^+)$ which provides good mass resolution since the track errors of the kaon and the pion largely cancel [80]. In that publication differential cross sections and D^*-jet correlations where studied in addition to the D^*, D^*-jet, and D^*-dijet photoproduction cross sections. The results were compared to NLO calculations in the massive (FMNR) and in the massless (ZMVFNS) schemes

and to a matched scheme (GMVFNS). It was observed that the charm photopro-
duction is in general reasonably well understood but that none of the calculations
describe all details of the differential measurements, as shown in Figure 5.4.
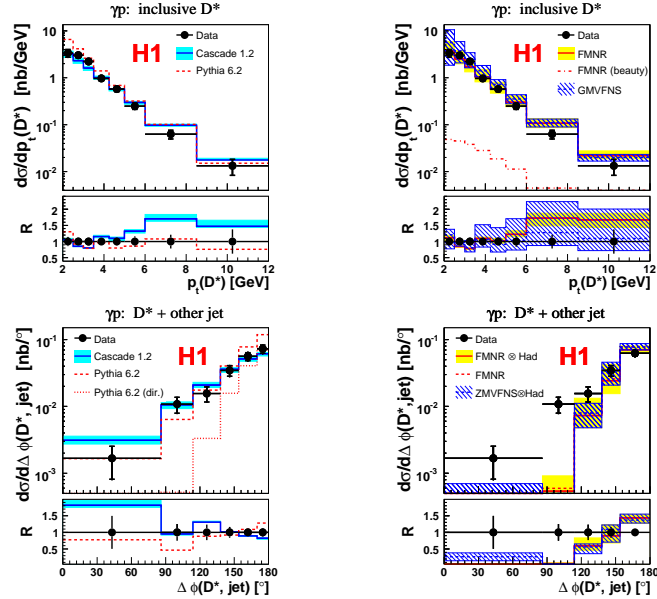
Figure 5.4: Top: Inclusive D^* cross section as a function of $p_t(D^*)$. Bottom: D^*+jet
cross sections as a function of $\Delta\phi(D^*, jet)$. The measurements are compared with
the predictions of PYTHIA and CASCADE on the left and of the next-to-leading order
calculations FMNR and GMVFNS on the right. From [80].

A lifetime tag allows to reconstruct also other D mesons apart from D^* mesons,
e.g. the lifetime of the D^+ meson has been measured for the first time at HERA
with the ZEUS micro-vertex detector [81]. The $D^\pm$ mesons have been reconstructed
in the decay channel $D^+ \to K^-\pi^+\pi^+$ and the corresponding anti-particle decay.
The decay length significance has been computed resulting in an enhanced signal
to background ratio. In [82] and [83] the inclusive production of D^+, D^0, D_s^+ and
D^{*+} mesons in deep inelastic scattering was studied by the reconstruction of a sec-
ondary vertex. The ratio of neutral to charged D-meson production ($R_{u/d}$), the
strangeness-suppression factor in charm fragmentation (γ_s), the fraction of charged
D mesons produced in a vector state (P_v^d) and the open charm fragmentation frac-
tions measured in those analyses agree with results obtained in charm production

and in e^+e^- annihilation. See Figure 5.5. These measurements support the hypoth-
esis of the universality of the charm fragmentation functions.
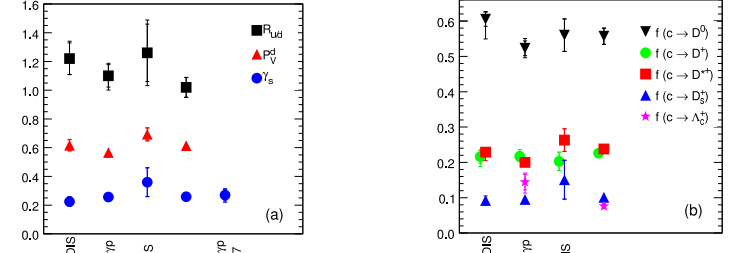
Figure 5.5: Ratio of neutral to charged D-meson production rates ($R_{u/d}$), the
strangeness-suppression factor in charm fragmentation (γ_s), and the fraction of
charged D mesons produced in a vector state (P_v^d) (left). The fraction of c quarks
hadronising as charm mesons and baryons (right). From [83]

The results presented in [84] measure the production of $D^{*\pm}$ mesons using the
ZEUS beam pipe calorimeter, which allows the first measurement of the transition
region between photoproduction and deep inelastic scattering. The cross sections
are compared to the predictions of two different NLO calculations, one designed
for photoproduction (FMNR) while the other for DIS (HVQDIS). Both calculations
predict similar cross sections in the intermediate Q^2 region, and agree well with the
measurements, as shown in Figure 5.6.
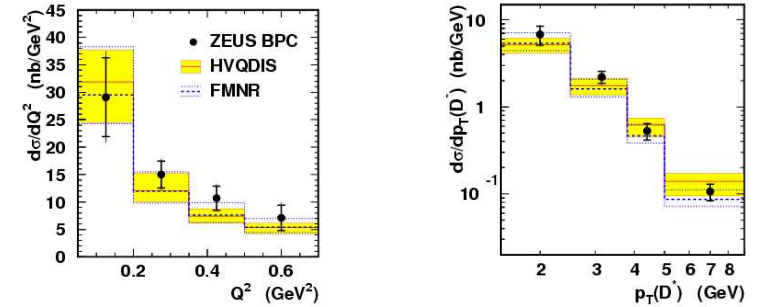
Figure 5.6: Differential D^* production cross section as a function of Q^2 (left) and
$p_T(D^*)$ (right) compared to the HVQDIS and FMNR NLO predictions. From [84].

5.3 Beauty measurements

The beauty quark was discovered in 1977 at FERMILAB [85] via the Υ resonance at 9.5 GeV. Since then extensive studies have been made for example in $p\bar{p}$ collisions at the $Sp\bar{p}S$, in $\gamma\gamma$ interactions at LEP, in pp collisions at the Tevatron collider and in ep collisions at HERA (see e.g. [86] and references therein).

While theoretical calculations for beauty in perturbative QCD are expected to give more reliable predictions than for charm, the beauty measurements are more challenging for the experiments than charm measurements because beauty cross sections are significantly smaller than those for charm. Measurements at LEP and early measurements at the Tevatron showed large discrepancies between data and NLO predictions compared to the charm sector (see e.g. [87]). Over the years this difference has been reduced by both more refined theoretical and experimental methods. Improvements on the experimental side include the use of b-jets and B-hadrons rather than extrapolating to b quarks. From the theoretical side, the description was improved introducing e.g. the fixed order and next-to-leading log (FONLL) scheme and using improved fragmentation and parton density functions. Recent publications from Tevatron show a better agreement of the data and NLO calculations [88].

Previous measurements of beauty at HERA are summarised in Figure 5.7. The ratios of the measured cross section over the theoretical predictions from fixed order massive NLO calculations are shown as a function of the photon virtuality Q^2. The differential cross section for b-quark production as a function of the b-quark transverse momentum $< p_t^b >$ is also shown. The different channels and tagging methods used are also displayed. It is important to mention that the phase space of the different analysis may differ considerably. In most analyses the data tend to be somewhat higher than the QCD NLO massive predictions but are still in agreement taking into account the experimental uncertainties and the corresponding theoretical uncertainties reflected in the differences between the MRST04 and the CTEQ6HQ predictions. The larger deviations seem to increase towards low transverse momentum of the b quark and lower virtualities.

Most previous measurements of beauty at HERA selected events by requiring the presence of one or more jets, tagged by a muon or electron from the semileptonic decay of one of the heavy quarks, or by tracks originating from a secondary vertex. This restricts the measurements to high p_t of the b quarks. For this work the analyses where beauty events are selected using double tagging techniques are the more relevant ones. Next the $b\bar{b} \to \mu\mu X'$ channel will be described and the case of the $b\bar{b} \to D^*\mu X'$ channel will be treated in detail in Section 6.5. The cross sections measured in those analyses will be compared to the theoretical predictions at NLO calculated in Chapter 6. Also a new analysis is started in Chapter 7 following the method used in the dimuon analysis.
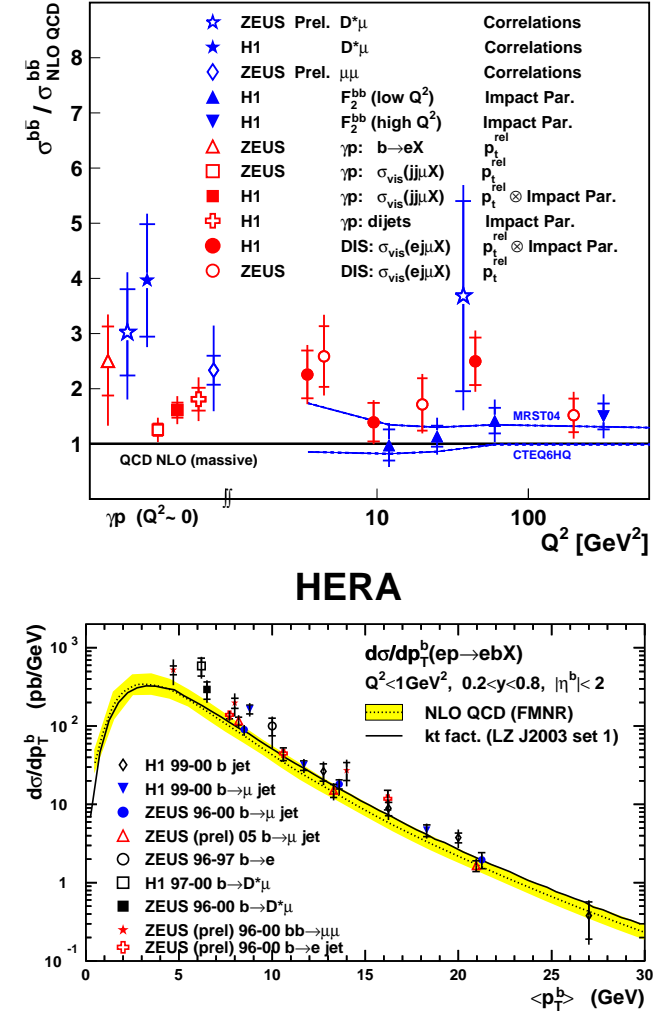
Figure 5.7: Summary of previous beauty measurements at HERA . The ratio between the measured cross sections and the corresponding NLO predictions are shown as a function of the photon virtuality Q^2 (top, from [89]). Differential cross section for b-quark production as a function of the mean transverse momentum of the quark $< p_t^b >$ (bottom, From [90]).

5.3.1 Dimuon analysis

In [52] beauty production with events in which two muons are observed in the final state has been measured at ZEUS. In this analysis a low p_t threshold for muon identification, in combination with the large rapidity coverage of the ZEUS muon system, gives access to essentially the full phase space for beauty production. Two main event classes contribute to the beauty signal to be measured. The first kind are events in which the two muons originate from the same parent B hadron, e.g. through the sequential chain $b \to c\mu X \to s\mu\mu X'$. These yield unlike-sign muon pairs produced in the same event hemisphere and are constrained to dimuon invariant masses of $m_{inv}^{\mu\mu} < 4\,\text{GeV}$. The second kind are events where the two muons originate from different beauty quarks of a $b\bar{b}$ pair. These yield both like- and unlike-sign dimuon combinations, depending on whether the muon originates from the decay of the primary beauty quark or from a secondary charm quark, and whether $B^0\overline{B^0}$ mixing has occurred. Such muons will be predominantly produced in different hemispheres, and tend to have large dimuon masses.

To extract the signal the events were separated by the muon charges into like- and unlike-sign dimuon samples and further separated depending on the dimuon invariant mass. The resulting dimuon mass distributions for the low and high mass, like- and unlike-sign subsamples are shown in Figure 5.8. The expected contributions from the different processes is also shown.
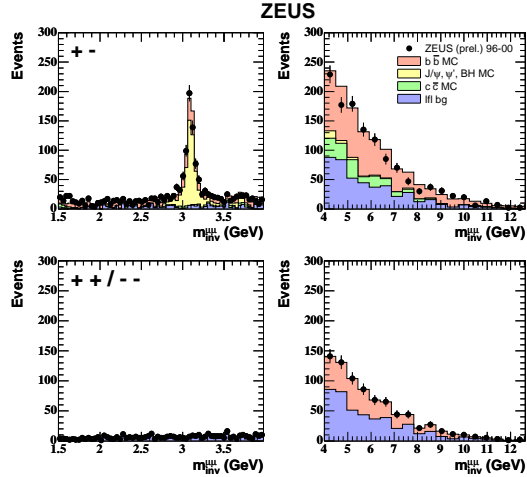
Figure 5.8: Dimuon mass distributions of unlike sign dimuon pairs in the low mass and high mass subsamples, as well as like sign dimuon pairs in the low and high mass subsamples. From [52].

An additional muon-isolation criteria was applied to the samples. Figure 5.9 shows the muon p_t and η distributions for nonisolated unlike-sign dimuon pairs, combining the low and high mass samples. In that analysis it was observed that the charge of the light-flavour fake muon pairs is almost uncorrelated, i.e. light flavour background contributes almost equally to both like- and unlike-sign dimuon distributions. Therefore, once the other background contributions (from charm, heavy vector mesons and Bethe-Heitler) are known, the difference of the like- and unlike-sign distributions can be used to measure the beauty contribution to the total event sample.
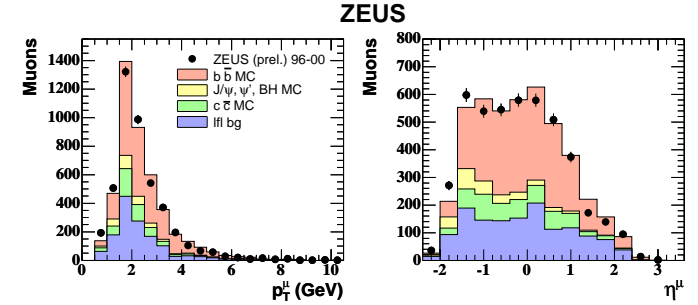
Figure 5.9: Muon transverse momentum (left) and pseudorapidity distribution (right) from both high and low mass dimuon pairs. From [52].

The resulting visible cross sections were initially only compared to LO + PS Monte Carlo predictions due to the lack of proper NLO predictions. The differential distributions are shown in Figure 5.10.
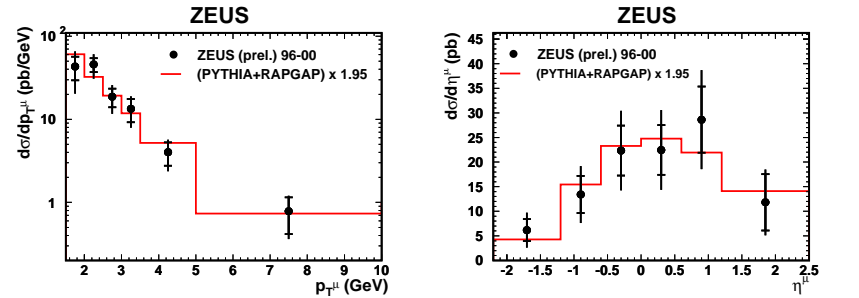
Figure 5.10: Cross sections $d\sigma/dp_t^\mu$ (left) and $d\sigma/d\eta^\mu$ (right) for muons from b decays in dimuon events. The data (solid dots) are compared to the scaled sum of the LO + PS predictions from PYTHIA and RAPGAP (histogram). From [52].

Chapter 6

The FMNR⊗Pythia interface

In order to obtain predictions at next-to-leading order for heavy flavour processes at HERA, a new tool was developed in this thesis work: the FMNR⊗Pythia interface. This chapter will deal with the implementation and the application of this new method to calculate NLO QCD predictions at visible level in the photoproduction regime.
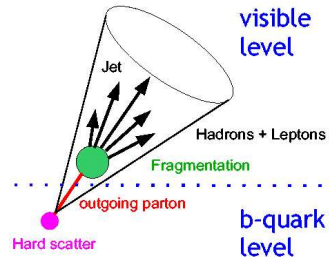
Figure 6.1: Different regions for NLO calculations: quark- and visible-level.

In the previous chapter it was mentioned that several heavy flavour production channels studied at HERA have been compared to next-to-leading order QCD predictions based on the FMNR massive fixed order calculations. These calculations are currently the only ones available at NLO which include a fully differential description of the parton-level final states, and therefore a non-trivial propagation of cuts at the visible level (i.e. on variables measured directly in the detector). To achieve this, the partons need to be fragmented and decayed to measurable hadron or lepton final states. Figure 6.1. For relatively simple cases, this can be implemented through a numerical or analytical parametrisation of the parton-hadron level relation, obtained from separate MC simulations tuned on measurements, which are then directly appended to the FMNR prediction. For final states with correlated cuts on several final state particles, such as in [52, 91], this is not easily possible, although it has been attempted [92]. Nevertheless, NLO predictions for such final states are needed.

One solution to this problem is the MC@NLO approach –already implemented for LHC and Tevatron– which is not yet available for HERA. In that approach NLO QCD matrix elements are incorporated to parton showers, combining the Herwig Monte Carlo event generator with NLO calculations of rates for QCD processes.

The alternative proposed here is based on an interface of the FMNR program to Pythia. Such an interface is not available by default. To implement it, the FMNR program needs to be transformed into a genuine Monte Carlo event generator through the application of a procedure called RedStat. Then, the "Ale Couches accord" interface is used to make the match to Pythia 6.2, from where the description of the full B-hadron decay chain is obtained. No attempt is made to include additional parton showering. A description of the different steps to obtain the FMNR⊗Pythia interface will be given next, as well as some examples of the application of this new method to make predictions for HERA data.

6.1 The FMNR program

FMNR is a FORTRAN program that makes cross-section calculations at NLO in QCD for heavy quark production in ep and γp collisions. It is designed to give predictions for the photoproduction regime (photon virtuality $Q^2 < 1\,\mathrm{GeV}^2$). It contains point-like and hadronic photon coupling to the heavy quarks (as illustrated in Figure 4.8) in the massive fixed order approach. As described in Section 4.4.3, in this scheme, the quarks are produced dynamically (i.e. they are not included in the structure functions) and the relevant scale is the mass of the heavy quarks (m_Q where $Q = c, b$). This makes this approach particularly valid when the renormalisation scale $\mu^2 \sim m_Q^2$.

In addition to quark-level predictions, the FMNR program provides a framework to fragment e.g. b quarks into B hadrons, and simulate the decay of these hadrons by interfacing them to appropriately chosen decay spectra. However, decays to complex final states, like $D^* + \mu$ from the decay of the same B hadron with cuts on both particles, cannot be easily implemented in this scheme.

A straightforward interface of the parton-level events produced by FMNR to a Monte Carlo-like fragmentation and simulation chain is not practical since weights (either positive or negative) are assigned to the output events. These span over more than 8 orders of magnitude as is shown in Figure 6.2. FMNR also differs from a traditional Monte Carlo generator because the events are not created fully randomly, but sets of correlated events are created in a systematic order, and thus the complete data set must be considered in order to get meaningful results. This makes such an approach extremely inefficient because high statistics needs to be generated in order to keep statistical fluctuations low.
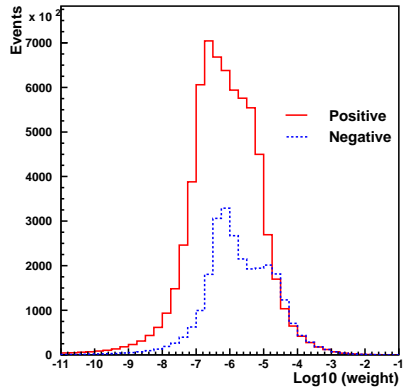
Figure 6.2: Distribution of weights for the generated FMNR events.

As seen in Figure 6.2, in most cases the weights assigned to the events are within four orders of magnitude. However, there also exist cases in which a pair of similar events are created with relatively large (but oppositely signed) weights. This is due to the fact that in the phase-space region where FMNR performs the calculations, collinear and infrared divergences are present [93]. Physically, these paired events correspond to two distinct but similar processes: In the first case, a $b\bar{b}$ pair and a gluon are produced in the collision, and the gluon is such that it is either very soft (infrared divergencies) or remains near one of the heavy quarks or initial state partons (collinear divergencies). In the second case, the gluon not only remains near one of the partons but also at some later time is reabsorbed (virtual gluon, see Figure 6.3).

For the cross section, the process with e.g. the soft gluon contributes with positive weight, but gives a divergent contribution[1], and the interference term between the LO process and the process with a virtual gluon yields an equally diverging contribution with negative weight, such that the two contributions almost cancel.

FMNR overcomes the problem of the soft and collinear divergences by generating sequences of topologically correlated events in such a way that the cancellation is performed by the integration over that phase-space region. The output of FMNR is hence weighted partonic events with a heavy quark-antiquark pair, and events with the pair plus an extra parton (a gluon or a light quark or anti-quark).

---

[1]in practice, the "divergence" is parametrised by large, but still finite, weights

Figure 6.3: Example of processes with positive or negative weight, and their contribution to the cross-section.

However, problems do occasionally arise because the histograms used to plot the output are discretely binned, and it can happen that one of the two paired events will end up in one histogram bin, while the other event with only very slightly different topology ends up in the adjacent one. When this happens the two events can not cancel one another, and so the two adjacent bins get entries with relatively large weights. It is then necessary to produce many more events with smaller weights for the histogram to smooth out. Although the contributions to the cross section are finite at this point, the values of the weights for the generated events span more than 8 orders of magnitude, as seen in Figure 6.2.

A solution to this problem is to find all paired events and suitably average them before they are output into a histogram, or written to an output file. This is exactly what the "REDuced STATistics" option does, as will be explained in detail in the following section.

6.2 REDSTAT

REDSTAT is a group of subroutines implemented as an extension to the standard FMNR program. It is designed to:

- reduce the range of weights for the generated events;
- reduce the necessary statistics without loosing NLO accuracy;
- improve run-time efficiency.

The advantage of the method is that it is based in a simple idea, although the implementation inside the FMNR program is far from trivial. The method is as follows;

REDSTAT monitors all the parton level events as they are generated by FMNR, and searches for events with weights higher than a given threshold (Figure 6.4). The threshold is chosen such that the amount of positive weighted events and negative ones is almost equal above that threshold, indicating that almost all contributions originate from paired events. Reference events selected in this way are compared to events generated immediately afterwards (Notice that FMNR generates sets of correlated events). If one or more events have large but opposite sign weights and similar kinematics with respect to the reference event they are then combined with it into a new single event, using a weighted average of the four-momentum of the partons and assigning the sum of the weights as new weight. For events with weights below the threshold, REDSTAT makes a random decision to keep the event with a probability proportional to its weight (sampling approach) and sets the weight of the sampled events to the threshold.
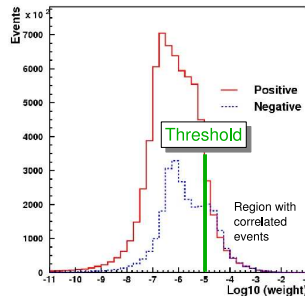
Figure 6.4: Example of a threshold used in REDSTAT.

Events are considered to have similar kinematics when the difference in transverse momentum (p_T), rapidity (ζ) and azimuthal angle (ϕ) of the $b\bar{b}$-pair and the gluon are less than user cut values that should reflect the experimental detector resolution.
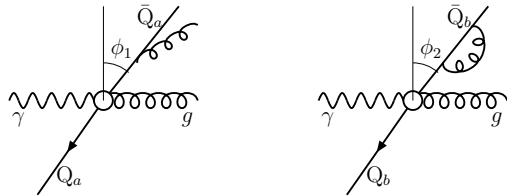
Figure 6.5: Two different events with similar kinematics. Here for example the azimuthal angle angle ϕ of the events will be compared.

After this procedure, as can be seen in Figure 6.6, the range of weights is reduced to almost one order of magnitude and the number of generated events is also reduced, therefore improving the run time efficiency of subsequent applications using these events as input.
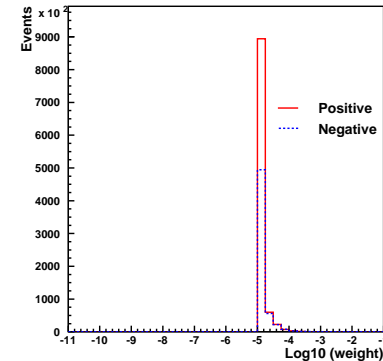
Figure 6.6: Distribution of weights for the generated FMNR events after REDSTAT.

This method preserves the NLO accuracy for the relevant spectra (e.g. b quark p_T and angular distributions) and cross-sections at parton level, as long as the chosen binning is not larger than the assumed resolution (Figure 6.7).

Finally, an optional output file for the interface to other packages is created. This is an ASCII file containing the information of the generated parton level events. For each event, this includes e.g. the assigned weight and the four-momenta of the two or three final state partons (see Appendix A).

The caveats of this method are related to the technical details of the REDSTAT implementation, e.g. the optimal threshold used to decide whether or not the events will be combined does not have an universal value. It must be chosen looking at the weights distribution for the generated process. This changes according to the number of generated events (for example, it moves to the left when more statistics is generated because FMNR keeps the total weight sum constant independently of the number of generated events) and according to the heavy quark generated.

It is also important to notice that the default cut-off values of p_T, ζ and ϕ are tuned to the ZEUS detector resolution and for other applications REDSTAT would need an appropriate re-tuning. Detailed information about the technical implementation of REDSTAT and the source code is found in Appendix A.

6.3   REDSTAT results

In this section a selection of REDSTAT results will be presented. The intention here is to probe that the accuracy of the NLO prediction using REDSTAT is unaltered in comparison with the prediction from the original FMNR program.

- **Cross-section prediction at b-quark level for the process $\gamma p \rightarrow b(\bar{b})X$**

  This was calculated using the standard FMNR and compared to the FMNR version including REDSTAT. The kinematic region was $Q^2 < 1\,\mathrm{GeV}^2$, $0.05 < y < 0.85$ and $|\zeta| < 1$. The parameters used in both calculations were:

  - the mass of the b-quark $m_b = 4.75\,\mathrm{GeV}$;
  - the renormalisation and factorisation scales, defined as $\mu^2 = m_b^2 + p_{Tb}^2$, where p_{Tb}^2 is the average of the squared transverse momentum of the two emerging b quarks;
  - and the structure functions CTEQ5M for the proton and GRV-G-HO for the photon.

  For the evaluation of the theoretical uncertainties (relevant for Section 6.5), the scales were varied by a factor 2, and the mass of the beauty quark was varied between 4.5 and 5 GeV. The variations were done simultaneously such that the spread was maximised. The uncertainty of the structure functions turned out to be small in comparison and is therefore neglected.

  Additional REDSTAT parameters were applied to the two heavy (anti)quarks:

  - weight threshold $= 10^{-5}$;
  - maximal difference in transverse momentum of the partons $p_T = 1.0\,\mathrm{GeV}$;
  - maximal difference in rapidity $\zeta = 0.20$;
  - maximal difference in the azimuthal angle $\phi = 0.3$ rad.

  The results shown in Table 6.1, demonstrate that the NLO accuracy of the standard FMNR is preserved after the application of the REDSTAT option.

	$\sigma_{\gamma p \rightarrow b(\bar{b})X}$
FMNR (standard)	4.95 nb
FMNR with REDSTAT	4.94 nb

Table 6.1: Comparison of NLO cross-section predictions using FMNR without/with the REDSTAT option, for rapidity of the b-quark or antiquark $|\zeta| < 1$.

For the next examples two more samples were generated, one using the standard FMNR program to generate ~ 10 times the number of events of the previous samples, and another sample where the REDSTAT parameters were optimised to obtain a faster running time. The number of events generated in each sample are displayed in Table 6.2.

Sample	Number of events
FMNR (original)	31318299
FMNR with REDSTAT	3159440
FMNR high statistics	322391999
FMNR with fast REDSTAT	3077217

Table 6.2: Number of generated events in the different samples.

- **Comparison of transverse momentum distributions of the $b(\bar{b})$-quark**

  The same cuts as in the previous example were applied. The REDSTAT option yields a good description of the b-quark p_T, as shown in Figure 6.7. The small differences in the shapes of the distributions are due to statistical fluctuations of such a typical FMNR run.
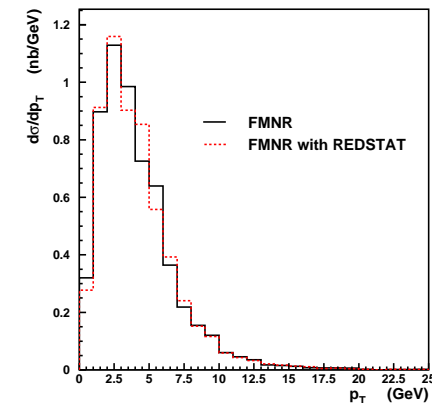
Figure 6.7: Comparison of the $b(\bar{b})$-quark transverse momentum distributions using the standard FMNR (continuous line) and FMNR with REDSTAT (dashed line).

This is illustrated further in Figure 6.8. It is important to notice that the statistical errors need a special treatment here, because the events are not generated with weight one, as in any generic Monte Carlo. Therefore, in order to properly estimate the statistical fluctuations, to take into account the weight of the events, 10 additional samples of FMNR runs were generated. The same statistics and parameters as the FMNR (original) sample in Table 6.2 were used in each of the 10 samples. The only difference was that the seed of the internal random number generator in FMNR was changed, to take values from 1 to 10.

A p_T distribution was obtained as the mean value of the p_T distributions of the 10 samples. The error of which has a variance $V(\bar{x}) = \sigma^2/N$. This mean distribution (called standard in Figure 6.8) is compared to a run with 10 times more statistics and to the version using REDSTAT. After REDSTAT, the fluctuations are expected to be smaller than in the original FMNR, since the probability to split a correlated pair of events at the bin boundary is reduced.
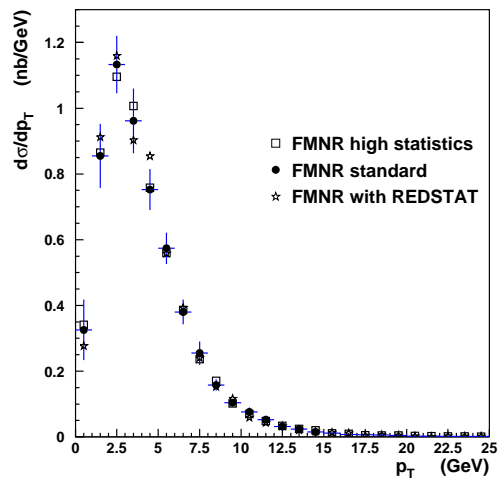
Figure 6.8: $b(\bar{b})$-quark transverse momentum distributions using the original FMNR with 10 times more statistics (squares), a mean of 10 FMNR samples (full circles, the error bars are the statistical errors properly accounted for the different event weights), and FMNR using REDSTAT (stars).

• **Variation of detector resolution parameters**

A comparison between the run using standard values tuned for ZEUS ($\Delta p_T = 1.0$ GeV, $\Delta\zeta = 0.2$ and $\Delta\phi = 0.3$ rad) and a run with significantly wider values ($\Delta p_T = 1.5$ GeV, $\Delta\zeta = 0.38$ and $\Delta\phi = 0.45$ rad), which therefore allows a faster performance, is shown in Figure 6.9. The fluctuations result from the differences in the event combination procedure, since the same original FMNR events are generated in each case.
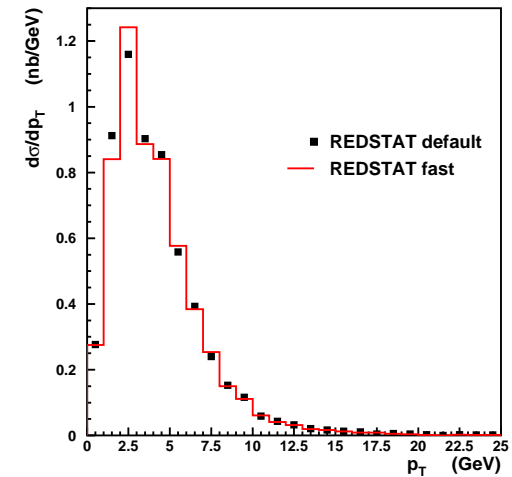
Figure 6.9: Comparison of the $b(\bar{b})$-quark transverse momentum distributions using REDSTAT with default parameters (1 GeV, 0.2, 0.3 rad) and fast REDSTAT with wider cut values (1.5 GeV, 0.38, 0.45).

6.4 The FMNR⊗Pythia Interface

The method to obtain the interface of the FMNR parton-level predictions to the fragmentation and decay chain from Pythia/Jetset is a two-step process (as shown in Figure 6.10). The first step of this FMNR⊗Pythia interface consists in the application of the RedStat extension to the FMNR program. RedStat is used to transform FMNR into an effective Monte Carlo-like parton-level event generator, through the combination of events with similar kinematics and a sampling approach as described in Section 6.2. The parton level events obtained this way are written to an output file. In the second step, these parton level events are read back into the Pythia 6.2 program trough the "Les Houches accord" user interface, where the Pythia/Jetset full fragmentation and decay chain can be applied.
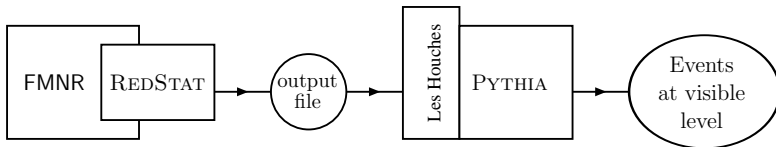
Figure 6.10: Schematic view of the FMNR⊗Pythia interface.

The first part (FMNR + RedStat) was already extensively discussed in the previous sections, the discussion will now move on to the second part of the interface.

Once the output ASCII file containing the information of the parton level events from RedStat is available, a "Les Houches" interface routine (UPEVNT) sequentially reads one event from the ASCII file and fills it into the "Les Houches" interface variables to be used as input by Pythia. At this stage, a "reasonable" (i.e. physically possible) colour flow is assigned to each FMNR parton level process. FMNR does not provide this information, which is needed in the case of string fragmentation. The difference due to different possible colour flow assignments should be included in the systematic error if this is critical for the application.

The initial state partons are allowed to have an intrinsic k_T (typically $\sim 300\,\text{MeV}$) as implemented in Pythia. This has a negligible effect on the resulting cross-sections ($\sim 1\%$). Parton showering is **not** allowed in order to avoid double counting of higher order contributions. This is the main difference with respect to MC@NLO for HERA (in preparation [94]).

Fragmentation of heavy quarks close to production threshold turned out to be a non trivial issue. Since the details of the threshold treatment were found to be much more important than the choice of a particular fragmentation function, the

Peterson formula with $\epsilon = 0.0035$ is used for convenience. Three approaches are considered:

- **Independent fragmentation in the Pythia model.**
  This is used because FMNR does not provide colour connections on a event-to-event basis, and colour connections are not required in this model.

- **Fragmentation in the Lund string model.**
  For this, reasonable colour connections have to be associated to each FMNR event.

- **Independent fragmentation scheme as provided by FMNR.**
  Setting e.g. the B-hadron momentum equal to the b-quark momentum before reducing it according to the Peterson formula. This neglects threshold corrections due to the need of simultaneous conservation of energy and momentum.

Finally, in the first two cases, the full decay tables and kinematics implemented in Pythia 6.2 are used to obtain a full hadron-level event. Therefore, non-dominant arbitrarily complicated decays, such as $B \to D^*D$ followed by a $D \to \mu X$, or muons through intermediate J/Ψ or τ states, are automatically included. The branching ratios were empirically corrected later (at analysis level) to correspond to those obtained from the Particle Data Group (PDG). Unless otherwise stated, the 2nd approach is used for the central predictions, while the first enters the systematic uncertainty. The third case could be used only for relatively simple final states (e.g. independent production of a muon from each heavy quark), and the resulting differences with respect to the first two cases were extrapolated to the more complicated ones (e.g. correlated production of two muons from the same b quark), and used as a systematic check.

6.4.1 FMNR⊗Pythia interface parameters

The parameters set within the FMNR⊗Pythia interface which were used to calculate the next-to-leading order predictions presented in this thesis are given in Table 6.3. The parton density functions used were CTEQ5M for the proton and GRV-G-HO for the photon. The renormalisation and factorisation scales μ were chosen to be equal and parametrised by $\mu_0 = \sqrt{m_b^2 + p_T^2}$, where p_T is the transverse momentum of the two emerging b quarks, and m_b is their invariant mass. Estimates for the theoretical uncertainties were obtained by simultaneously varying $4.5 < m_b < 5.0\,\text{GeV}$ and $\mu_0/2 < \mu < 2\mu_0$ such that the uncertainty was maximised. Variations of the parton densities led to uncertainties which were much smaller than the uncertainties related to the mass and μ scale variations. They were therefore neglected.

Parameter	FMNR
m_b	4.75 GeV
μ scale	$\mu^2 = m_b^2 + p_T^2$
Q^2	$< 1 \, \text{GeV}^2$
PDF p	CTEQ5M
PDF γ	GRV-G-HO
RedStat	yes

Parameter	Pythia
k_T kick	yes
Parton showers	no
ϵ Peterson	$\epsilon = 0.0035$

Table 6.3: Parameters used in the FMNR⊗Pythia interface.

6.5 Examples of the use of the FMNR⊗Pythia interface method.

In this section two examples of the application of the FMNR⊗Pythia interface will be presented. Since the first comparisons with data where made to measured beauty cross sections, the following is written for the specific case of beauty quarks. All arguments hold in an analog way for charm and some predictions for it are already available [95].

Here the FMNR⊗Pythia interface method will be applied to obtain NLO beauty cross-section predictions for the final state channels $D^*\mu$ and $\mu^+\mu^-$, which were published in [91] and in preparation in [96, 97] respectively, and from which I am co-author. A beauty enriched data sample is obtained in these channels through a significant reduction of the background which results from the use of a double tagging technique. This allows softer kinematic cuts which, in combination with the wide rapidity coverage of the ZEUS muon detectors, results in an enhanced sensitivity to B hadrons produced at low transverse momenta, where the bulk of the b cross-section is concentrated. Under these conditions a direct measurement of the total $b\bar{b}$ cross-section becomes possible without the use of large model-dependent extrapolation factors.

Tagging muons or D^* arising from different b quarks allows to explicitly measure $b\bar{b}$ correlations, while tagging two muons or a muon and D^* from the same b quark yields measurements which are almost insensitive to such correlations. However, the complexity of the decays of these channels and the different cuts applied to the final state particles made a standard calculation of the NLO prediction very difficult, a perfect situation to apply the FMNR⊗Pythia interface.

6.5.1 The $ep \to eb\bar{b}X \to eD^*\mu X$ channel

In the case of $D^* + \mu$ [91, 98] an unlike-sign combination of both particles is observed in the same detector hemisphere if they come from the same b quark, (mainly via $B^0 \to D^*\mu\nu_\mu$) yielding a quite pure b sample; if they come from different b quarks then they are emitted into different hemispheres. This last signature is similar to the one given by charm background, from different c quarks, which produces unlike-sign $D^*\mu$ pairs in a characteristic back-to-back configuration as illustrated in Figure 6.11.
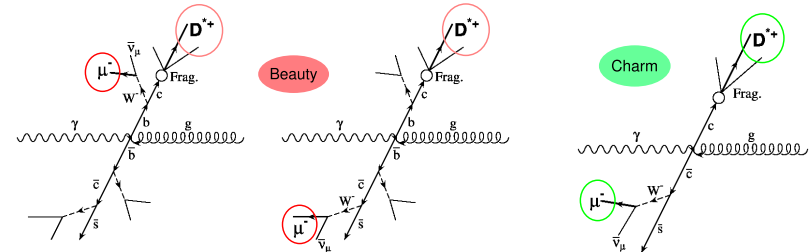
Figure 6.11: Processes leading to $D^* + \mu$ final states.

The distributions of the angular difference $\Delta R = \sqrt{\Delta\phi^2 + \Delta\eta^2}$ between the D^* and the muon (where ϕ is the azimuthal angle) and the invariant mass reconstruction of the $D^*\mu$ system are shown in Figure 6.12.

The distributions are shown separately for like- and unlike-sign events. For unlike-signed events the region $\Delta R > 2$ predominantly corresponds to the back-to-back configuration which is dominated by events from charm. In contrast the region $\Delta R < 2$ is enriched in beauty events in which the D^* and μ originate mainly from the same parent B hadron. In the invariant mass distribution (Fig. 6.12 b) for the beauty-enriched region a peak which can be attributed to the partial reconstruction of the decaying B meson is clearly visible. A comparison with the like-sign sample shows that the low-mass edge of this peak is dominated by background. An invariant-mass cut of 3 GeV $< M(D^*\mu) < 5$ GeV was therefore applied to the $\Delta R < 2$ subsample.

The measured beauty fraction in the inclusive sample, corrected for detector acceptance and branching ratios, was used to obtain the cross-section in the kinematic range $p_T^{D^*} > 1.9$ GeV, $-1.5 < \eta^{D^*} < 1.5$, $p_T^\mu > 1.4$ GeV and $-1.75 < \eta^\mu < 1.3$ as:

$$\sigma_{vis}(ep \to eb\bar{b}X \to eD^*\mu X) = 160 \pm 37(\text{stat.})^{+30}_{-57}(\text{syst.}) \text{ pb.} \qquad (6.1)$$

ZEUS
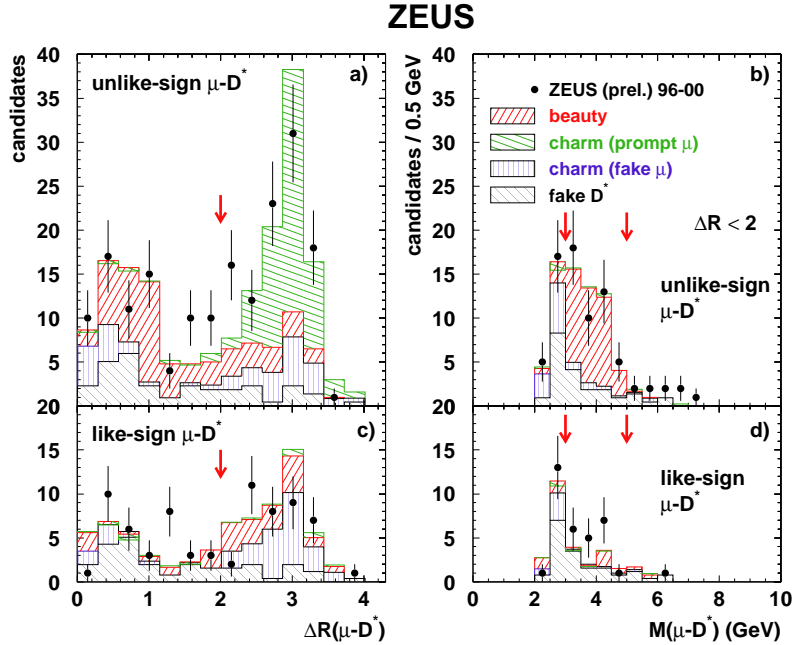
Figure 6.12: $a, c)$ Unlike-sign and like-sign distributions of $\Delta R(D^*\mu)$ and $b, d)$ $M(D^*\mu)$ for data (full circles), beauty and charm signal, fake-μ and fake-D^* backgrounds. From [98].

Visible beauty cross-sections from $ep \rightarrow eb\bar{b}X \rightarrow eD^*\mu X$

The measured visible cross-section Eq. (6.1) is larger than, but still compatible with, the corresponding FMNR⊗PYTHIA NLO prediction of:

$$\sigma_{vis}^{\text{NLO}}(ep \rightarrow eb\bar{b}X \rightarrow eD^*\mu X) = 67^{+20}_{-11}(\text{NLO})^{+13}_{-9}(\text{frag.} \otimes \text{br.}) \text{ pb.} \qquad (6.2)$$

where the first error refers to the uncertainties of the FMNR parton level calculation, and the second error refers to uncertainties related to fragmentation and decay. The FMNR⊗PYTHIA parameters used for the calculation of the central value prediction and the theoretical uncertainties are described in Section 6.4.1.

Strictly speaking, the FMNR predictions are only valid for the photoproduction regime. Here, the Weizsäcker-Williams (WW) approximation [99–101] with an effective $Q^2_{max} < 25 \, \text{GeV}^2$ cutoff was used to include the 15% DIS contribution for a combined cross section. This NLO QCD prediction is also listed in Table 6.4.

A cross section for the same kinematic range, but adding a photoproduction requirement ($Q^2 < 1 \, \text{GeV}^2, 0.05 < y < 0.085$) was also obtained. The result as well as the corresponding NLO predictions from FMNR⊗PYTHIA, are shown in Table 6.4. As in the inclusive case, the prediction underestimates the measured cross-section, but is compatible with the measurement within the large errors.

Finally, these visible level cross-sections were extrapolated to b-quark level using plain PYTHIA. The NLO QCD prediction can then be obtained at parton level directly from the original FMNR calculation. From the comparison of the data/NLO ratios at visible and b-quark level presented at Table 6.4, one can conclude that the PYTHIA extrapolation was reliable. This extrapolation was the only way to compare the cross sections before the Equation(6.2) from FMNR⊗PYTHIA could be calculated [98].

	Cross-section	Measured	NLO QCD	Ratio
Visible	Total	$160 \pm 37^{+30}_{-57}$ pb	67^{+24}_{-14} pb	$2.4^{+0.9}_{-1.3}$
	γp	$115 \pm 29^{+21}_{-27}$ pb	54^{+18}_{-12} pb	$2.1^{+0.8}_{-1.0}$
b level	Total	$11.9 \pm 2.9^{+1.8}_{-3.3}$ nb	$5.8^{+2.1}_{-1.3}$ nb	$2.0^{+0.8}_{-1.1}$

Table 6.4: Comparison of measured and predicted cross-sections. For the measured, the first error is statistical and the second systematic. The NLO predictions at visible level were obtained using FMNR⊗PYTHIA, and the measurement at b-quark level was obtained extrapolating with plain PYTHIA.

Comparison ZEUS - H1

The H1 Collaboration has measured a cross-section similar to the ZEUS photopro-duction measurement of Equation (6.1) in a slightly different kinematic region [102]: $p_T^{D^*} > 1.5$ GeV, $-1.5 < \eta^{D^*} < 1.5$, $p^\mu > 2.0$ GeV and $-1.735 < \eta^{D^*} < 1.735$. Its value is shown in Table 6.5. Using the FMNR⊗PYTHIA interface, the ZEUS cross-section can be extrapolated to the H1 kinematic region. A direct comparison of the two results is shown in Table 6.5. Reasonable agreement is found.

Cross-section		H1	ZEUS (extrap.)
H1 Visible	γp only	$206 \pm 53 \pm 35$ pb	$135 \pm 33^{+24}_{-31}$ pb

Table 6.5: Comparison of H1 and ZEUS visible cross section for $ep \to b\bar{b}X \to D^*\mu X'$. The ZEUS cross section has been extrapolated to the H1 kinematic range.

The corresponding NLO prediction from FMNR⊗PYTHIA is

$$\sigma^{\text{NLO}}_{vis,H1}(ep \to eb\bar{b}X \to eD^*\mu X) = 61^{+17}_{-12}(\text{NLO})^{+12}_{-8}(\text{frag.} \otimes \text{br.})\ \text{pb}. \qquad (6.3)$$

The data to NLO ratio is again consistent with the ones quoted in Table 6.4.

The NLO prediction is somewhat larger than the one evaluated in [102] due to the inclusion of the hadron-like photon contribution, the inclusion of secondary-muon branching fractions for D^* and muons from the same b quark (e.g. $B \to D^*D \to D^*\mu X$, which are difficult to handle outside the FMNR⊗PYTHIA framework), and a detailed simulation of the kinematics of the $b \to B \to D^*$ chain rather than direct collinear fragmentation of b quarks into D^* mesons. This reduces the discrepancy claimed in [102] and is an example for the importance of a detailed treatment of complicated final states.

6.5.2 The $ep \to eb\bar{b}X \to e\mu^+\mu^- X$ channel

The signature of the dimuon channel is very similar to the $D^*\mu$ channel shown in Figure 6.11, and detailed information can be found in [52]. Again, this is a very complicated final state, for which the cross section measurements are being finalised by ZEUS.

Visible beauty cross-sections from $ep \to eb\bar{b}X \to e\mu^+\mu^- X$

For the dimuon channel, a complicated set of muon p_T and η cuts were used for maximal acceptance [52]. Table 6.6 shows the measured visible cross-section com-pared to the NLO prediction from FMNR⊗PYTHIA. The extrapolation to b-quark level was done using PYTHIA and is compared to the NLO prediction, obtained by adding up the (original) FMNR and HVQDIS predictions, for the photoproduction

and DIS regions respectively.

Here, as in the case of the $D^*\mu$ channel, the cross-section comparisons at visible and b-quark level are consistent.

	Cross-section	Measured (prel.)	NLO QCD	ratio
Visible	Total	$63 \pm 7^{+20}_{-18}$ pb	30^{+9}_{-6} pb	$2.1^{+0.8}_{-1.0}$
b level	Total	$16.1 \pm 1.8^{+5.3}_{-4.7}$ nb	$6.8^{+3.0}_{-1.7}$ nb	$2.3^{+1.0}_{-1.2}$

Table 6.6: Comparison of measured and predicted dimuon cross-sections. For the measured, the first error is statistical and the second systematic.

Differential cross sections

Differential cross-sections were also obtained and shown in Figure 6.13. One can observe the general trend of NLO to lie below the data, but consistent within errors. The shape of the distributions is well reproduced by the NLO prediction.

For the correlations between the two b quarks, the reconstructed dimuon mass range was restricted to $m^{\mu\mu} > 3.25$ GeV. This additional cut reduces the probability that both quarks come from the same B-hadron. The corresponding differential cross-section is shown in Figure 6.14. The distribution is reasonably described by the FMNR⊗PYTHIA NLO prediction within the large errors.

The leading order contribution alone reproduces the measured cross section less well [52]. Although the difference in shape is not dramatic, this confirms the impor-tance of contributions from higher order processes.

6.6 Other applications

In principle, the FMNR⊗PYTHIA interface can be used to generate events which can be propagated through the full simulation and reconstruction chain of any experi-ment measuring ep or γp heavy flavour final states (if the chain allows the handling of negative weights). This opens up additional applications, such as cross sections for hadron-level heavy flavour jets, with hadron to parton-level corrections fully con-sistent with the NLO approach. So far, LO+PS Monte Carlos needed to be used for this purpose.

Examples for potential applications in the near future include:
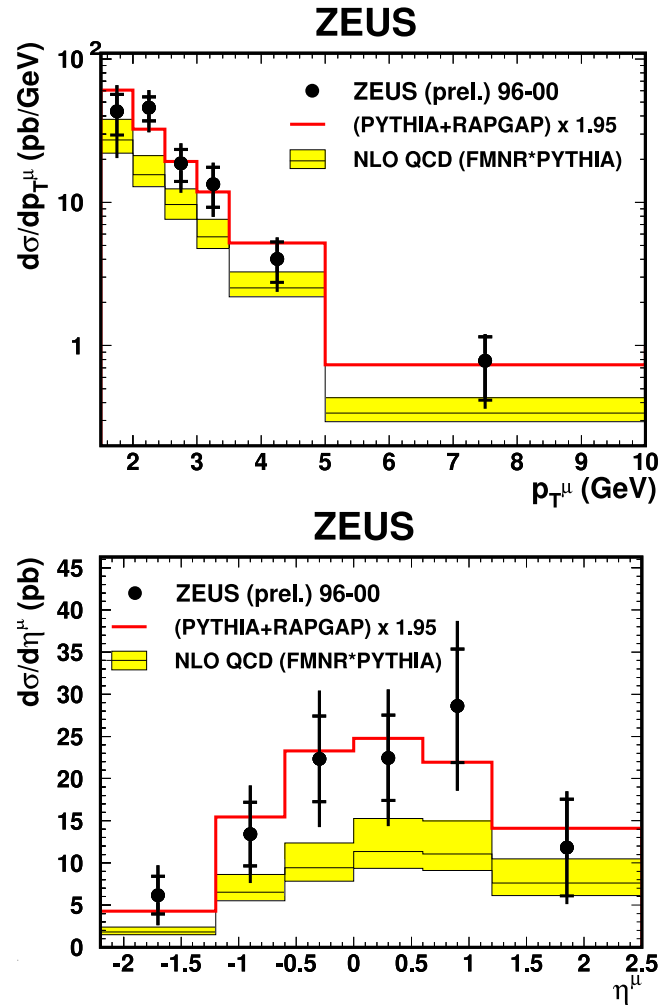
Figure 6.13: Differential cross-sections $d\sigma/dp_T$ (top) and $d\sigma/d\eta$ (bottom) for muons. The data points are compared to the scaled LO prediction from PYTHIA + RAPGAP, and to the NLO prediction from FMNR⊗PYTHIA.
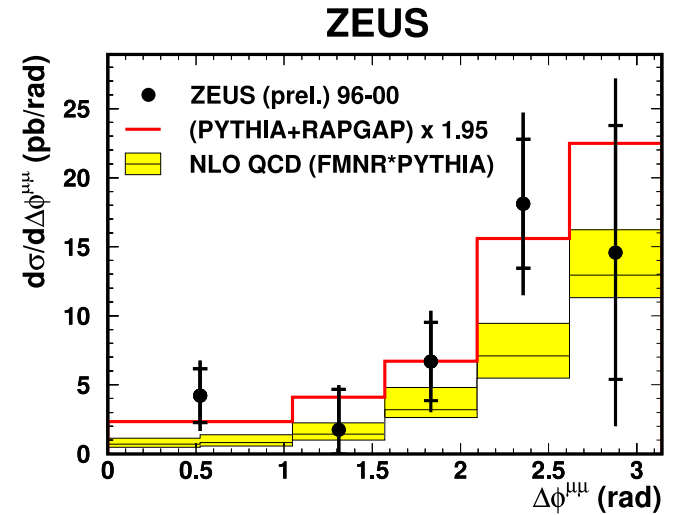
Figure 6.14: Differential cross-section $d\sigma/\Delta\phi$ for muons from different b-quarks.

- evaluation of parton to hadron-level corrections for measurements of the charm fragmentation function at HERA [82, 103];

- evaluation of NLO cross sections for measured $\mu\mu$-jet-jet and μe-jet-jet final states from both charm and beauty[89, 104], for which no NLO predictions exist so far;

- reevaluation and verification of NLO predictions for essentially all earlier HERA heavy flavour results [105–111] at visible level.

These applications will not obliviate the need for calculations using the MC@NLO approach, which will be able to handle final state parton showering in addition. However, they have the virtue of being available immediately.

Chapter 7

^{G}Elec finder and dilepton identification of Beauty

In Chapter 5 the importance of double tagging techniques to identify events where heavy flavours are present was discussed. To compare data from these kind of analyses to NLO predictions a new tool, the FMNR⊗PYTHIA interface, was developed as was described in the previous chapter. If a physics analysis is using a double tagging technique and the final state is a pair of leptons, a reliable lepton identification is essential. This chapter will deal with another new tool, the ^{G}Elec finder, developed in this work for electron identification in beauty quark events. Using this tool a heavy flavour analysis has been started in order to extend the measurement of beauty quark processes to a region of phase space not very much explored at HERA (low transverse momenta). This measurement will also complement previous ZEUS measurements using this time events were a pair of leptons, an electron and a muon, are present in the final state, the $ep \rightarrow b\bar{b}X \rightarrow e\mu X'$ channel. Contributing in this way to the understanding of beauty quark production and its evolution.

At ZEUS the lepton identification is done using the central tracking detectors, the Uranium calorimeter and, for muons additionally, the muon system. The general muon finder ^{G}Muon is implemented to identify muon signatures combining all the different muon finder algorithms at ZEUS. This finder was already extensively tested in several analyses [52, 73, 112] and it is already part of the standard ZEUS reconstruction software. The next part of this thesis work consists in the first stage of the development of a similar algorithm to tag electrons. Using calorimeter and tracking information, like the shape of the energy deposit in the calorimeter and the energy loss by ionisation (dE/dx), to obtain a better separation of b-quark events through an efficient identification of the resulting electron (or positron) from the semileptonic decay of the heavy quark.

To test the efficiency of the new method, it was applied to the reconstruction of the invariant mass of $J/\psi \rightarrow e^+e^-$ and compared to Monte Carlo models for beauty-quark production. The code was implemented in an object-oriented frame named ^{G}Elec, to make it compatible with the already existing ^{G}Muon finder. Therefore, a project using ^{G}Elec and ^{G}Muon, could identify –any– semileptonic muon/electron decay channel of beauty hadrons. The beauty quark cross sections can be measured, for instance, following the method developed for the dimuon channel [52] which used ^{G}Muon only.

A brief description of the event reconstruction at ZEUS will be given next. There the fundamental objects for lepton identification will be described. The muon identification at ZEUS using the ^{G}Muon finder and the discussion on the new ^{G}Elec finder will be treated next. Finally the dilepton analysis $ep \rightarrow b\bar{b}X \rightarrow e\mu X'$ will be presented.

7.1 Event reconstruction at ZEUS

In this section the reconstruction of final-state quantities used at ZEUS for the selection of event candidates where beauty quarks are present will be presented.

The event reconstruction starts from the central tracks found in the central tracking detector using the standard ZEUS tracks reconstruction software. Then particle energies were reconstructed from signals in the calorimeter cells. Energy islands (two dimensional energy clusters) and cone islands (three dimensional clusters) were formed from the calorimeter cells and combined with tracking information to form energy flow objects (EFOs). Using the information from the EFOs, collimated bundles of particles, called jets, were constructed using clustering algorithms. All this process will be shortly described next.

7.1.1 Track reconstruction in the CTD

Tracks at ZEUS were reconstructed based on CTD hits information and are found in several passes. The first pass is called pattern recognition. It consists of two separate 2D fits: a circle fit in the XY plane of the detector and a fit in the sZ plane, being a line fit for the path length s on the circle in XY. Ambiguities in the XY hit position (introduced by only measuring the distance of the ionisation along the field lines and not on which side of the signal wire the ionisation occurred) are removed by assigning CTD segments consisting of up to 8 hits in one cell to proto-tracks. The pattern recognition in sZ uses Z information from the CTD z-by-timing system as well as information from the stereo super layers using the segments from the XY plane fit. The variation in the curvature of the track is taken into account even in the first fast pass.

The second pass is a full 3D helix fit with 5 parameters of the previously determined pattern recognition tracks to the hits. At this step several corrections are applied to the hits and the resulting tracks e.g. corrections due to the non-uniform magnetic field, time of flight corrections, kinks of the track at detector boundaries and energy-loss corrections as well as corrections applied to the hits.

In a third step a main event vertex and secondary vertices are found from the fitted tracks. The association of the tracks to vertices is used as an additional input to refit the tracks. Additionally, the tracks and the error matrices are extrapolated to the CAL inner surface. Thus the positions and directions of the tracks can be used to match them to energy deposits in the calorimeter. More details can be found in [113], an overview of modern track reconstruction methods can be found in [114] and details about the corrections in [10].

7.1.2 Energy reconstruction in the CAL

The signals from the photomultipliers of the calorimeter are converted into particle energy measurements during the event reconstruction. Calibration factors determined in test-beams measurements are used to translate the signals from the photomultipliers into values of energy, which are additionally corrected for detector effects and noise. The main source of noise are sparks in the photomultipliers and hot cells (cells with large signals due to badly behaving photomultiplier or electronics). Hot cells are determined by offline DQM jobs from the calorimeter experts, as explained in Chapter 3. Using the lists of bad channels obtained after the calibration and DQM of the calorimeter those not properly working cells are rejected. Noise signals due to small sparks are suppressed by setting cell energy thresholds for isolated cells. Cells are rejected if there is no signal in the neighbouring cells and the cell itself has a signal amplitude corresponding to less than $80\,\mathrm{MeV}$ in the electromagnetic part of the CAL and less than $140\,\mathrm{MeV}$ in the hadronic part. Bigger sparks are suppressed using the redundant CAL cell readout by two independent photomultipliers.

Persisting differences can be corrected by multiplying energy values in data by a correction factor, as described in [115]. The data correction factors for the electromagnetic and hadronic parts of the calorimeter are summarised in Table 7.1. Additional corrections are needed for parts of dead material that are modeled incompletely as well as for shifts in the modelling of energy losses of minimally ionising particles such as muons. These corrections are applied to the EFOs, as described e.g. in [52].

The total transverse energy E_T^{CAL} is calculated from the corrected information

Calorimeter energy corrections			
CAL section	cell type	1996-1997	1998-2000
FCAL	electromagnetic	+4.0%	+2.4%
	hadronic	−5.0%	−5.9%
BCAL	electromagnetic	+4.0%	+5.3%
	hadronic	+8.2%	+9.6%
RCAL	electromagnetic	+2.2%	+2.2%
	hadronic	+2.2%	+2.2%

Table 7.1: Energy correction factors for the calorimeter for the HERA I running period.

of all cells by the scalar sum of the transverse energy of each individual cell:

$$E_T^{CAL} = \sum_{i=1}^{N_{cells}} E_i \cdot \sin(\theta_i) \tag{7.1}$$

where θ is the angle with respect to the z axis.

7.1.3 Energy flow object reconstruction

The basic information in the calorimeter is the energy content of a cell. The cells in the three sections of the calorimeter (EMC, HAC1, HAC2) are clustered separately in each section to form so called islands. To form islands, all neighbouring cells with an energy content bigger than the noise are grouped together, starting from the cell with the largest signal. By clustering single cells the complete energy deposits of separate particles can be determined. This method can be improved by building so called cone islands. These are obtained combining islands in cones in θ and ϕ, oriented towards the interaction point. The process starts in the HAC2 sections of the calorimeter (the outermost layers) and combines cell islands across layers guided by single pion MC probabilities [116, 117]. The spacial centre of the cone island is determined by a logarithmically weighted centre of gravity. At low momentum however the cone island method has a low resolution and some low momentum particles are not measured at all.

A method to compensate for the low resolution at low momenta is the combination of calorimeter clusters with tracking information from the central tracker to form energy flow objects (EFOs). The p_T dependence of the separate energy resolutions for calorimeter entries and central tracks are shown in Figure 7.1.

Primary vertex tracks having crossed more than 4 CTD super layers are matched to the energy weighted centre of gravity of the CAL clusters. A match is found if

Figure 7.1: Central tracking and calorimeter energy-resolution dependence on the transverse momentum of the corresponding particles. The CTD transverse momentum resolution of the tracks is shown in open circles, that of the CAL in full dots.

the track has a momentum of $|p^{\text{track}}| \in [0.1, 20^{(4\,\text{SL tracks})} \text{ or } 25^{(>7\,\text{SL tracks})}]$ GeV and is either less than 20 cm away from the centre of gravity measured in the plane perpendicular to the cluster vertex connection line at the CAL inner surface or is less far from the centre than the island radius. The EFO momentum is taken from either the calorimeter cluster or the matched track, depending on the resolution of the track momentum as well as the CAL cluster energy resolution. Pion masses are assumed for the matched tracks. For unmatched calorimeter clusters $m = 0$ is assumed and for unmatched tracks $m = m_\mu$ is assumed. A graphical representation of EFOs is shown in Figure 7.2. Details on cone islands and EFO corrections are described e.g. in [52].

Figure 7.2: Examples of track-island matches in EFOs. Four EMC and one HAC1 islands are shown. The islands 1, 2 and 3 form a 3d cone island which is matched to a track. The island 4 is also matched to a track. Island 5 is not matched to a track (neutral particle) and the lower right track is not matched to any island (low momentum particle).

7.1.4 Jet reconstruction

Jets were reconstructed using a k_T-like clustering algorithm [118] based on EFOs. The jet reconstruction definition using this algorithm has the main advantage of being invariant against longitudinal boosts, being insensitive to the emission of very low energy particles (infrared safe) and final state collinear particle splittings (collinear safe). Additionally, the forward particle spray from the proton final-state colour connection (proton remnant) and the rear spray of particles from a potential resolved photon can be removed in a controlled way.

The formation of jets by the k_T algorithm is implemented by the definition of three facts. The first is a test variable (energy-angle resolution) d_{kl} to test if the two hadrons belong to the same cluster (each EFO is considered as a hadron). The second one is a recombination procedure defining the iterative formation of jets from single particle entries in the EFO list. And the last one is a hard scattering scale d_{cut} to separate hard and soft processes.

The used KTCLUS algorithm clusters the EFOs into jets using the following scheme:

- the resolution variables d_{kl} and d_k, d_l are calculated for all pairs of EFOs e_k and e_l as follows:

$$d_k = (p_T^k)^2$$
$$d_{kl} = min((p_T^k)^2, (p_T^l)^2)\Delta R_{kl}^2$$

where $\Delta R_{kl}^2 = (\eta_k - \eta_l)^2 + (\phi_k - \phi_l)^2$.

- The smallest value from the list of resolution variables (d_k, d_l) is determined in two different ways:
  - If d_{ij} is the smallest resolution variable, the two EFOs e_i and e_j are combined into a single *pseudo particle* using the so called E recombination scheme. Here the hadrons are treated as massive particles and their four-momenta are added.
  - If d_k is the smallest resolution variable, the EFO e_k is removed from the EFO list and is included in a soft so called *remnant* jet.

- This process continues until all particles and pseudo particles not included in the remnant jet have resolution variables larger than the hard scale d_{cut}, where $\Lambda_{QCD}^2 \ll d_{cut} \ll s$ with $\sqrt{s}$ the centre-of-mass energy.

This process results in hard final-state jets and remnant jets. The use of the E recombination scheme in heavy flavour studies has proven to be more convenient in comparison with other recombination schemes [118] as the massive approach yields a good agreement of the measurements and theoretical predictions of jets for beauty quarks [119].

7.2   Muon Identification

A highly efficient single-muon reconstruction is needed for an efficient muon tagging with a good signal to background ratio. This has been achieved using the muon system of the ZEUS detector.

7.2.1   Muon signature

Muons mainly lose energy in the detector material due to ionisation. In accordance with the Bethe-Bloch equation muons with $p > 1\,\mathrm{GeV}$ can be considered as minimal ionising particles (MIPs), which have a big penetration power. They do not interact strongly and the energy loss due to radiation (Bremsstrahlung) becomes important only at energies of a few hundred GeV and is therefore negligible here. In the Uranium calorimeter electrons produce showers and are stopped in the electromagnetic part. Hadrons generate longer showers due to strong interaction with the material, whereas muons lose only a small amount of their energy in the calorimeter as they do not produce showers, as pictured in Figure 7.3, reaching the muon chambers.
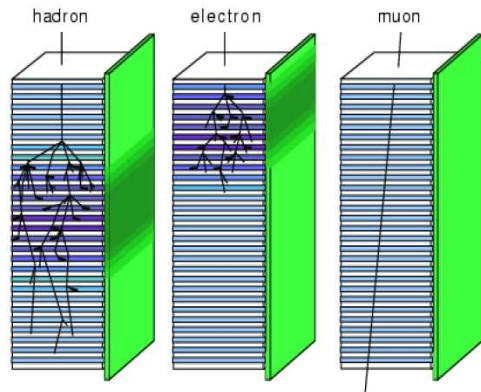
Figure 7.3: Typical shower profiles in the calorimeter for different types of particles.

A typical muon signature in the ZEUS detector has the following characteristics:

- **A track reconstructed in the tracking system.**
  Muons are charged particles, they therefore yield tracks in the ZEUS inner tracking detectors, MVD, CTD, STT and FRTD. These tracks are bent in the ZEUS solenoid field and from this the muon momentum and the direction can be determined.

- **Vertex association of the track.**
  Muons from beauty decays are produced very close to the interaction point, and thus in the HERA I period they are associated to the primary vertex within the resolution of the CTD. For the HERA II period, where the micro vertex detector was installed, the muon tracks may be associated to a secondary vertex.

- **MIP signature in the calorimeter.**
  For muons the energy loss by ionisation in matter is very low, typically about $1\,\mathrm{GeV/m}$ in uranium. They can therefore reach the muon chambers. In contrast particles like electrons, pions and kaons are stopped in the calorimeter.

- **Hits in the muon chambers.**
  Due to the high penetration power muons can reach the BAC and the inner/outer muon chambers.

- **Nonisolation**
  Muons from heavy flavour decays have typically nonisolated tracks, they are accompanied by the particles from the decay of the heavy hadron, which were clustered into a jet.

7.2.2   General muon reconstruction with $^{\mathrm{G}}$Muon

Different algorithms are available for muon reconstruction at ZEUS. Most of them are using the B/RMUON or FMUON chambers (mainly BREMAT and MPMATCH), some use the BAC (i.e. MUBAC) and others only the calorimeter information (MV). The general muon finder $^{\mathrm{G}}$Muon [120] is based on a combination of the signatures from the different muon finders available in ZEUS to obtain a single muon object. It establishes links between these finders and assigns a global *muon quality*.

In the following, the main characteristics of the different muon reconstruction algorithms will be described.

- MUONFIND
  This algorithm [120] performs a simple matching of CTD tracks with CAL cone islands compatible with a MIP signature. It is used for CTD tracks with high momentum, i.e. $p_T^\mu > 2\,\mathrm{GeV}$.

- MV
  This finder [121] uses calorimeter information to find and classify energy clusters by their shape and orientation using a neural network approach, called phase space probability function [122]. The function outputs a probability for the selected cluster to have been induced by a minimally ionising particle, such as a muon, coming from the event vertex. It also matches CTD tracks with the MIP CAL cone islands.

- GLOMU
  The GLOMU [123] algorithm provides a simple match, based on distance and angular cuts, between a CTD track and inner/outer B/RMUON segments. It also provides a match to MIP clusters.

- BREMAT
  This algorithm [124] performs a match between tracks extrapolated from the CTD into the inner muon chambers and reconstructs muon segments. To match the CTD to the muon chamber tracks, the CTD track is extrapolated to the inner muon chamber plane. The possible scattering process of the muon passing all the material on the way to the muon chambers, as well as the variation of the magnetic field along the trajectory is simulated using the GEANE [125] package and is also included in the error matrix of the extrapolated CTD track. For matching with an inner muon chamber track, the extrapolated CTD track is then matched in position and angle in two projections. If the muon chamber track segment spans the inner and outer chambers, one can derive an additional muon momentum estimate from the two muon chamber tracks alone. This algorithm is recommended for non-isolated muon studies.

- MUBAC
  The MUBAC [120] finder reconstructs muon segments from BAC information. Rather precise position information of the order of $1\,cm$ in the $r\phi$ plane in the barrel BAC and zr plane in the forward and rear BAC is obtained from the strip information. The other position is constrained within a resolution of 0.15 to 2 m, depending on the position of the BAC and whether the information comes from the analog wires only or from the pad readout. The distance of closest approach method is used to match the tracks from the CTD to the reconstructed BAC muon segments.

- MCTS
  In the MCTS algorithm [120] the segments are obtained by combining a simplified curved spline fit in the FMUON system with a straight line fit trough the CAL and the CTD towards the primary vertex, including an estimation of the energy loss. This provides a rudimentary momentum estimate at the vertex based on FMUON information only.

- MPMATCH
  The MPMATCH [126] algorithm is one of the most sophisticated algorithms available. It matches FMUON segments with CTD primary vertex tracks using a Kalman filter technique. As in BREMAT the CTD tracks are extrapolated using GEANE. The muon momentum is determined from the combined track measurement. CAL or BAC information is not used within MPMATCH.

- MUFO
  This algorithm [120] is very similar to MPMATCH. It has two main substreams.

  - Using a Kalman filter fit, it makes the match between an FMUON segment, a CTD track and the primary vertex. This is essentially identical to MPMATCH and yields almost the same muon candidates.

  - Match between a FMUON segment and the primary vertex, without a CTD track. This is interesting in particular for the very forward region in which a CTD track may not be reconstructed.

The [G]Muon algorithm combines all the finders mentioned above. The advantages of such combination relay on the fact that whereas each separate finder might be limited to reconstruct only a certain type of muon candidates (e.g. isolated muons, high or low p_T muons, forward muons, etc.) and have limited geometrical coverage, the combination of all finders drastically reduces these limitations, increasing therefore the signal to background ratio and the number of muon candidates.

The quality assigned to each candidate range on a scale from 0 (lowest quality) to 6 (highest quality). High quality means that a high signal to background ratio is to be expected. Here *signal* means semileptonic muons from beauty decays, while *background* refers to all other muon candidates in a given event. For lower quality the signal to background ratio decreases depending on the sample used. The signal to background dependence on the muon quality was estimated using an inclusive $b\bar{b}$ and a light flavour Monte Carlo samples.

The tuning of [G]Muon does not include background from cosmics or from noise in the forward detector. Therefore muon quality modification and MC muon efficiency correction routines have been implemented in addition. Detailed information on these issues can be found in [120].

For beauty quark analyses muons with quality 4 or higher are best suited. Examples of finder combinations and the resulting [G]Muon quality are shown in Table 7.2. The cut values for the different finders are taken from analyses using these finders separately.

quality	finders used	CTD match	match prob. or DCA	vtx. ass.	MIP prob.	p^μ or η^μ
6	BREMAT	yes	> 0.01	yes	-	-
	MPMATCH	yes	> 0.05	-	-	-
	MPMATCH/MUFO+MV	yes	$> 0.01, < 0.05$	-	> 0.6	$p > 1\,\mathrm{GeV}$
5	BREMAT+MV	yes	> 0.01	yes	> 0.6	$|\eta| > 0.6$
	MUBAC+MV	yes	-	yes	> 0.6	$|\eta| > 0.6$
	MUBAC+BREMAT+MV	yes	> 0.01	yes	> 0.6	$|\eta| > 0.6$
	MUBAC+BREMAT+MV	yes	> 0.01	no	> 0.6	-
	MPMATCH or MUFO	yes	$> 0.01, < 0.05$	-	-	-
	MUFO good vtx	no	-	yes	-	-
4	BREMAT	yes	> 0.01	yes	-	-
	MUBAC	yes	$< 50\,\mathrm{cm}$	yes	-	-
	MUBAC+MV	yes	$< 120\,\mathrm{cm}$	yes	> 0.6	$|\eta| > 0.6$
	MUBAC+ MIP	yes	$< 120\,\mathrm{cm}$	-	impl.	$p_T > 2\,\mathrm{GeV}$
	MUFO other vtx	no	-	yes	-	-
	MCTS+MV	no	-	no	> 0.6	-

Table 7.2: Muon quality assignments in $^\mathrm{G}$Muon for quality ≥ 4.

7.3   Electron Identification

Most particle identification techniques at ZEUS are based on ionisation measurement and on the different showering properties of hadrons and electrons in the absorber material of the detector. For electron identification usually the most important instruments are the central tracking detector and the calorimeter. Nevertheless, at ZEUS the aim at short term is to create a general electron finder, similar and compatible with $^\mathrm{G}$Muon, which will combine the different electron identification algorithms using the information coming not only from the central tracker and the calorimeter but also from other detectors like the hadron-electron separator and the forward detector. This part of the work is a first step in that direction and is one of the main topics of this thesis. Here the base framework of such a general electron finder, $^\mathrm{G}$Elec, is developed.

7.3.1   Electron signature

Electrons may leave very distinctive tracks in the central detectors, corresponding to an energy loss by ionisation of about 1.4 MIPs. Then, they typically deposit all their energy in the electromagnetic part of the uranium calorimeter in form of small and compact showers, as shown in Figure 7.3. Electrons from semileptonic decays have typically a signature with the following characteristics:

- **A track reconstructed in the tracking system.**
  As in the case of muons, most of the electrons leave tracks in the central tracking detectors, from where the electron momentum and direction can be determined.

- **Vertex association of the track.**
  Electrons from beauty decays may be associated to the primary vertex in the HERA I period and for the HERA II period to a secondary vertex.

- **1.4 MIPs signature in the tracking system.**
  For electrons the energy loss by ionisation in matter corresponds to a value of about 1.4.

- **Electromagnetic energy in the calorimeter.**
  The shower produced by the electron is almost fully contained in the electromagnetic part of the calorimeter. For hadrons, in contrast, there are also energy deposits in the hadronic part of the calorimeter.

- **Nonisolation**
  Electrons from heavy flavour decays have typically nonisolated tracks, they are accompanied by the particles from the decay of the heavy hadron, which were clustered into a jet.

7.3.2 General electron reconstruction with $^{\mathrm{G}}$Elec

Two main electron finders are available at ZEUS: SINISTRA and EM. They were mainly designed to tag the scattered electron of the hard interaction and are not well suited to tag e.g. electrons from semileptonic decays. Therefore in this first part these electron finders were not yet integrated into the $^{\mathrm{G}}$Elec code. Nevertheless, a space is left for them into the code for later implementation. A brief description of them follows.

- SINISTRA
  This algorithm [127] uses calorimeter information only, grouping calorimeter energy deposits into islands, where each island is an electron candidate. It uses a neural net to decide over the quality of the electron candidate, and it is mainly trained to tag electrons in the RCAL.

- EM
  This finder [128] uses information from the central tracker and the calorimeter. First, CAL cells are clustered into islands and then a match to the track in the central tracking detector is done. If no track is found then the island is a trackless candidate.

The $^{\mathrm{G}}$Elec finder is not restricted to tag preferentially the scattered electron, as was the case of SINISTRA and EM, it will be optimised to tag electrons from semileptonic decays. The $^{\mathrm{G}}$Elec algorithm is implemented in C++, in an object oriented framework. It is based on two types of discriminating variables, the ones related to the track and the ones related to the shape of the energy deposit in the calorimeter, as will be explained below. All the needed information is obtained from the energy flow objects (EFOs) which were described in Section 7.1.3.

7.3.3 Discriminating variables in $^{\mathrm{G}}$Elec

The $^{\mathrm{G}}$Elec finder makes the selection of electron candidates using the information from the EFOs. A pre-selection at Ntuple-generation level is done searching for EFOs with one reconstructed track and one cluster of energy deposited in the calorimeter (so called, EFOs type 1). The corresponding relevant information is stored in a separate common block in the Ntuple. This common block contains the variables described in Table 7.3. Such a separate common block has the advantage that the size of the Ntuple is reduced because only the relevant information is stored. Avoiding e.g. the need to save the whole islands information block, which is one of the largest in a standard Ntuple. There is also an improvement in run time efficiency at analysis level because, for example, it is not needed to loop over the whole tracking block to find the track corresponding to the EFO, this was done at Ntuple-generation level, and using the pointer to the tracking block one has access to this and additional information.

Variable	Description
TCnzufos	number of zufos stored
TCinxTrk	pointer to the tracking block
TCqTrk	charge of the matched track
TCpTrk	momentum of the track
TCdca	distance of closest approach between track and the CAL cluster
TCNrcIsl	number of cells of the island
TCrIsl	radius of the island

Table 7.3: Variables in the $^{\mathrm{G}}$Elec common block of an Ntuple.

At analysis level, the $^{\mathrm{G}}$Elec finder uses the following estimators on the track:

- **Primary vertex track**
  As for the time being $^{\mathrm{G}}$Elec's design is limited to HERA I data, in order to reject background coming from places far away from the interaction point (e.g. photon conversions in the dead material of the detector) a track from the primary vertex within the resolution of the central tracking detector is required.

- **Minimum momentum of the track**
  As hadronic and electronic showers become nearly indistinguishable below 1 GeV and the only non shower based technique, dE/dx in the central tracking detector, also has fundamental difficulties to separate hadrons and electrons below 1 GeV a lower cut on the momentum of the track of 1.2 GeV is introduced.
  $$p_{\mathrm{track}} \geq 1.2\,\mathrm{GeV}$$

- **Energy loss by ionisation**
  When electrons lose their energy in the central tracker, a typical dE/dx measurement of ~ 1.4 MIPs is expected, as displayed in Figure 7.4. The measurement of the specific energy loss due to ionisation, dE/dx, in the central tracker is one of the most important tools for particle identification. Recently there was a major improvement in the dE/dx measurement with the ZEUS CTD [10]. In that work twelve detector-related influences affecting the dE/dx measurement have been identified, separately studied and parametrised. A sophisticated iterative process has been developed to correct for those effects, obtaining an universal parametrisation of the detector specific Bethe-Bloch curve valid for all particles. This yields the best achievable prediction for the single track dE/dx resolution. Here, this improved dE/dx measurement

method will be applied. Its discrimination power will be compared to the set of variables related to the shape of calorimeter energy cluster for the case of the invariant mass reconstruction of the J/ψ meson, as will be shown in the next section.
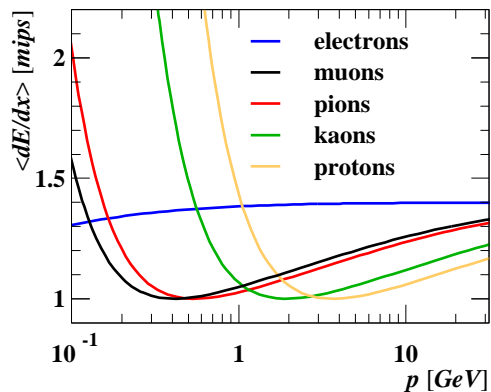
Figure 7.4: Bethe-Bloch prediction for different particle types. From [129].

The following estimators deal with the shape of the energy deposit in the calorimeter:

- **Electromagnetic energy fraction in the calorimeter**
  As already mentioned above, electrons deposit almost all their energy in the electromagnetic part of the calorimeter. Therefore, the sum of the energy of all the cells in the electromagnetic section should be larger than 90% of the whole energy of the cluster:

$$\text{EMC fraction} = \frac{\Sigma_{\text{EMC cells}} E_i}{E_{\text{CAL cluster}}} \geq 0.9 \qquad (7.2)$$

- **Distance of closest approach track-cluster**
  The track reconstructed in the central tracker matched to an energy deposit in the calorimeter was required to have a distance of closest approach of less than 15 cm.

$$dca \leq 15\,\text{cm}$$

- **Number of cells per island**
  Isolated electrons spread their showers in very few cells of the calorimeter. In an extreme case, an electron may hit the corner of four neighbouring EMC cells and leakage some energy in a couple of HAC cells. Non-isolated electrons from

heavy flavour decays accompanied by hadronic activity have bigger showers but, when the electron is not almost aligned to the axis of the jet, it is possible to reconstruct a smaller cluster. Therefore the required number of cells in the island was set to be not more than 8.

$$nrcisl \leq 8$$

- **Radius of the island**
  Here the radius of the island is calculated from the centre of the most energetic cell. Considering that the electromagnetic cells are 5×20 cm big, as is shown in Figure 7.2, the radius of the energy deposit of an electron candidate was selected to be smaller than 30 cm.

$$risl \leq 30\,\text{cm}$$

- **Energy-momentum consistency**
  The ratio between the energy deposited in the calorimeter and the momentum of the track, E/p, is typically used as discriminating variable. Here, an analogous quantity, the difference of the energy and the momentum normalised to the energy $(E - p)/E$, will be used instead. The $(E - p)/E$ measurement can be deteriorated when a particle is not properly isolated and showers from several particles overlap in the calorimeter cluster. The energy-momentum consistency values for an electron candidate were set to:

$$-1.4 < (E - p)/E < 0.175$$

The Figure 7.5 shows the $^{\text{G}}$Elec discriminating variables applied to the shape of the energy cluster in the calorimeter which are not typically used in other analysis. The sample used to produce those plots was a Monte Carlo $b\bar{b}$ sample from direct beauty processes generated using PYTHIA, for the HERA I running period (99p-00p), with 23788 events.
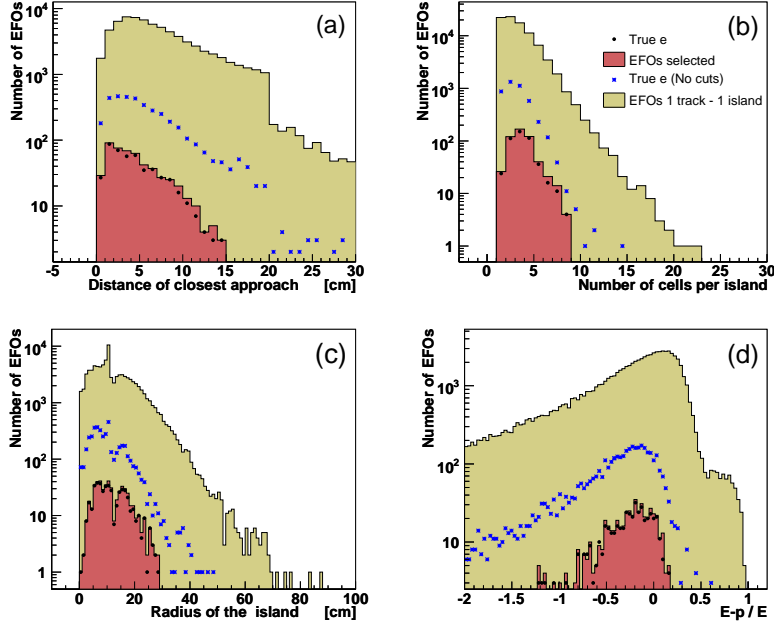
Figure 7.5: Some discriminating variables used in $^{\mathrm{G}}$Elec. The clear shadowed histograms show the EFOs with one reconstructed track matched to an energy cluster in the calorimeter, the stars show the corresponding true electrons. The dark shadowed histograms show the selected EFOs which correspond to electron candidates chosen by $^{\mathrm{G}}$Elec. The full dots are the true electrons. (a)Distance of closest approach between the track and the calorimeter island. (b)Number of cells per island. (c)Radius of the island. (d)$(E-p)/E$ variable.

7.4 $J/\psi \rightarrow e^+e^-$ reconstruction

To test the $^{\mathrm{G}}$Elec identification method, events with elastically produced J/ψ decaying into an electron and a positron were selected. The branching ratio for this process is: $\mathrm{BR}(J/\psi \rightarrow e^+e^-) = (5.93\pm0.10)\%$. The selection criteria for J/ψ events is based on the reconstruction of the invariant mass of the J/ψ, which corresponds to a value of:

$$m(J/\psi) = 3.096 \pm 0.04 \, \mathrm{GeV},$$

assigning the right sign combination of two primary vertex tracks. The scattered electron is excluded from this study. The main trigger used for this selection was an elastic $J/\psi \rightarrow e^+e^-$ trigger (HFL06) in which the EMC fraction is more than 0.9, for two primary vertex tracks with a reconstructed invariant mass of $m_{ee} > 1.5 \, \mathrm{GeV}$.

Electron candidates at ZEUS are typically selected in other analysis using the following cuts: the requirement of primary vertex tracks with the corresponding track matched to one energy cluster in the calorimeter (EFOs type 1), the electromagnetic energy in the calorimeter (EMC fraction ≥ 0.9), minimum momentum of the track ($p_{\mathrm{track}} \geq 1.2 \, \mathrm{GeV}$), and E/p cut which is almost equivalent to the $^{\mathrm{G}}$Elec energy-momentum consistency cut $(E-p)/E$. These cuts are defined here as *basic cuts*.

In order to compare the discrimination power of the other variables used in $^{\mathrm{G}}$Elec, the recently improved dE/dx measurement (see [10]) with respect to the calorimeter based discriminating variables (dca, $risl$ and $nrcisl$), two additional samples were produced. A pre-selection was applied in both cases using the basic cuts quoted above. To acquire more statistics some of the $^{\mathrm{G}}$Elec cuts were widened. The invariant mass of the J/ψ was reconstructed in each case. The different samples and the cuts used are summarised in Table 7.4.

$J/\psi \rightarrow e^+e^-$		
Test sample	HERA I data (99e), $\mathcal{L} = 765.32 \, \mathrm{nb}^{-1}$	
Event cuts	at least two PV tracks matched to one energy cluster each $2.0 \, \mathrm{GeV} \leq$ invariant mass $m_{ee} \leq 5.0 \, \mathrm{GeV}$	
Basic cuts	on the track on the island	$p_{\mathrm{track}} \geq 1.2 \, \mathrm{GeV}$ EMC fraction ≥ 0.9 $-1.4 < (E-p)/E < 0.3$
Selection A	Basic cuts + dE/dx	$1.2 \leq dE/dx \leq 1.6$
Selection B	Basic cuts + CAL variables	$dca \leq 15 \, \mathrm{cm}$, $risl \leq 30 \, \mathrm{cm}$, $nrcisl \leq 6$
Selection C		All cuts

Table 7.4: Selection criteria for the elastic $J/\psi \rightarrow e^+e^-$ events.

The Figure 7.6 shows the invariant mass distributions obtained from Selections A and B. The Table 7.5 shows the signal to background ratio obtained in each case.
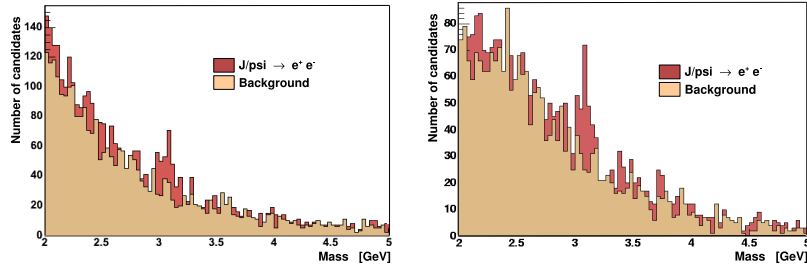
Figure 7.6: Comparison of the invariant mass reconstruction for the process $J/\psi \rightarrow e^+e^-$. The dark histogram shows the right charge combinations and the clear histogram shows the wrong charge combinations. The left plot shows the J/ψ signal extracted from the selection A (basic cuts plus dE/dx). The right plot shows the signal obtained from the selection B (basic cuts plus the cuts on the calorimeter cluster shape).

Selection	Number of events		S/B ratio
A	Signal	384	1.79
	Background	214	
B	Signal	343	1.64
	Background	209	

Table 7.5: Number of events and signal to background ration in the selections A and B.

As one can see from Figure 7.6 and Table 7.5 the dE/dx measurement and the calorimeter variables have a comparable discrimination power. Nevertheless separately they do not have good resolution of the J/ψ signal. The Figure 7.7 shows the J/ψ signal obtained from Selection C, using all the cuts as they are implemented in $^{\rm G}$Elec. The $^{\rm G}$Elec method shows a clear improvement over the application of the basic cuts, the dE/dx and the calorimeter cuts separately. A very clear signal is obtained with almost no combinatorial background. Another advantage is that no further cuts on the event or the leptons were needed, e.g. multiplicity cuts on the number of energy flow objects present in the event.
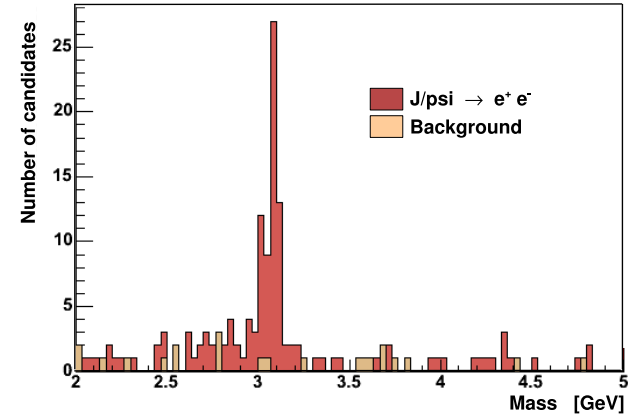
Figure 7.7: Invariant mass reconstruction for the process $J/\psi \rightarrow e^+e^-$ using $^{\rm G}$Elec. The dark histogram shows the right charge combinations and the clear histogram shows the wrong charge combinations.

7.5   Test of $^{\rm G}$Elec on Monte Carlo samples

Two additional Monte Carlo samples were generated to include the new variables in the Ntuples and test the $^{\rm G}$Elec finder. The first one was a Monte Carlo sample of the elastic $J/\psi \rightarrow e^+e^-$ process. This sample was generated using GRAPE-dilepton Monte Carlo with the specifications listed in the Table 7.6. The same event and lepton cuts used in Selection C (Table 7.4) were used in this case.

$J/\psi \rightarrow e^+e^-$ Monte Carlo	
Test sample	HERA I MC (97p), 20000 events
Generator	GRAPE-Dilepton
Process	DIS $J/\psi \rightarrow e^+e^-$ (elastic)
Kin. range	$Q^2 > 1\,\mathrm{GeV}^2$ and $10 < W < 220\,\mathrm{GeV}$

Table 7.6: Generation criteria for the $J/\psi \rightarrow e^+e^-$ Monte Carlo.

The Figure 7.8 shows the invariant mass distribution obtained. As one can see from the Figure, the reconstruction of the J/ψ signal is very good. The peak is placed at the right position around the mass value of $m(J/\psi) = 3.096\,\mathrm{GeV}$ and the bremsstrahlung tail to the left is also visible.
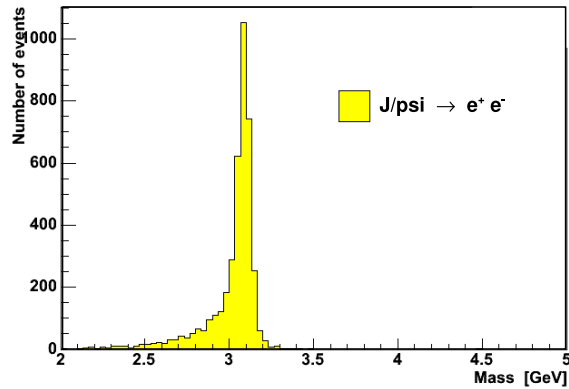
Figure 7.8: Invariant mass reconstruction for the process $J/\psi \to e^+e^-$ using $^{\mathrm{G}}$Elec on a Monte Carlo sample.

The second Monte Carlo sample was a $b\bar{b}$ sample from direct beauty processes with the specifications listed in the Table 7.7. In this sample also e^+e^- pairs were selected using the same cuts as in Selection C (Table 7.4).

$b\bar{b}$ direct Monte Carlo	
Test sample	HERA I MC (99p-00p), $\mathcal{L} = 368.5$ pb^{-1}
Generator	PYTHIA 6.203
Process	$\gamma g \to b\bar{b}$
Fragmentation	Peterson ($\epsilon = 0.0041$)
PDF p	CTEQ4L
Kin. range	no cuts

Table 7.7: Generation criteria for the $b\bar{b}$ direct Monte Carlo.

The Figure 7.9 shows the invariant mass reconstruction in this case. There, it is possible to distinguish a peak coming from the process $b\bar{b} \to J/\psi \to e^+e^-$ which is slightly above the combinatorial background. Due to the low branching ratio for this kind of events the background is considerable. Nevertheless, the presence of the J/ψ signal is a good indication that the $^{\mathrm{G}}$Elec method works, because only the $^{\mathrm{G}}$Elec selection cuts were applied in the selection of the electron candidates. Additional cleaning cuts may be applied later to improve the resolution, as will be shown in the next section.
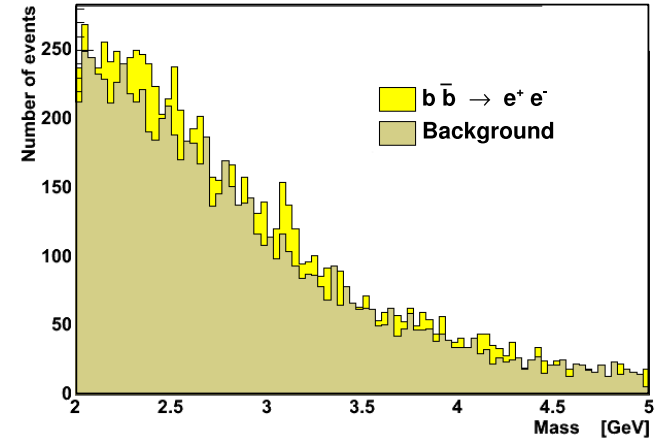
Figure 7.9: Invariant mass reconstruction for the process $b\bar{b} \to J/\psi \to e^+e^-$ using $^{\mathrm{G}}$Elec on a $b\bar{b}$ Monte Carlo sample.

7.6   Dilepton identification of beauty

In this section a new ZEUS heavy flavour analysis will be introduced. The $ep \to b\bar{b}X \to e\mu X'$ channel. For this analysis, the method used in the dimuon analysis [52] is followed and dilepton mass distributions for the like- and unlike-sign lepton combinations are obtained for a HERA I data sample. However, due to time constraints from the author of this work, proper background estimation using Monte Carlo models and the calculation of the cross sections for the whole HERA data are left for a further stage of the analysis.

The new $^{\mathrm{G}}$Elec finder developed in this thesis will be used now to tag events were beauty quarks are present. These will be selected tagging the leptons which result from the semileptonic decays of the heavy quarks. The corresponding branching ratios for the decay of beauty mesons into leptons are displayed in Table 7.8.

b meson decay	$e^+\nu_e$	$\mu^+\nu_\mu$	$\tau^+\nu_\tau$
BR [%]	10.9	11.0	2.5

Table 7.8: Beauty quark branching ratios in percentage.

Muon selection is done using $^{\mathrm{G}}$Muon and electron selection using $^{\mathrm{G}}$Elec. Any combination of electrons and/or muons is therefore possible. From all possible dilepton combinations the dimuon channel, $ep \to b\bar{b}X \to \mu^+\mu^- X'$, was already extensively studied using $^{\mathrm{G}}$Muon only [52, 96]. The electron+muon channel was not yet studied at ZEUS and this channel should provide better cross-section measurements in the low p_T^b region in comparison with previous analyses because the electrons allow to further extend the phase space of the measurements close to the kinematic threshold.

The principle of the measurement is based on the selection of two main event classes which contribute to the beauty signal to be measured. The first kind are events in which the two leptons originate from the same parent B hadron yielding unlike-sign particle combinations produced in the same event hemisphere, constrained to the lepton invariant mass reconstruction of $m_{e\mu} < 4\,\mathrm{GeV}$ (which corresponds to the partially reconstructed B-hadron mass considering the energy that the neutrino takes away). In the second kind of events, the leptons originate from different beauty quarks from a $b\bar{b}$ pair. This events yield both like- and unlike-sign lepton combinations. They may come from the decay of the primary beauty quark, or from the secondary charm quark from a decay chain. The charge combination also depends if a $B^0\overline{B^0}$ mixing has occurred. Leptons produced in this way tend to be present in different event hemispheres and have larger dilepton masses.

As already established in [52] for the dimuon case, an important background contribution arises from charm-pair production, were both charm quarks decay semileptonically. In similar way in this case the charm production yields unlike-sign electron-muon pairs and the two leptons are produced predominantly in opposite hemispheres. Another source of background is the, so called, light flavour background. It consists of both like- and unlike-sign combinations where at least one of the leptons is fake, i.e. originates from kaon or pion decays, or a hadron is misidentified as a lepton. Another measure taken in that analysis to separate signal and background was a muon non-isolation requirement, because as already explained before, muons from semileptonic decays are accompanied by hadronic activity.

The method used in the dimuon analysis relies on the fact that the light flavour background contributes almost equally to the like- and unlike-sign dimuon distributions, and therefore knowing all the other background contributions the difference between unlike and like-sign distributions can be used to measure the beauty contribution and extract the cross sections.

7.6.1 Data set

The data used in this analysis is a sample of ZEUS HERA I data. This dataset is reliable due to the well functioning and well understood detector components. A large data sample with consistent set of trigger configurations and stable detector components (especially tracking, calorimetry and muon chambers) of ZEUS pre-upgrade data has been recorded from 1996 to 2000.

A pre-selection of the data sample is applied using the, so called, ZEUS *take* routines. These contain veto flags for certain detector components and runs, which are set if a component was malfunctioning during a given run. The veto flags are the output of data quality monitoring jobs performed by the corresponding experts of the components, as explained in Chapter 3. The main ZEUS data quality flag (EVTAKE) corresponds to good data quality of main components: the central tracking detector, calorimeter, trigger chain and luminosity measurement. Additionally, a similar run-by-run selection based on the muon chamber quality has been applied, called MBTAKE for the barrel and rear muon chambers and FMUTAKE for the forward muon spectrometer. A small sample was excluded from the selection, it consists of a period running with a shifted vertex (+0.8 m) in the year 2000 corresponding to an integrated luminosity of 0.815 pb^{-1}. An overview of the different running periods and the corresponding luminosity collected is displayed in Table 7.9.

Data set				
Running period	Interaction	$\sqrt{s}$ [GeV]	Luminosity [pb^{-1}] after EVTAKE	Luminosity [pb^{-1}] after EVTAKE+FMU/MBTAKE
1996-1997	e^+p	300	38.62	38.01
1998-1999	e^-p	318	16.68	15.89
1999-2000	e^+p	318	65.88	60.17
Total			121.2 ± 3.0	114.0 ± 2.9

Table 7.9: ZEUS data set collected from 1996 to 2000.

7.6.2 Trigger selection

The triggers slots used in this analysis were chosen on the third level trigger of the ZEUS trigger chain as explained in 2.8. The selected triggers are mainly focused in the identification of a muon candidate in the event, but for a future comparison to Monte Carlo models (important also for background studies) the selected trigger slots include triggers on charm events, dijet events, generic deep inelastic scattering events, as well as combination of the given trigger types. A summary of the triggers used is shown in Table 7.10. Detailed trigger slot definitions can be found in [52].

Trigger selection		
Property	Name	Main cuts
pure muon triggers		
Forward muon	MUO1/2/4	$\eta^\mu > 1.3$
Barrel/Rear muon	MUO3	$\eta^\mu < 1.3$
outer B/R muon	EXO11/12	outer B/R μ by GLOMU, cosmic μ rejection
hadronic triggers		
Dijet + muon	HFL1	$\eta^\mu < 1.3$, 2 jets with $E_T^{jet} > 3.5\,$GeV, $|\eta^{jet}| < 2.5$
Dijet	HPP14	2 jets with $E_T^{jet} > 4(4.5)\,$GeV, $|\eta^{jet}| < 2.5$
Generic charm	HFL10/11	D^* in $K\pi\pi$ channel, $p_T(D^*) > 1.8\,$GeV
DIS triggers		
DIS	DIS3	$E^e > 4\,$GeV, $30 < E - p_z < 100\,$GeV
DIS + muon	DIS27	$E^e > 7\,$GeV, $\eta^\mu < 1.3$

Table 7.10: TLT trigger selection applied to the reconstructed information.

7.6.3   Electron-muon selection

- **Event selection**
  The dilepton events in this analysis were selected by requiring the presence of a muon found by ^{G}Muon using the same cuts applied on the muons in [52], the main requirement was the transverse momenta of the muon as:

$$p_T^\mu \geq \begin{cases} 1.5\,\text{GeV} & \text{for muons with quality} = 4, \\ 0.75\,\text{GeV} & \text{for muons with quality} \geq 5, \end{cases}$$

depending on the muon reconstruction quality defined in Table 7.2.

The presence of an electron in the event was also required, which was found by ^{G}Elec with transverse momenta of

$$p_T^e \geq 1.2\,\text{GeV}.$$

Selection cuts related to calorimeter quantities were also applied as implemented in ^{G}Elec (See 7.3.2).

In order to cut on the partially reconstructed mass of the two beauty quarks present in the event, considering that neutrinos escape detection, the transverse energy reconstructed in the calorimeter E_T^{cal} was restricted to have a value of:

$$E_T^{cal} \geq 8\,\text{GeV}.$$

The transverse energy was corrected by subtracting the transverse energy in a cone of 10° around the forward beam pipe (to subtract the particles coming

from the proton remnant or final state colour connection) as well as subtracting the energy of the scattered DIS electron, in case it was detected:

$$E_T^{cal} = \begin{cases} E_T^{cal} - E_T^{cal}\mid_{\text{in 10° forward cone}} & \text{for } \gamma p \text{ events,} \\ E_T^{cal} - E_T^{cal}\mid_{\text{in 10° forward cone}} - E_T^{electron} & \text{if a DIS electron was found.} \end{cases}$$

To reject cosmic background the cuts applied were a cut on the difference in ϕ angle of the dilepton (considering that the two leptons are of the same species):

$$\delta\phi \equiv \mid\mid \phi^{\text{lepton 1}} - \phi^{\text{lepton 2}} \mid -\pi \mid < \pi/200$$

thus perfectly back-to-back pairs of the same kind of leptons are cut out. A similar cut was also done using the difference in the θ angle:

$$\delta\theta \equiv \mid \theta^{\text{lepton 1}} - (\pi - \theta^{\text{lepton 2}}) \mid < \pi/200$$

To reject light flavour background a cut on the dilepton p_T asymmetry was done:

$$\mid p_T^{\text{lepton 1}} - p_T^{\text{lepton 2}} \mid / \mid p_T^{\text{lepton 1}} + p_T^{\text{lepton 2}} \mid \leq 0.7.$$

The cuts used are summarised in Table 7.11.

$ep \rightarrow b\bar{b}X \rightarrow e\mu X'$	
Test sample	HERA I data , $\mathcal{L} = 114$ pb^{-1}
Event cuts	number of electrons found by ^{G}Elec $N_e \geq 1$ number of muons found by ^{G}Muon $N_\mu \geq 1$ 1.5 GeV $\leq$ dilepton invariant mass ≤ 15 GeV E_T^{cal} (corrected) ≥ 8 GeV.
Electron cuts	$p_{\text{track}} \geq 1.2$ GeV, $1.2 \leq dE/dx \leq 1.6$ EMC fraction ≥ 0.9 $dca \leq 15$ cm, $risl \leq 30$ cm, $nrcisl \leq 6$ $-1.4 < (E-p)/E < 0.3$
Muon cuts	$p_T^\mu \geq 1.5$ GeV for muons with quality $= 4$ $p_T^\mu \geq 0.75$ GeV for muons with quality ≥ 5
Background cuts	to reject cosmics: $\delta\phi \equiv \mid\mid \phi^{\text{lepton 1}} - \phi^{\text{lepton 2}} \mid -\pi \mid < \pi/200$ or $\delta\theta \equiv \mid \theta^{\text{lepton 1}} - (\pi - \theta^{\text{lepton 2}}) \mid < \pi/200$ to reject combinatorial and light-flavour background: $m^{e\mu} > 1.5$ GeV and $\mid p_T^{\text{lepton 1}} - p_T^{\text{lepton 2}} \mid / \mid p_T^{\text{lepton 1}} + p_T^{\text{lepton 2}} \mid \leq 0.7$

Table 7.11: Selection criteria for the selection of $b\bar{b} \rightarrow e\mu$ events.

- **Dilepton mass and charge separation**
  To discriminate between the leptons produced directly from the decay of different beauty quarks and those produced in a cascade decay of the same beauty quark, invariant mass distributions were produced. The distributions are separated according to the dilepton invariant mass in two sets. First, low-dilepton mass range with

$$m_{e\mu} < 4\,\mathrm{GeV},$$

  where the pair of leptons come predominantly from the same beauty quark. The second sample a high-dilepton mass range with

$$m_{e\mu} \geq 4\,\mathrm{GeV},$$

  which contains dileptons originated from the decay of different b quarks. Both samples are additionally separated by the charge of the lepton into like- and unlike-sign dilepton events. The mass distributions in the low and high mass range, as well as the like- and unlike-sign lepton charge combination are displayed in the Figure 7.10.

7.6.4   Outlook

At this stage of the analysis one can conclude that the shape of the invariant mass distributions in Figure 7.10 look reasonable and the amount of events in each one is as expected, using as a reference the distributions obtained in the dimuon analysis [52], shown in Figure 5.8, giving an indication that the analysis is going along the right path.

The next steps in the development of the $ep \to b\bar{b}X \to e\mu X'$ analysis consist in the separation of the data in isolated and non-isolated leptons subsamples, and the comparison to Monte Carlo models to take into account the contributions from the different processes, and in this way estimate the background and extract the cross sections. The analysis can be extended as well to the full HERA data sample, which is now available. Taking advantage of the upgrades of the accelerator and the ZEUS experiment in the HERA II running period. This would allow a considerably reduction of the experimental uncertainties, providing an accurate extraction of the total cross sections, and a reliable measurement down to very low values of the p_T^b spectra. Gaining with this a further insight into the understanding of QCD processes. On the other hand, the comparison to next-to-leading order cross section predictions would be straight forward because the FMNR⊗Pythia interface is already available.
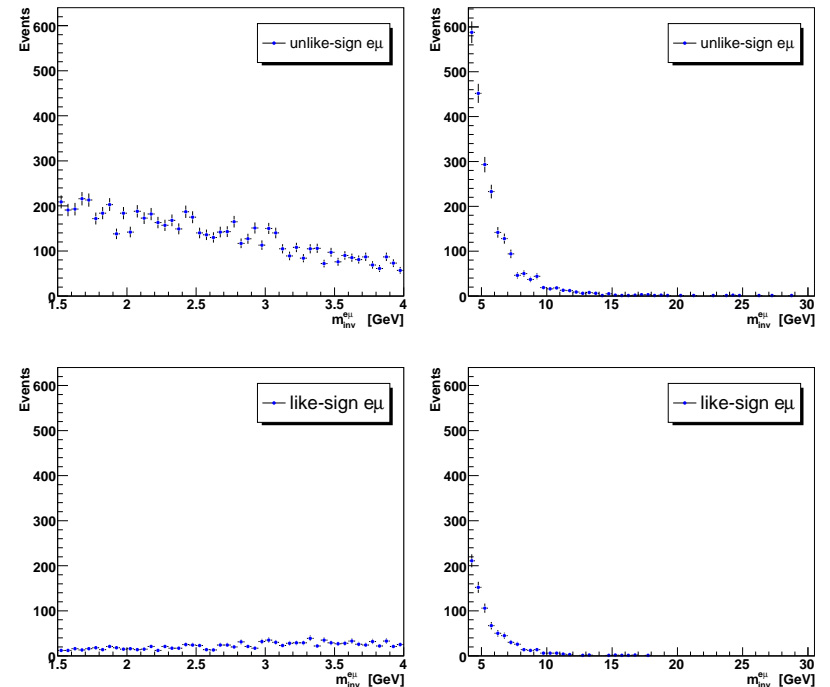
Figure 7.10: Dilepton invariant mass distributions of unlike-sign electron-muon pairs in the (a) low mass and (b) high mass subsamples, as well as like-sign electron-muon pairs in (c) the low and (d) high mass subsamples.

Chapter 8

Summary and Conclusions

This thesis work is among the first to be presented after the completion of the HERA accelerator program. The members of the different experiments did an extremely big effort to maintain, upgrade and keep running the detectors in optimal conditions during so many years of data taking in order to acquire the best possible data. This thesis work was done in the context of the ZEUS experiment, and one example of the work related to the maintenance and data quality monitoring of one of the most important components of the detector, the uranium calorimeter, was described here.

Cross sections for heavy quark production from the ep collisions at HERA are being measured with high precision. This includes channels with complex final states for which next-to-leading order QCD predictions are not easily obtained from simple extensions to parton-level calculations. An algorithm capable to make such calculations for HERA data was not available. Similar algorithms, e.g. MC@NLO are fully implemented only for hadron colliders. The need to compare the data from the recently finished heavy flavour ZEUS analyses ($ep \to b\bar{b}X \to D^*\mu X'$, $\mu^+\mu^- X'$, etc., with complex cuts on these final state particles) to theoretical predictions caused the development of a FMNR⊗Pythia interface. This interface allows such next-to-leading order QCD predictions to be obtained for the photoproduction regime.

The FMNR⊗Pythia interface calculates point-like and hadronic parton-level processes using the FMNR program with an extension, the RedStat routines, which transform the FMNR program into a Monte Carlo-like event generator. The RedStat routines preserve the next-to-leading order accuracy for the cross section predictions and relevant spectra (e.g. beauty quark p_T and angular distributions). The parton-level events obtained in this way are interfaced to Pythia. From the Pythia/Jetset framework the full fragmentation and decay chains can be applied. All possible branching ratios and decay modes of the heavy quarks are considered

and non-trivial cuts on the final state particles can be implemented, obtaining at the end next-to-leading order cross-section predictions at visible level for heavy-flavour processes.

In contrast to leading-order generators for which parton showers are fundamental to introduce higher order corrections, for the FMNR⊗Pythia interface parton showers are not so relevant because the next-to-leading order calculations already include some of the higher-order contributions. Therefore, parton showers were not implemented. For the FMNR⊗Pythia interface the implementation of hadron-like processes and all branching ratios and decay modes of the heavy quarks was more relevant, opening the possibility to implement sets of complicated cuts at visible level.

The FMNR⊗Pythia interface is thus essential to obtain next-to-leading order predictions for the HERA heavy flavour analyses which use complex cuts on the final state particles. Later, one can also compare with the predictions from the MC@NLO algorithm for HERA which will be available for ep collisions in the near future.

Two examples of the next-to-leading order predictions for HERA data obtained with the new FMNR⊗Pythia interface were presented in this thesis. In the $ep \to b\bar{b}X \to D^*\mu X'$ channel, the measured data at ZEUS exceed the FMNR⊗Pythia NLO prediction, both at visible and quark level, but are compatible within the errors. A comparison to H1 data was also performed. It was found that the H1 and ZEUS visible cross sections are in reasonable agreement. The next-to-leading order prediction is somewhat larger than the one evaluated in [102] due to three facts: the inclusion of the hadron-like photon contribution, the inclusion of secondary-muon branching fractions for D^* and muons from the same b quark (e.g. $B \to D^*D \to D^*\mu X$, which are difficult to handle outside the FMNR⊗Pythia framework), and a detailed simulation of the kinematics of the $b \to B \to D^*$ chain rather than direct collinear fragmentation of b quarks into D^* mesons. This is an example for the importance of a detailed treatment of complicated final states, which could not have been achieved otherwise.

The almost constant data to NLO ratio obtained from the cross sections shows that the extrapolation from visible to quark level, or viceversa, is meaningful and reliable. The extrapolation from visible $\to$ parton-level predictions obtained in early times using plain Pythia was the only way to compare the cross sections before the FMNR⊗Pythia interface were available, and it was not clear if this extrapolation was consistent. This question is now positively answered.

For the $ep \to b\bar{b}X \to \mu^+\mu^- X'$ channel the cross section comparisons at visible and b-quark level are consistent, as in the case of the $D^*\mu$ channel. The predictions are lower than the measured cross sections, but compatible within the uncertainties.

Differential cross sections were also evaluated. The shape of the distributions is well reproduced by the NLO predictions, and agree with the LO + PS predictions, but are somewhat lower than the data, in agreement with the observation from the total cross section.

Other potential applications of the FMNR⊗PYTHIA interface to both charm and beauty measurements in ep and γp interactions have been outlined, such as the evaluation of parton to hadron-level corrections for measurements of the charm fragmentation functions at HERA.

In the last part of this thesis work the ^{G}Elec finder is described. This tool was developed for electron identification in beauty quark events, and it is a first step into the development of a general electron reconstruction algorithm for ZEUS. The ^{G}Elec finder was implemented into a C++ object oriented framework to make it compatible with the general muon reconstruction algorithm ^{G}Muon, which is already extensively used in the ZEUS Collaboration. Therefore, a heavy-flavour analysis using ^{G}Elec and ^{G}Muon could tag any combination of semileptonic muons and/or electrons of a dilepton decay channel.

The ^{G}Elec finder uses discriminating variables based on the track and on the energy deposited in the calorimeter by the electron candidate. Among the most important discriminators, an improved dE/dx measurement and a set of variables related to the shape of the calorimeter cluster were used. These discriminators provide a good signal to background separation power. The ^{G}Elec finder was tested in the reconstruction of the invariant mass distributions for the elastic $J/\psi \to e^+e^-$ process on a sample of HERA I data, and Monte Carlo models for $J/\psi \to e^+e^-$ and beauty-quark production. A clear signal is obtained in the reconstruction of the signal for the data sample with almost no combinatorial background. A very good response is also shown for the $J/\psi \to e^+e^-$ Monte Carlo; and for the case of the beauty Monte Carlo to tag $b\bar{b} \to J/\psi \to e^+e^-$ events the output is acceptable, considering that only electron selection cuts and no other kind of cleaning cuts were applied.

A heavy-flavour analysis has been started using the new ^{G}Elec electron finder. This analysis consists in the study of beauty-quark events decaying into a dilepton, namely the $ep \to b\bar{b}X \to e\mu X'$ channel. In this analysis the dilepton mass distributions for the like- and unlike-sign lepton combination are obtained for a HERA I data sample. The proper background estimation using Monte Carlo models and the calculation of the cross sections for the whole HERA data are left for a further stage of the analysis. One additional advantage of the analysis is that, once the cross sections are measured, the comparison to next-to-leading order theoretical predictions will be very straight-forward because the FMNR⊗PYTHIA interface is at hand.

In general, a study of beauty-quark production and its evolution was framed by the analyses discussed in this thesis work, for which the FMNR⊗PYTHIA interface allows direct comparison of the data to next-to-leading order calculations without the need of extrapolations. From the comparisons presented here, it is clear that there is still the trend observed in other channels, namely the theoretical predictions lying below the data. The inclusion of higher order corrections in the theoretical calculations seems to be still not enough to perfectly match the data, although the difference of the NLO predictions with respect to data is reduced in comparison with previous investigations. This could be an indication of the need to improve other aspects of the theoretical predictions e.g. the definition of the renormalisation or factorisation scales, using for example a parametrisation of μ_0 like $\mu_0 = \sqrt{p_T^2 + m_b^2}/2$. Such a scale choice is analogous to the choice $\mu_0 = E_T/2$ used in measurements at other colliders (Tevatron). This topic is under investigation at the moment and some results are expected soon [97]. Another possibility would be the use of a different mass of the beauty quark e.g. the pole mass or a running b mass. Of course, the implementation in the code of newer parton distribution functions would also improve the predictions. With all that the theoretical error may be further reduced obtaining more accurate predictions even if even higher order contributions, like NNLO or FONLL, will not be calculated any more for these processes.

From the experimental side, in order to get a further insight into the understanding of beauty quark related processes, an investigation of a not yet studied decay channel of the heavy quark (the electron + muon channel) was started. The ^{G}Elec finder developed in this work should help to obtain a better discrimination of the events were beauty quarks are present. The almost complete phase space coverage of this analysis will allow an accurate extraction of the total beauty production cross section, and it is expected to provide a reliable description of the p_T^b spectra down to very low values. A further improvement would be to extend the analysis to use the full HERA data sample which is now available. In this way, the experimental uncertainties will be reduced considerably.

The study of beauty quarks events obtained with the ZEUS detector promises more than ever –because the full sample of HERA data is available– very interesting results, which also complement previous measurements. The use of the tools described in this thesis will provide exciting and accurate results for the upcoming heavy flavour analysis.

List of Figures

List of Tables

Appendix A

Technical implementation of REDSTAT

A.1 Where to find the source code

The complete source code for the modified FMNR code as described in this work, including the REDSTAT extension, can currently be found on the DESY zenith cluster in the directory:
/data/zenith221a/nuncio/nlo
or in the web page:
http://www-zeus.desy.de/ ∼ nuncio/ZEUS ONLY/FMNR/.
Please consult the authors before using the code, in order to avoid pitfalls related to the caveats exposed in Section 6.2.

A.2 Procedure

In FMNR the events are prepared in their final form in the routine `outall` (this routine is found in both the point-like and hadronic programs, though in slightly different forms). Once the event is created, the user routine `outfunmy` is called. Therefore, the best place to implement the Reduced Statistics option is in the function `outall` directly after the event is created and directly before `outfunmy` is called, and this is where the call to the subroutine `redstat1` was placed.

The subroutine `redstat1` works in three main steps. The first step is to explicitly calculate the lab frame four vectors of the partons based on the information provided in the common-block variables p_x and p_y in the lab frame, and the rapidity in the center of mass frame. This calculation is adapted from the one that could

already be found in the subroutine `outfunmy`, and is implemented in the subroutine `getppart`.

If the weight of the event is higher than the threshold, then the second step is to compare the current event to the current "reference" event to determine if they are "similar." This is accomplished in the subroutine `compppart`. Two events are said to be similar if the difference between the rapidities, transverse momentums, and ϕ-angles of the corresponding heavy quarks in the two events are less than user-determined cutoff values. These cutoff values can be set in the control cards (see below).

The third step depends on whether or not the two events are found to be similar. If they are similar, then the third step is to add the current event to the running average of events. This running average consists of the current event, the reference event, and all events in between.

In the case that the two events are dissimilar, the third step is to set the reference event so that it now equals the current event, and also to finally send the previous running average to be output in `outfunmy`. This second part consists of setting the common-block variables to appropriate values, and setting a flag so that when execution returns to `outfun` it is known that `outfunmy` should be called. The common-block variables that need to be calculated are those that were originally supplied: p_x, p_y, and the rapidity in the center of mass frame. The values p_x, p_y are already available, however the rapidity in the center of the rest frame must be calculated. To do this, the calculation used in `getppart` was simply "reversed."

For events with weight smaller than the threshold, the second part is a random decision made in order to keep or discard the event with a probability proportional to its weight. If the event is kept, then the new weight assigned to it equals the threshold, and the event is sent to the output.

The parameters to activate REDSTAT in the control cards are:

```
**** Reduced Statistics Options
redstat  1       0/1 reduced statistics option off/on
angvar   0.45    maximum difference in angle phi between b-quarks
ptvar    1.5     maximum difference in p_t
rapvar   0.38    maximum difference in rapidity
wwwth    -5.0    weight threshold
pythia   0       Output File for the interface to PYTHIA:
                     0 for NO output file
                     1 for the first 15 events
                     2 for ALL events (Warning very big file!)
```

The last parameter `pythia` is not implemented directly in the REDSTAT subroutines. This has to be implemented in the user `analysis_my.fpp` file, where the produced events after the REDSTAT procedure are finally used. This parameter when different from 0, produces two lists of parton level events (one for the point-like processes and one for the hadronic ones). The lists contain the number of the event, the number of final state particles (at parton level it means 2 for quark-antiquark or 3 for the pair + light quark/gluon), the kind of particle (quark, antiquark, gluon), the initial state from where they where produced, the weight of the event and the 4 momentum of the partons, as shown next:

```
Event:      1  Final State Partons: 2  Initial State:pg  Weight:0.10E-04
 Parton: 1  Type: 1  4Momentum:0.00E+00 0.1822E+02 0.4726E+03 0.4730E+03
 Parton: 2  Type: 2  4Momentum:0.00E+00 -.1822E+02 0.6997E+02 0.7246E+02
```

These lists are used in the interface to other packages e.g. PYTHIA as explained in Chapter 6.

Appendix B

Technical implementation of FMNR⊗PYTHIA

B.1 Where to find the source code

The current code version can be found in:

/data/zenith221a/nuncio/nlo   for REDSTAT and

/afs/desy.de/user/g/geiser/public/PYTHIA   for the PYTHIA part.

To avoid potential pitfalls, please contact the authors before using this code or modifying it for other purposes.

B.2 Procedure

The technical implementation of the first part of the interface, the REDSTAT extension to FMNR , is discussed in Appendix A. So far the second part of the interface is implemented in standalone mode of the PYTHIA 6.2 program. In the initialisation part of the PYTHIA main program

- one of the FMNR⊗PYTHIA output ASCII files described in the Appendix A is opened as input file,

- the kinematics of ep interactions and the chosen PYTHIA options are set:

    – PTMIN = 0, no pt cut;

    – MSTP(61) = 0, MSTP(71) = 0, parton showering off;

    – MSTJ(1) = 1 (string) or 2 (independent) fragmentation (varied for systematics);

    – MSTJ(11) = 3, Peterson parametrisation;

    – PARJ(54) = -0.035, epsilon for charm (varied for systematics);

    – PARJ(55) = -0.0035, epsilon for beauty (varied for systematics);

    – PARJ(21) = 0 (no initial k_T) or default (with initial k_T);

- cut values for specific physics channels are set,

- histograms for these physics channels are booked,

- PYTHIA is initialised (default PYINIT with 'USER' option). This calls the "Les Houches" user interface routine UPINIT.

- in UPINIT, the user processes corresponding to the FMNR processes to be read in are initialised.

Then the event loop starts with:

- a call to the default PYEVNT routine, which in turn calls the "Les Houches" user interface routine UPEVNT;

- UPEVNT then reads one event from the input ascii file and fills it into the "Les Houches" interface variables to be used as input by PYTHIA. At this stage, a "reasonable" (i.e. physically possible) colour flow is assigned to each FMNR parton level process. FMNR does not provide this information, which is needed in the case of string fragmentation. The difference due to different possible colour flow assignments should be included in the systematic error if critical for the application;

- apply cuts and fill histograms.

Finally, the histograms are written to an output file. To convert them to cross sections, the so-called EPA flux factor has to be applied correctly for each sample. This is to be included as an automatic rescaling factor into the ASCII file in a later version of the code.

Appendix C

Technical implementation of ^{G}Elec

C.1 Where to find the source code

Currently the code is implemented in a private version of a working frame, named GUTCODE, which was developed and is extensively used by several members of the ZEUS heavy flavour group.

This code can be found in afs under: nuncio/zeus/libraries/GutLib
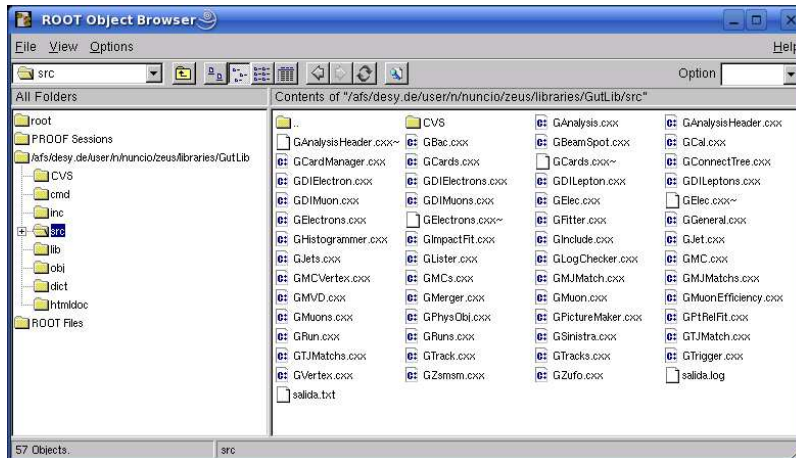
Figure C.1: Working framework GUTCODE where the ^{G}Elec finder is implemented.

C.2 Procedure

The GutLib directory contains the standard structure of an object oriented project as shown in the Figure C.1.

The source code and include files are stored in the corresponding directories, as shown in th example above for the src directory. The new files which are not in the standard CVS group version of the GUTCODE are:GElec.cxx, GElectrons.cxx, GDIElectron.cxx, GDIElectrons.cxx, GDILepton.cxx, GDILeptons.cxx, and their corresponding include files. Nevertheless, most of the other files were also modified to implement the ^{G}Elec into the GUTCODE framework.

References

[1] *HERA – A Proposal for a Large Electron Proton Colliding Beam Facility at DESY*. DESY Report HERA 81-10, Hamburg, Germany (1981).

[2] Yao, W. -M. et. al., J. Phys. **G33**, 1 (2006).

[3] Sokolov, A. A. and Ternov, I. M., Sov. Phys. Dokl. **8**, 1203 (1964).

[4] M. Seidel, *The Upgraded Interaction Regions of HERA*, Technical Report DESY-HERA-00-01, DESY, 2000.

[5] U. Schneekloth (ed.), Preprint HERA-98-05, DESY, 1998, available on `http://www.desy.de/~ahluwali/HERA-98-05/`.

[6] H1 Coll., I. Abt et al., Report DESY-93-103, DESY, 1993.

[7] ZEUS Coll., U. Holm (ed.), *The ZEUS Detector*. Status Report (unpublished), DESY (1993), available on `http://www-zeus.desy.de/bluebook/bluebook.html`.

[8] N. Harnew et al., Nucl. Inst. Meth. **A 279**, 290 (1989);
B. Foster et al., Nucl. Phys. Proc. Suppl. **B 32**, 181 (1993);
B. Foster et al., Nucl. Inst. Meth. **A 338**, 254 (1994).

[9] R. Hall-Wilton et al., *The CTD Tracking Resolution* (unpublished). ZEUS-99-024, internal ZEUS-note, 1999.

[10] Bartsch, D., *Energy-loss measurement with the ZEUS central tracking detector*. Ph.D. Thesis, University of Bonn, 2007. BONN-IR-2007-05.

[11] M. Derrick et al., Nucl. Inst. Meth. **A 309**, 77 (1991);
A. Andresen et al., Nucl. Inst. Meth. **A 309**, 101 (1991);
A. Caldwell et al., Nucl. Inst. Meth. **A 321**, 356 (1992);
A. Bernstein et al., Nucl. Inst. Meth. **A 336**, 23 (1993).

[12] Maddox, E., *Study of heavy quark production at HERA using the ZEUS microvertex detector*. Ph.D. Thesis, Amsterdam University, 2004.

[13] G. Abbiendi et al., Nucl. Inst. Meth. **A 333**, 342 (1993).

[14] H. Abramowicz et al., Nucl. Inst. Meth. **A 313**, 126 (1992).

[15] J. Andruszków et al., Acta Phys. Pol. **B 32**, 2025 (2001).

[16] H. Bethe and W. Heitler, Proc. Roy. Soc. Lond. **A 146**, 83 (1934).

[17] W. H. Smith, K. Tokushuku and L. W. Wiggers, *Proc. Computing in High-Energy Physics (CHEP), Annecy, France, Sept. 1992*, C. Verkerk and W. Wojcik (eds.), p. 222. CERN, Geneva, Switzerland (1992). Also in preprint DESY 92-150B.

[18] S.M. Fisher and P. Palazzi, *ADAMO Programmers Manual – Version 3.2*. CERN ECP, available on `http://adamo.web.cern.ch/Adamo/programmers_manual/TOC_of_adamo.html`.

[19] Calorimeter Group, *CAL Online Primer*. Status Report (unpublished), DESY (2004).

[20] A. Caldwell et al., Nucl. Inst. Meth. **A 321**, 356 (1992).

[21] Brun, R. et al., *PAW: Physics Analysis Workstation*. URL: http://wwwasd.web.cern.ch/wwwasd/paw/.

[22] Altarelli, G., *The standard model of particle physics*. (To appear in) Encyclopedia of Mathematical Physics, Elsevier, 2005.

[23] Nuncio Quiroz, A. E., *Conformal Field Theory on the Manifold $R \times S^3$*. Diploma Thesis, University of Hannover, 2002.

[24] R.K. Ellis, W.J. Stirling and B.R. Webber, *QCD and Collider Physics*, Cambridge Monographs on Particle Physics, Nuclear Physics and Cosmology, Vol. 8. Cambridge University Press, 1996.

[25] D. Griffiths, *Introduction to elementary particles*. John Wiley & Sons, Inc., 1987.

[26] R.P. Feynman, Phys. Rev. Lett. **23**, 1415 (1969).

[27] J.D. Bjorken, Phys. Rev. **179**, 1547 (1969).

[28] J.P. Collins, D.E. Soper and G. Sterman, Nucl. Phys. **B 308**, 833 (1988).

[29] G. Altarelli and G. Parisi, Nucl. Phys. **B 126**, 298 (1977).

[30] Ya.Ya. Balitskiĭ and L.N. Lipatov, Sov. J. Nucl. Phys. **28**, 822 (1978).

[31] V.S. Fadin, E.A. Kuraev and L.N. Lipatov, Phys. Lett. **B 60**, 50 (1975).

[32] E.A. Kuraev, L.N. Lipatov and V.S. Fadin, Sov. Phys. JETP **45**, 199 (1977).

[33] M. Ciafaloni, Nucl. Phys. **B 296**, 49 (1988).

[34] S. Catani, F. Fiorani and G. Marchesini, Phys. Lett. **B 234**, 339 (1990).

[35] S. Catani, F. Fiorani and G. Marchesini, Nucl. Phys. **B 336**, 18 (1990).

[36] Frixione, S., Preprint hep-ph/0111368, 2001.

[37] ZEUS Structure Functions and Electroweak Physics working group,
*Combined H1 and
ZEUS Results on NC and CC Cross Sections* (unpublished), 2000, available on
`http://www-zeus.desy.de/physics/sfew/PUBLIC/sfew_results/preliminary
/lp99/nc-cc-h1-zeus/index.html`.

[38] URL: http://cteq.org/.

[39] Nisius, R., Phys. Rept. **332**, 165 (2000).

[40] A.D. Martin, R.G. Roberts and W.J. Stirling, Phys. Rev. **D 50**, 6734 (1994).

[41] H.L. Lai et al., Phys. Rev. **D 55**, 1280 (1997).

[42] E. Laenen et al., Nucl. Phys. **B 392**, 162 (1993).

[43] E. Laenen et al., Nucl. Phys. **B 392**, 229 (1993).

[44] J. Smith and W.L. van Neerven, Nucl. Phys. **B 374**, 36 (1992).

[45] Olness, F. I. and Tung, W., Nucl. Phys. **B308**, 813 (1988).

[46] Aivazis, M. A. G. and Collins, John C. and Olness, Fredrick I. and Tung,
Wu-Ki, Phys. Rev. **D50**, 3102 (1994).

[47] Aivazis, M. A. G. and Olness, F. I. and Tung, W., Phys. Rev.
D50, 3085 (1994).

[48] Cacciari, M. and Greco, M. and Nason, P., JHEP **05**, 007 (1998).

[49] Cacciari, M. and Frixione, S. and Nason, P., JHEP **03**, 006 (2001).

[50] Buza, M. and Matiounine, Y. and Smith, J. and van Neerven, W. L., Phys.
Lett. **B411**, 211 (1997).

[51] Chuvakin, A. and Smith, J. and van Neerven, W. L., Phys. Rev.
D62, 036004 (2000).

[52] Bloch, I., *Measurement of beauty production from dimuon events at HERA /
ZEUS*. Ph.D. Thesis, University of Hamburg, 2005.
DESY-THESIS-2005-034.

[53] Andersson, B., *The Lund string model*. In Durham 1984, Proceedings,
Antiproton 1984, 447-462.

[54] Khoze, V. A. and Azimov, Y. I. and Frankfurt, L. L., *On the Three
Component Picture of e+ e- → Hadrons*. Mini-rapporteur talk given at 18th
Int. Conf. on High Energy Physics, Tbilisi, USSR, Jul 15-21, 1976.

[55] C. Peterson et al., Phys. Rev. **D 27**, 105 (1983).

[56] Kartvelishvili, V. G. and Likhoded, A. K. and Petrov, V. A., Phys. Lett.
B78, 615 (1978).

[57] Jadach, S., Preprint hep-th/9906207, DESY, Theory group, 1999.

[58] T. Sjöstrand et al., Comp. Phys. Comm. **135**, 238 (2001).

[59] H. Jung, Comp. Phys. Comm. **86**, 147 (1995).

[60] G. Ingelman, J. Rathsman and G.A. Schuler, Comp. Phys. Comm.
101, 135 (1997).

[61] G. Corcella et al., JHEP **01**, 010 (2001).

[62] M. Bengtsson, G. Ingelman and T. Sjöstrand, *Proc. HERA Workshop*,
R.D. Peccei (ed.), Vol. 1, pp. 149–165. DESY, Hamburg, Germany (1987).

[63] T. Sjöstrand, Comp. Phys. Comm. **82**, 74 (1994).

[64] *Geant v3.13 modules* GMOLI.FPP & GMOLS.FPP. In GEANT –
Detector Description and Simulation, CERN Program Library Long Writeup
W5013, available on
`http://wwwasdoc.web.cern.ch/wwwasdoc/geant_html3/node247.html`.

[65] Frixione, S. and Mangano, M. and Nason, P.and Ridolfi, G., Nucl. Phys.
B412, 225 (1994).

[66] Frixione, S. and Mangano, M. and Nason, P.and Ridolfi, G., Phys. Lett.
B348, 633 (1995).

[67] Frixione, S. and Mangano, M. and Nason, P.and Ridolfi, G., Nucl. Phys.
B454, 3 (1995).

[68] Harris, B. W. and Smith, J., Nucl. Phys. **B452**, 109 (1995).

[69] Harris, B. W. and Smith, J., Phys. Lett. **B353**, 535 (1995).

[70] Harris, B. W. and Smith, J., Phys. Rev. **D57**, 2806 (1998).

[71] Frixione, S. and Webber, B., JHEP **06**, 029 (2002).

[72] Frixione, S. and Nason, P. and Webber, B., JHEP **08**, 007 (2003).

[73] Kahle, B., *Measurement of beauty production in deep inelastic scattering at HERA II.* Ph.D. Thesis, University of Hamburg, 2006. DESY-THESIS-2006-011.

[74] Aktas, A. et. al., *Measurement of F2cc and F2bb using the H1 vertex detector at HERA*, 2007.

[75] Augustin, J. E. et. al., Phys. Rev. Lett. **33**, 1406 (1974).

[76] Aubert, J. J. et. al., Phys. Rev. Lett. **33**, 1404 (1974).

[77] Aid, S., et. al., Nucl. Phys. **B472**, 32 (1996).

[78] Derrick, M. et. al., Phys. Lett. **B349**, 225 (1995).

[79] Meyer, A., *Heavy quark production at HERA.* Habilitationsschrift, Hamburg University, 2005.

[80] Aktas, A. et. al., Eur. Phys. J. **C50**, 251 (2007).

[81] Chekanov, S. et. al., *Measurement of the D+ lifetime with the ZEUS Micro-vertex detector at HERA II*, 2006.

[82] Aktas, A. et. al., Eur. Phys. J. **C38**, 447 (2005).

[83] Chekanov, S. et. al., *Measurement of D mesons production in deep inelastic scattering at HERA*, 2007.

[84] Chekanov, S. et. al., Phys. Lett. **B649**, 111 (2007).

[85] Herb, S. W. et. al., Phys. Rev. Lett. **39**, 252 (1977).

[86] Geiser A., Published in *Munich 2007, Deep-inelastic scattering **2**, 883 (2007).

[87] Abbott, B. et. al., Phys. Lett. **B487**, 264 (2000).

[88] Acosta, D. et. al., Phys. Rev. **D71**, 032001 (2005).

[89] Goettlich, M., *Study of charm and beauty production at HERA / H1 using dilepton events.* Ph.D. Thesis, University of Hamburg, 2007. DESY-THESIS-2007-012.

[90] Chekanov, S. et. al., *Measurement of beauty production from dimuon events at HERA.* Submitted to the XXXIII International conference on High Energy Physics, 2006.

[91] Chekanov, S. et. al., Eur. Phys. J. **C50**, 299 (2007).

[92] Aktas, A. et. al., Phys. Lett. **B621**, 56 (2005).

[93] Mangano, M. and Nason, P. and Ridolfi, G., Nucl. Phys. **B373**, 295 (1992).

[94] H. Jung, T. Todt, private communication.

[95] Gladkov, D., *Charm quark pair correlations with D* - muon tag at HERA.* Ph.D. Thesis, University of Hamburg, 2007. DESY-THESIS-2005-034.

[96] Geiser, A. and Nuncio Quiroz, A. E., *The FMNRxPYTHIA interface for Heavy Quark production at HERA*, 2007.

[97] Chekanov, S. et. al., *Measurement of beauty production from dimuon events at HERA*, 2008.

[98] A. Longhin, *Measurement of Beauty Production at HERA with a D∗+μ Tag.* Ph.D. Thesis, Universita di Padova, Padova, Italy, Report DESY-THESIS-2004-050, 2003.

[99] C.F. von Weizsäcker, Z. Phys. **88**, 612 (1934).

[100] E.J. Williams, Phys. Rev. **45**, 729 (1934).

[101] S. Frixione et al., Phys. Lett. **B 319**, 339 (1993).

[102] H1 Coll., A. Aktas et al., Phys. Lett. **B 621**, 56 (2005).

[103] Padhi, S., *Charm jets in photoproduction at HERA.* Ph.D. Thesis, McGill University, 2004. DESY-THESIS-2004-012.

[104] Aktas, A. et. al., Phys. Lett. **B583**, 28 (2004).

[105] Adloff, C. et. al., Phys. Lett. **B467**, 156 (1999).

[106] Aktas, A. et. al., Eur. Phys. J. **C41**, 453 (2005).

[107] Aktas, A. et. al., Eur. Phys. J. **C40**, 349 (2005).

[108] Aktas, A. et. al., Eur. Phys. J. **C47**, 597 (2006).

[109] Breitweg, J. et. al., Eur. Phys. J. **C18**, 625 (2001).

[110] Chekanov, S. et. al., Phys. Rev. **D70**, 012008 (2004).

[111] Chekanov, S. et. al., Phys. Lett. **B599**, 173 (2004).

[112] Gutsche, O., *Measurement of beauty quark cross sections in photoproduction with the ZEUS experiment at the electron proton collider HERA.* Ph.D. Thesis, University of Hamburg, 2005. DESY-THESIS-2005-010.

[113] G.F. Hartner, *VCTRAK Briefing: Program and Math* (unpublished). ZEUS-98-058, internal ZEUS Note, 1998.

[114] Mankel, Rainer, Rept. Prog. Phys. **67**, 553 (2004).

[115] J. Repond, *Jet Energy Corrections* (unpublished). ZEUS-96-133, internal ZEUS Note, 1996.

[116] G.M. Briskin, *Diffractive Dissociation in ep Deep Inelastic Scattering.* Ph.D. Thesis, Tel Aviv University, Report DESY-THESIS 1998-036, 1998.

[117] N. Tuning, *ZUFOs: Hadronic Final State Reconstruction with Calorimeter, Tracking and Backsplash Correction* (unpublished). ZEUS-01-021, internal ZEUS Note, 2001.

[118] S.Catani et al., Nucl. Phys. **B 406**, 187 (1993).

[119] Corradi, M. and Turcato, M., *Beauty production in dijet events*, 2004.

[120] Geiser, A., *GMUON - a general ZEUS muon finder.* ZEUS-Note 06-016.

[121] L. Bellagamba, *MVMATCH: A package to Match FMUON Tracks with Central Detectors* (unpublished). ZEUS-96-051, internal ZEUS Note, 1996.

[122] V.A. Kuzmin, Nucl. Inst. Meth. **A 453**, 336 (2000).

[123] G. Abbiendi et al., *Observation of $J/psi \to \mu^+\mu^-$ in the first $274\,nb^{-1}$ of 1993 Run* (unpublished). ZEUS-93-120, internal ZEUS Note, 1993.

[124] G. Abbiendi, *Global Tracking of Muons in the Barrel and Rear Region* (unpublished). ZEUS-99-063, internal ZEUS Note, 1999.

[125] V. Innocente, M. Maire and E. Nagy, *MC91: Workshop on Detector and Event Simulation in High Energy physics*, K. Bos and B. van Eijk (eds.), pp. 58–78. Amsterdam, NIKHEF (1991).

[126] M. Corradi, *MPMATCH2 Web Page*, available on `http://www-zeus.desy.de/~corradi/ZEUS_ONLY/mpmatch/mpmatch2.html`.

[127] R. Sinkus and T. Voss, Nucl. Inst. Meth. **A 391**, 360 (1997).

[128] Kappes, A., *Measurement of $e^-p \to e^-X$ Differential Cross Sections at High Q^2 and of the structure Function xF_3 with ZEUS at HERA.* Ph.D. Thesis, University of Bonn, 2001. BONN-IR-2001-16.

[129] Bartsch, D.; (Private communication).

Gracias

I want to express my gratitude to all the people that in one way or another influenced my life such that I could accomplish this thesis.

I would like to start with my supervisors. Robert Klanner who warmly took me into his group since those early times when I arrived to DESY as a summer student, his trust in me opened the possibility to start this doctoral work and his support contributed to its finishing. I am especially grateful to Achim Geiser who with his extreme motivation, inspiration, knowledge and scientific curiosity was for me the best guidance and which whom I enjoyed to work with in all this years. I hope we can continue –even remotely– working together.

I am also grateful to Wolfram Zeuner, Elisabetta Gallo and Tobias Haas for their care, support and many wise and helpful advises.

I also got a big support in all senses from the students of my working group, the "beauty team": Oliver Gutsche, Ingo Bloch, Benjamin Kahle, Ursula Samson. I am very grateful for all the time we expended together either with the code, at lunch or during coffee breaks.

The heavy flavour group was also there. Special thanks go to Massimo Corradi and Monica Turcato for their advises and fruitful discussions on the topics of this thesis. I am very grateful to Andrea Longuin and Ingo Bloch for allowed me to get a deeper insight into their measurements and use them in this work.

The technical task working for the calorimeter was one of the most nicer times of the Ph.D. studies. I want to thank Alessandro Polini who was always open to any detector or software question and knew the answer of all of them. Isabell Melzer-Pellmann and Detlef Bartsch from whom I learned a lot about the detector and who were always there to support me. Mauricio Barbi, Roberval Walsh, Wladimir Hain, Bill Schmidke, Cathy Farrow, Amita Raval was a pleasure to work with you.

Huge thanks also to my collegues or fellow students, all dear friends I found at DESY (almost in order of appearance): Oliver Gutsche, Ingo Bloch, Benjamin Kahle, Harald Labes, Sonja Hillert, Alessandro Polini, Isabell Melzer-Pellmann, Philipp Roloff, Damir Lelas, Nicola Coppola, Monica Turcato, Alessandro Montanari, Marta Ruspa, Silvia Miglioranzi, Amita Raval, Heuijin Lim, Julia Grebenyuk, Ana Yaguez Molina, Monica Vazquez, Dorian Kcira, Raquel Santamarta Martinez, Chi-Nhan Nguyen, Aziz Dossanov, Igor Rubinsky, Dmitri Gladkov, Mara Soares, Robert Ciesielski, Tatsiana Klimkovich, Karel Cerny, Daniel Perez Astudillo, Andrea Vargas Treviño, Ricardo Lopez Fernandez, Ursula Samson, Verena Schoenberg, Markus Jungs, Oliver Kind, Roger Renner. Special thanks to Detlef Bartsch from whom I have learned a lot about physics, about cooking and about the life in Germany. Your friendship is invaluable and makes me feel not so far away from home.

I thank Stefano Frixione for the advise on the FMNR program and his suggestions to the FMNR⊗Pythia interface.

My deeper gratitude goes to Prof. Ian Brock who gave me the chance to join his group at the Bonn University.

I also had a life outside DESY, and I thank Laura Carro and all the members of the dance group ATL (from the nahuatl: *Water*) for their friendship and for sharing with me the passion for the Mexican folkloric dance. También para Harald Ihmig, Leticia Cruz, Maria Teresa Gonzalez Osorio y tod@s l@s demas integrantes del grupo INIMEX Hamburg, gracias, ¡La lucha sigue!.

Este trabajo no hubiera sido posible sin el gran apoyo de mi familia. Mis padres Elpidio y Esther, y mis hermanas Karina y Jessica, y tod@s l@s demas de nuestra gran familia. Quiero agradecer especialmente a mis tias Rita, Elena y Rosa que vinieron a cuidarnos y nos trajeron mucha alegria. Mi "mostro" querido gracias por acompañarme todos estos años, por tu apoyo y tu paciencia en los momentos más duros del trabajo. Tu amor me alijeró el camino hasta estas últimas lineas.

Finally, I claim that during my doctoral studies I have discovered two multidimensional, supersymmetric, high energetic, real partners of beauty ...

I named them *Sophie* and *Karel*.